Analysis of Quasi-Optical Components for Far-Infrared Astronomy

Presented by
Paul Kelly, B.Sc.

A thesis submitted for Degree of
Master of Science

Department of Experimental Physics
NUI Maynooth
Co. Kildare
Ireland

May 2014

Head of Department

Professor J. A. Murphy

Research Supervisor

Dr. Créidhe O'Sullivan

Contents

Abstract

This thesis is concerned with the development and analysis of quasi-optical components used in experiments to measure of the CMB in the terahertz and submillimetre wavebands. I have concentrated on corrugated horn structures in the Planck and QUBIC experiments. A precise analysis of the electromagnetic and optical performance of such instruments is required if they are to reach the sensitivity goals required.

The analysis of these components was done through computer simulations and experimentation. There were a number of techniques used to model the horns. These techniques were implemented in NUI Maynooth's in-house simulation code 'Scatter' and a commercial software package known as CST. They were used to predict the beam pattern of corrugated horns including the effects of likely manufacturing errors. NUI Maynooth's Vector Network Analyser was used to confirm the results obtained by the simulations.

The results in this thesis show that variations in corrugated horn made with the efectroforming technique could result in significant degraded performance but that small gaps between the metal sheets in platelet arrays are acceptable.

Acknowledgements

First of all I would like to thank my supervisor Dr. Créidhe O'Sullivan for her advice and commitment throughout this masters project, for always being helpful and patient, and for providing me with the opportunity to perform this research. I would also like to thank Prof. Anthony Murphy for use of the department's facilities.

I am grateful for the assistance given by the technical staff, John Kelly for all computer related problems, David Watson for his hard work on the horn attachments and Ian McAuley for fixing the many things I broke over the two years. Many thanks go to Mr. Derek Gleeson and Mr. Pat Seery who were always there to help me with any problems I had. A special thanks to Gráinne Roche for all her help over the past two years and for the chocolate bunnies at Easter.

I want to thank my office mates Colm Bracken, Robert Dixon and Niamh Tobin for putting up with me over the years. I must also thank my fellow postgraduates that have helped me in over the past two years, their company made my time here entertaining.

I would also like to thank my family, my parents Úna and Brendan, my brothers Mark and David, and my sister Susan for their support over the years.

Chapter 1 Introduction

1.1 Introduction to Terahertz / Submillimetre Astronomy

The main purpose of this research is the analysis of quasi-optical systems for applications in the terahertz and submillimetre wavebands. The focus of much of my work has been on astronomical instrumentation in particular.

Optical astronomy has explored many of the important aspects of the physics of the Universe. However, from the plot of the electromagnetic (EM) spectrum shown in Figure 1.1, it can be seen that the optical region is only a small part of it, extending from $\lambda = 400$ nm to $\lambda = 700$ nm. Therefore much more can be explored with instruments sensitive to the other wavelengths. Since the development of radar technology in WW2 and the discovery of radio emissions from the Milky Way in 1932 by Karl Jansky, a lot more has been discovered about the Universe, for example the existence of radio galaxies, quasars, pulsars and radiation from the beginning of the Universe in the form of cosmic microwave radiation.

Recently other wavebands such as gamma rays, x-rays, ultraviolet, infrared and submillimetre waves have been used to explore the Universe. However, due to the Earth's atmosphere being largely opaque in these wavebands, ground-based instruments cannot be used and this has led to more balloon- and space-born instruments being developed. Some near infrared and submillimetre astronomy is possible from dry high altitude sites.

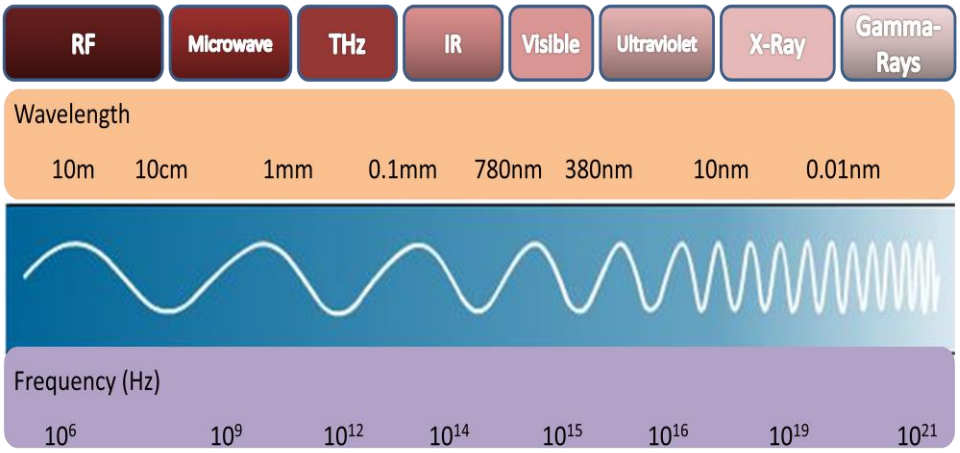

Figure 1.1 The EM spectrum, showing the THz region located between wavelengths of 1mm and 0.1mm.

Terahertz (THz) astronomy generally refers to astronomy in that part of the submillimetre wave region of the electromagnetic spectrum, lying between λ = 100 μm and λ = 1 mm. This region is the last part of the EM spectrum to be exploited and is known as the "THz Gap". The main reason for this is that instruments operating in this waveband are technically challenging to develop. Neither electronic nor optical devices can conveniently be made to work in the THz region. The atmosphere is only partially transparent due to the absorption of water vapour, and therefore the instruments need to be built in high dry areas, like the Mauna Kea site (4200 m) and the ALMA site (5000 m) in Chile. To reduce noise and background radiation loading on the detector, the instruments often need to be cooled to cryogenic temperatures, because the radiation visible at the submillimetre wavelengths originates from extremely cold objects.

The importance of the waveband stems from the fact that approximately 50% of the total luminosity and 98% of the photons emitted since the Big Bang fall into the THz region. The wavelength range from 1mm to 100 μm corresponds to an energy between 0.0012 - 0.012 meV and a blackbody temperature between

14 and 140 K. The THz region is therefore essential for probing the cold Universe.

There is a lot of cold dust and gas in the interstellar medium (ISM) which like many other cold objects emit in the far infrared. Stars and planets are formed in dust clouds where gravity can overcome thermal and magnetic pressures, causing the cloud to collapse. Since dust grains become transparent at submillimetre wavelengths astronomers are able to observe the processes involved in star birth, a process not yet fully understood. Figure 1.2 shows images of the Horsehead Nebula obtained from the Herschel Space Observatory, the dense regions seen at submillimetre wavelengths are believed to be cradles of massive stars. As well as this thermal emission, the THz portion of the EM spectrum is rich in molecular and atomic fine structures lines from species such as CO and OH.

Figure 1.2 The Herschel Space Observatory (left), Horsehead Nebula seen in optical (middle) and in the far-infrared (right) [1] .

Another important branch of THz astronomy is cosmic microwave background astronomy and since this has motivated the need for the quasi-optical components that are the subject of this thesis, this field of study is described in more detail below.

1.2 The Big Bang and the CMB

1.2.1 The Big Bang

The Big Bang theory is a widely accepted theory that is used to describe the early stages and evolution of the Universe. It was first developed by a physics professor and astronomer named Georges Lemaître at the Catholic University of Leuven, Belgium. He pointed out that if the Universe is expanding, there must have been a stage in its past when it was much more dense than it is now. He referred to this as a primeval atom. It was after this hot and dense stage, approximately 14 billion years ago, that a rapid expansion occurred (inflation) after which the rate of expansion slowed. As the universe expanded it cooled down allowing energy to be converted into sub-atomic particles, such as protons, neutrons and electrons. Then after hundreds of thousands of years atoms started to be formed; first hydrogen, then helium and then lithium. Clouds of these elements later coalesced through gravity to form stars and galaxies, the heavier elements were created from within the stars or during supernovae. The Universe continues to expand today (Figure 1.3).

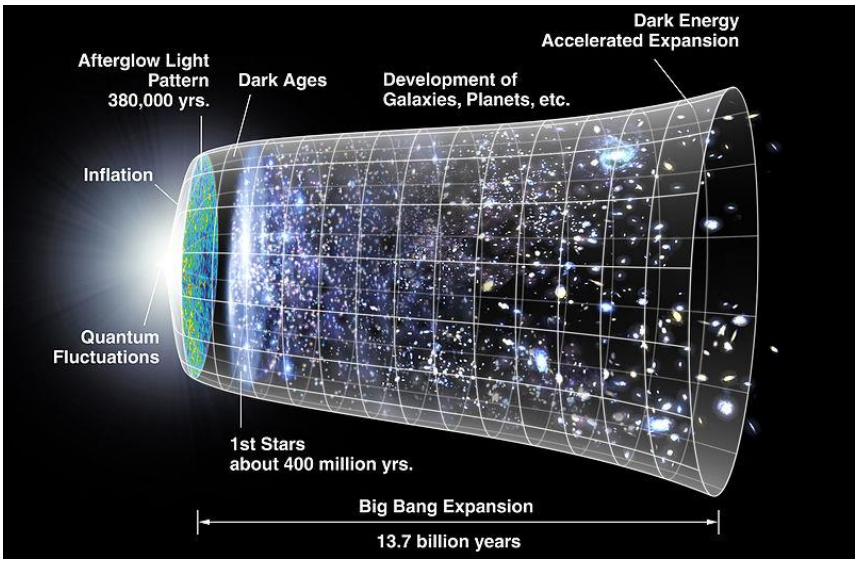

Figure 1.3 This is an artist's concept of the expansion of the Universe [2].

Building on Lemaître's idea that the Universe began in a hot dense state Russian physicist, George Gamow, suggested that when the Universe was 200 seconds old the temperature was greater than 10^9 K. At this temperature nuclear reactions could occur rapidly. In 1948, Ralph Alpher, Hans Bethe and George Gamow showed that these reactions could explain why there is a large abundance of helium within the Universe [3]. Later, both Alpher and Robert Herman postulated that the early Universe was filled with radiation and that this radiation can be detected as a low intensity background in the microwave region in the sky. However, this was more or less forgotten about and it was only in 1960 that his prediction was rediscovered by Robert Dicke and Yakov Zel'dovich.

Within the scientific community at the time there were two theories that were widely supported, the Big Bang and the Steady State theory. However, in 1964 two physicists, Arno Penzias and Robert Wilson, accidentally detected unknown radiation from the sky while using a sensitive radio telescope at the Bell Telephone Laboratories in Holmdel, New Jersey [4]. They found that the intensity of this radiation corresponded to a blackbody at a temperature of approximately 2.7 K. Later at Princeton similar measurements were carried out at different wavelengths that confirmed the presence of this radiation and that it did have a blackbody spectrum. This radiation is now believed to be the remnant radiation that had been proposed by Alpher and Herman called the Cosmic Microwave Background (CMB) radiation. The existence of the CMB converted most of the scientific community to support the Big Bang theory.

1.2.2 The Cosmic Microwave Background

The CMB radiation is believed to have been released approximately 380,000 years after the Big Bang [5]. Before this the Universe was a plasma of

ions and electrons coupled strongly to the photon field (photon-baryon fluid). The large Thompson scattering cross-section of the electrons resulted in a short mean free path for the photons and hence an opaque Universe in thermal equilibrium. The Universe continued to expand, resulting in a decrease in density and temperature. Eventually the Universe cooled enough for the electrons and protons to combine, and form neutral elements such as hydrogen in a process called recombination [6],[7]. The universe then became transparent to the radiation, and with the atoms free from radiation pressure they were able to clump together under gravity to form stars and galaxies, which in turn created heavier elements (Figure 1.4).

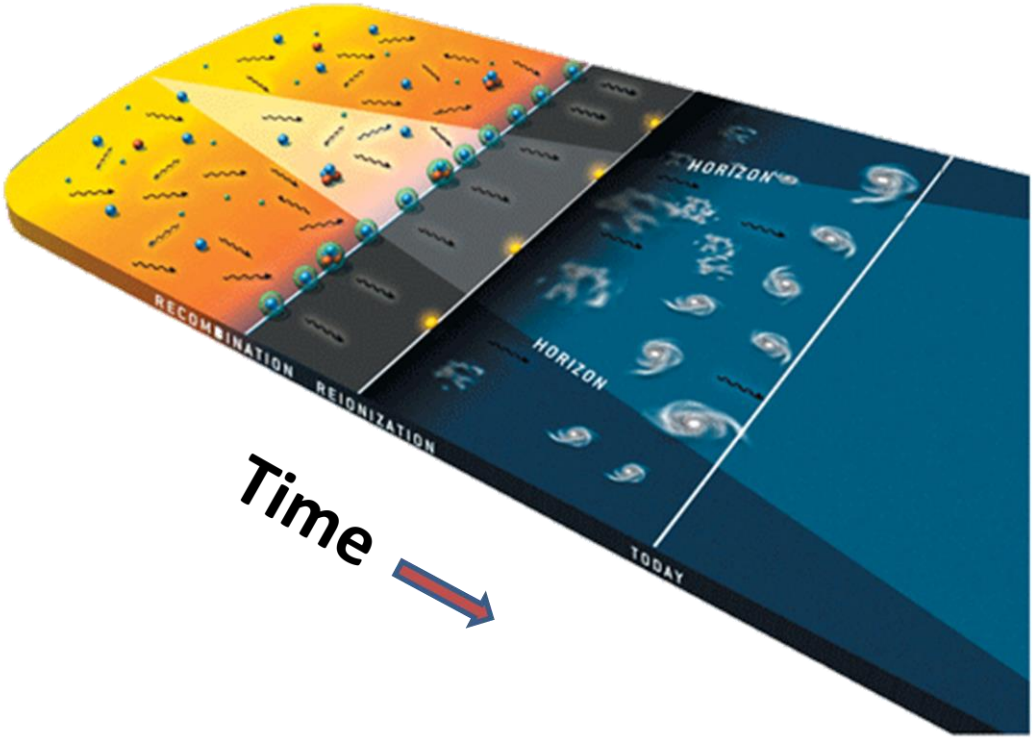

Figure 1.4 The timeline of the Universe, illustrating the radius and particle horizon. [8]

1.2.3 Temperature Anisotropies in the CMB

When Arno Penzias and Robert Wilson discovered the CMB in 1965 they determined that the radiation had a temperature of approximately 2.7 K, and that it

radiated uniformly throughout the sky. Straight away, astronomers and physicists suspected that there should be small temperature fluctuations within the CMB, but it took until 1992 for these fluctuations to measured with the COBE satellite. The average temperature of the CMB radiation was measured by the FIRAS instrument on the COBE satellite and was found to be 2.725 K. In 2001, NASA launched the Wilkinson Microwave Anisotropy Probe (WMAP), which recorded more accurate measurements of the temperature fluctuations. Finally in May 2009, ESA launched PLANCK which has produced the most accurate measurements of the CMB to date (Figure 1.5).

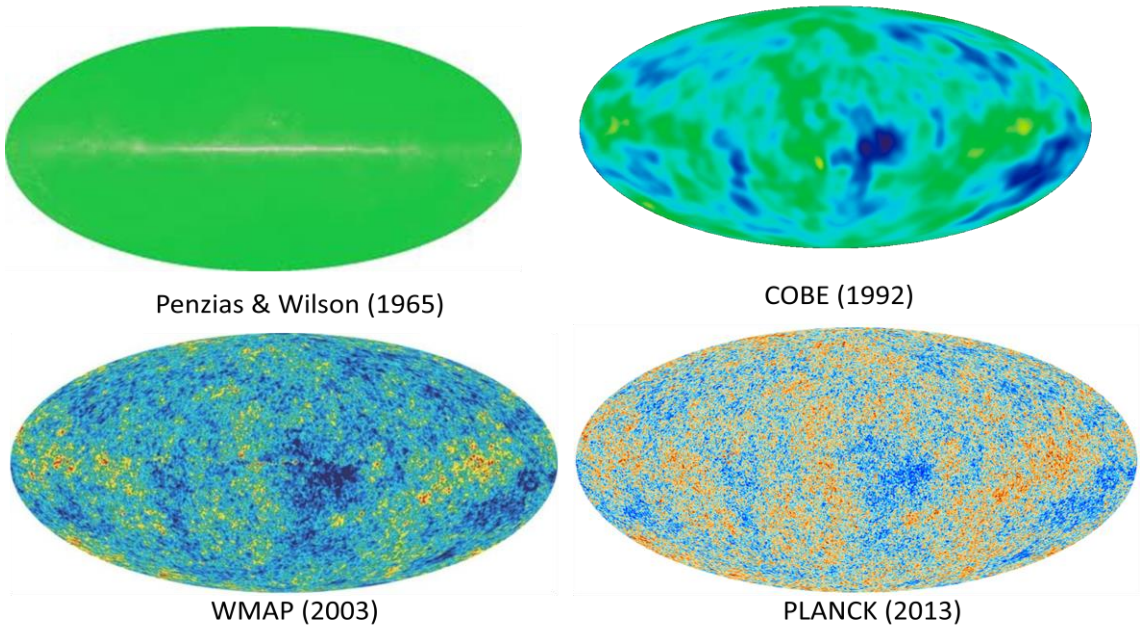

Figure 1.5 The CMB sky map observed by Penzias & Wilson (top left), the COBE satellite (top right), the WMAP satellite (bottom left) and the PLANCK satellite (bottom right) [9].

The features on the map correspond to photon energies at the time of the last scattering of photons by electrons. The areas of highest temperature are red, while the areas of lowest temperature are blue. It is believed that the temperature fluctuations are caused by mass inhomogeneities, throughout the CMB. The cold

spots indicate the more dense regions that are associated with gravitational potential wells cooling photons as they pass through.

Taking an angular power spectrum of the anisotropy of the CMB and comparing it with predictions gives much information about the formation of the Universe and its contents. This angular power spectrum is a plot of how much the temperature varies from one point to another on the sky as a function the multipole moment l (angular frequency l i.e. l=10 corresponds to ten cycles in the fluctuation around the whole sky, while l=100 represents 100 cycles around the sky [10](see Figure 1.6).

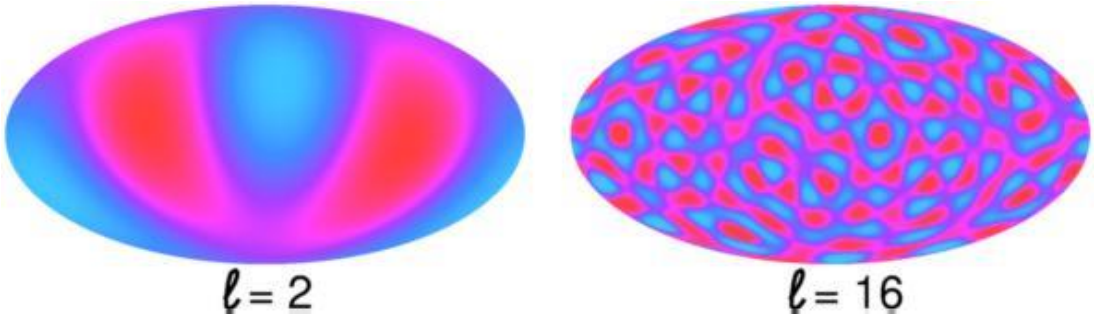

Figure 1.6 The image above shows an all-sky map with only l=2 power on the left, and another map with only l =16 power on the right [10].

Understanding this power spectrum can unlock the values of the key parameters that define current cosmological models. Cosmological models, such as the Big Bang model, arise from the solutions of Einstein's equations of general relativity. The key parameters that describe these solutions include the cosmological constant, Λ, the Hubble constant, H_0, and the density of the Universe, Ω_0. These parameters cannot be derived from theory; it is only from observations, such as examining the anisotropies in the CMB, that we can accurately measure them.

The geometry of the Universe is either open, closed or flat. The parameter Ω_0 dictates which one of these scenarios hold true for our Universe. If Ω_0 is

greater than one, the Universe would be closed, and a value smaller than one would point to an open Universe. Examining the power spectrum (Figure 1.7), the shape, size and position of the peaks in *l*-space probes the horizon size at decoupling which leads to constraints to the parameter Ω_0. It also puts constrains on parameters such as H_0, the fractional density of matter (including baryonic and dark matter Ω_m) and Ω_Λ, the fractional density of dark energy ($\Omega_m + \Omega_\Lambda = \Omega_0$.)

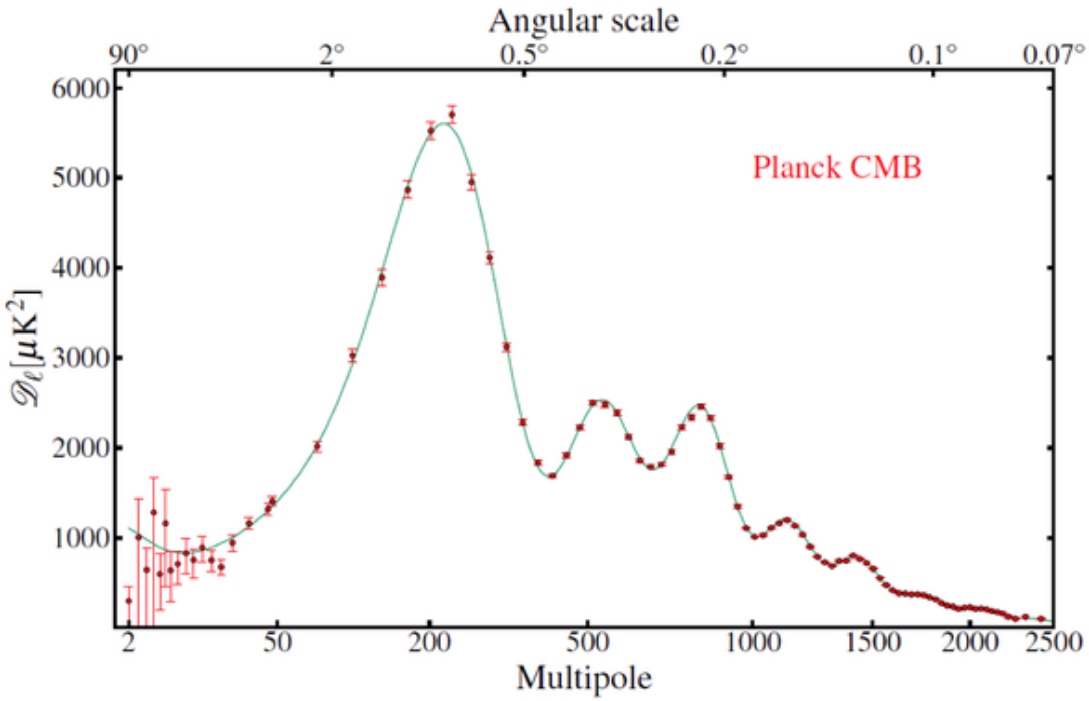

Figure 1.7 The temperature power spectrum measured by PLANCK. The solid line shows the prediction for a 6-parameter ΛCDM model[11].

The data obtained from Plank [11] is perfectly consistent with the ΛCDM model in which a flat Universe that is dominated by a vacuum energy density or cosmological constant which provides 68.3 % of the total density of the Universe. Another 26.8 % of the density is dark matter. Only 4.9 % of the density is ordinary matter consisting of protons and neutrons. This cosmological model, contains dark energy and dark matter contributions.

There can still be degeneracies between some of the cosmological parameters if CMB data alone is used. The polarization properties of the CMB

will break these and place more accurate constraints on the parameters. Polarization studies, in particular, will provide evidence for the theory of Inflation.

1.2.4 CMB Polarization

In 1980 Dr. Alan Guth and Dr. Andrei Linde introduced the world to the theory of Inflation [12]. This theory states that 10^{-38} s after the Big Bang the Universe expanded rapidly. This rapid expansion was so great that it pulled apart pairs of gravitons (theoretical quanta of the gravitational field) that under normal conditions would have annihilated each other. It also stretched the graviton wavelengths from microscopic to macroscopic scales. This in turn would have created gravitational waves. These gravitational waves are moving disruptions of a gravitational field that stretch and compress the space they travel through. These gravitational waves can travel undisturbed through materials that absorb all forms of electromagnetic radiation.

If the theory of Inflation were to be true, these gravitational waves would have echoed through the early Universe (Figure 1.8) and contributed to the temperature fluctuations. These gravitational waves would have stretched and squeezed the primordial plasma which induced motions in the spherical surface that emitted the CMB. This motion would have caused the temperature fluctuations and would have also polarized the CMB.

Figure 1.8 Illustration of the ripples in the CMB temperature caused by gravitational waves [13].

The polarization of the CMB is caused by the scattering of photons off free electrons during decoupling. When an electromagnetic wave is incident on a free electron, the scattered wave is polarized perpendicular to the direction of incidence. If the incident radiation were isotropic or had only a dipole variation, the scattered radiation would have no net polarization (Figure 1.9).

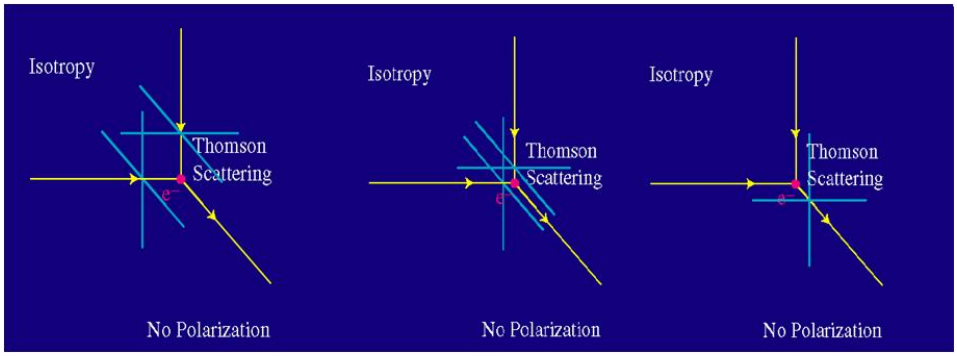

Figure 1.9 The scattering of isotropic radiation resulting in no polarization [14].

If the incident radiation from perpendicular directions (separated by 90°) had different intensities, a net linear polarization would result. Such anisotropy is called "quadrupole" (l=2) because the poles of anisotropy are 90° apart [14] (Figure 1.10).

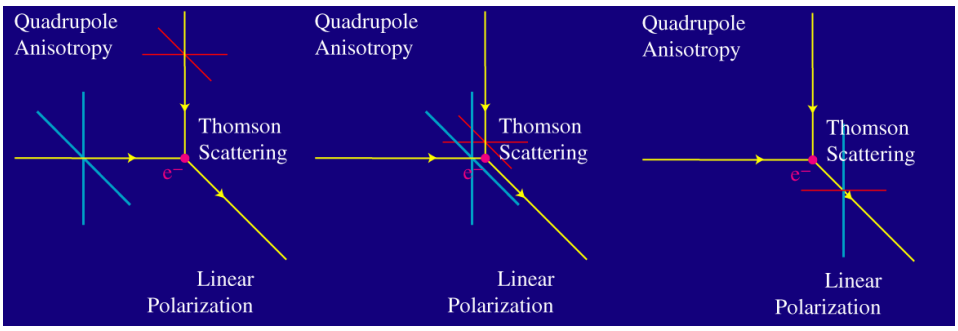

Figure 1.10 The scattering of anisotropic radiation resulting in linear polarization [14].

The quadrupole temperature anisotropy, which is required for the CMB to be polarized, arises from two different disturbances: scalar perturbations, which are due to the motion of matter at the surface of last scattering, and tensor perturbations, which are due to gravity waves.

The polarization can be decomposed into two components: E-modes and B-modes, by analogy with the electric fields (curl-free) and magnetic fields (divergence -free space) of electromagnetism. The curl-free E-modes are caused by both scalar and tensor perturbations. The divergence-free B-modes are caused by tensor perturbations only and so they are often referred to as the "smoking gun of Inflation". E-modes were first detected in 2002 by the ground based telescope DASI (Degree Angular Scale Interferometer) (Figure 1.11). B-modes on the other hand have not yet been detected and are believed to be much fainter than E-modes; to detect them a more sensitive detector is needed. Their detection would prove without a doubt the presences of gravitational waves and show the Inflation theory to be true.

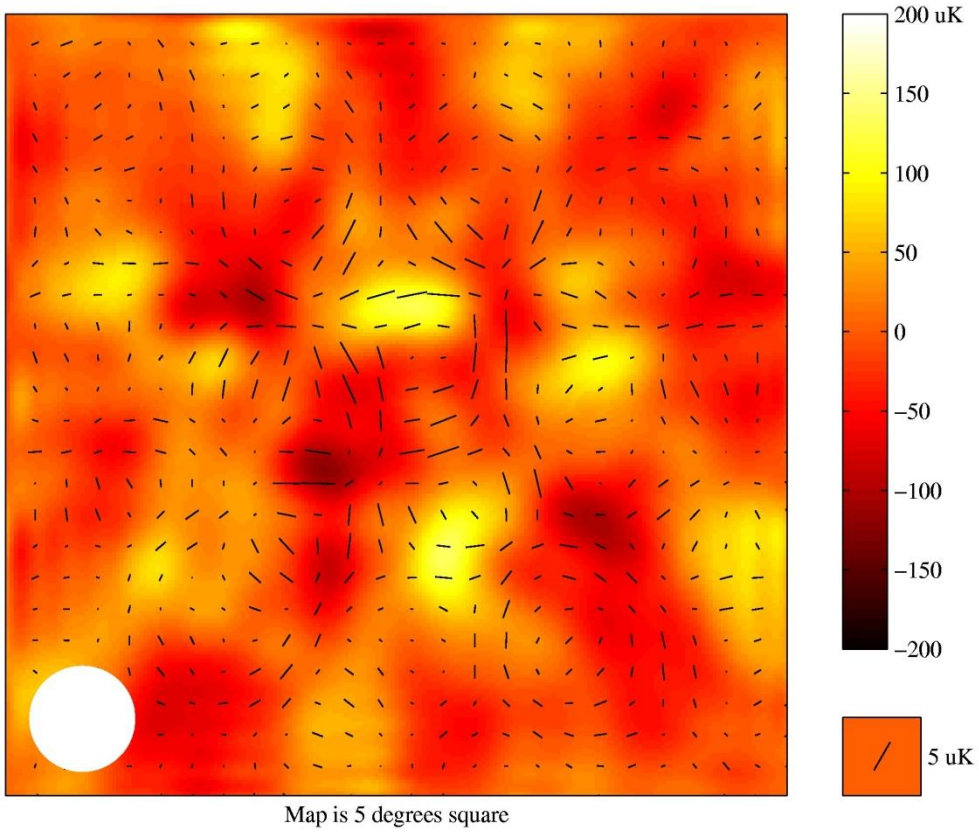

Figure 1.11 An image of the intensity and polarization of the cosmic microwave background radiation. The polarization at each spot in the image is shown by a black line [15].

1.2.5 CMB Instrument Types

In order to minimise or avoid the effects of the atmosphere, especially water vapour, CMB instruments are operated from ground at high altitude dry sites, or are balloon-borne or placed on satellites. These instruments can be imaging or interferometric (particularly good in controling systematic errors) and detectors tend to be bolometers (wide band and very sensitive) or heterodyne (single frequency).

Bolometric Receivers

A bolometer is essentially a resistor that is highly sensitive to change in temperature. They are typically located in a cryostatically cooled chamber in the focus box of a telescope. Its sensitivity to temperature makes it ideal for

measuring the temperature fluctuations in the CMB and the continuum emissions from cool dust clouds in the ISM. The QUBIC experiment discussed later in Chapter 4 will use transition-edge sensors (TESs) as bolometric detectors [16].

TES bolometers are bolometers with a superconducting film biased to operate close to their transition temperature. Along with SQUID readout, amplifiers they become negative feedback thermal detectors, with many favorable operating characteristics. TESs can be made entirely by thin film deposition and optical lithography [17]. They operate at very low power and have a very low noise margin. The TESs for QUBIC are being developed at APC, Paris. A novel feature of QUBIC is that it will do bolometric interferometry in order to take advantage of the control of errors offered by interferometers and the sensitivity of the bolometers. Traditionally heterodyne techniques, discussed next, are used in interferometers.

Heterodyning

Heterodyning is a technique that is commonly used for radio telescopes. This technique mixes the incoming signal coming from the sky with a locally generated, highly stable, reference signal known as a local oscillator (LO). This process generates a difference signal with a lower frequency that is easier to manage and detect. This signal still contains the all the information that was contained in the signal from the sky.

For a sub-millimetre telescope, the mixing between the LO signal and the sky signal can be done by coupling them onto a very small diode located in a wave-guide at the back of a horn antenna. The signal can then be analysed using an acousto-optic spectrometer.

1.2.6 CMB Experiments

In this section I list some of current, past and future CMB experiments. These experiments are either ground based, balloon-borne or space based.

Ground Based

Ground based CMB experiments need to be located in areas of low humidity areas, such as the Mauna Kea Chile or Antarctica.

One example of a ground based CMB experiment, with which NUI Maynooth was involved with, is QUaD. QUaD was a ground based high-resolution instrument located at the south pole and was designed to map the polarization of the CMB. QUaD is an acronym for "QUEST at DASI". QUEST (Q and U Extragalactic Sub-mm Telescope) was the original name attributed to the bolometer detector instrument, while DASI was the interferometer experiment which was the first to measure E-mode polarization. QUaD used the existing DASI mechanical infrastructure, but replaced the DASI interferometer array with bolometric detectors operating at 100 and 150 GHz located in the focal plane of a 2.6 m Cassegrain telescope. It ran between 2005 and 2007. I will describe the QUBIC experiment later in this thesis. Other ground based telescopes are listed below (Table 1.1).

Table 1.1 A list of some of ground based experiments

Name	Date	Detector	Frequency (GHz)
Arcminute Microkelvin Imager (AMI)	2005-	HEMT	12-18
Array for Microwave Background Anisotropy (AMiBA)	2002-	MMIC	86-102

Atacama Cosmology Telescope (ACT)	2007-	Bolometer	145, 225, 265
Atacama Pathfinder Experiment (APEX)	2005-	Bolometer	150, 217
Advanced Cosmic Microwave Explorer (ACME)	1988-1996	HEMT	26-35; 38-45
APACHE	1995-1996	Bolometer	100, 150 , 250
Australia Telescope Compact Array (ATCA)	1991-1997	HEMT	8.7
ACBAR	2001-	Bolometer	150, 219, 274
BICEP	2006-2008	Bolometer	100, 150
CAPMAP	2002-	MMIC/HEMT	40, 90
QUaD	2005-2007	Bolometer	100, 150
QUBIC	Future	Bolometer	97, 150, 230

Balloon-Borne

Airborne or balloon based CMB experiments have the benefit of going above most of Earth's atmosphere which reduces the atmospheric absorption of microwaves to a minimum. This is less costly compared to a satellite probe, the only drawback is that only a small part of the sky can be scanned.

The BOOMERanG experiment (Balloon Observations Of Millimetric Extragalactic Radiation ANd Geophysics) was a telescope designed to measure

the CMB radiation of a part of the sky during three sub-orbital balloon flights. The first flight was a test flight in 1997, which was launched from North America. The balloon was then launched in 1998 and 2003 from McMurdo Station in the Antarctic. It was carried by the Polar vortex winds in a circle around the South Pole, returning after two weeks. The experiment consisted of bolometers and a 1.2m mirror which focused the CMB radiation onto 16 horn-fed bolometers. The data from the 1998 flight to showed that the Universe was close to spatial flatness, with the total density within about 10% of the critical density. The second flight in 2003 made improved measurements of the microwave temperature anisotropies and polarization [18]. Other airborne or balloon based experiments are outline below (Table 1.2).

Table 1.2 A list of some of airborne based experiments

Name	Year	Instruments	Frequency (GHz)
Archeops	1999 -2002	Bolometer	143, 217, 353, 545
Cobra	1982 -1990	Bolometers/ FTS	15-800
MAXIMA	1995	Bolometer	150-420
QMAP	1996	HEMT/SIS	30-140
The E and B Experiment (EBEX)	Future	Bolometer	150-450
SPIDER	Future	Bolometer	90-210

Space Based

Space based experiments are ideal for measuring the CMB, due to the lack of water absorption from Earth's atmosphere. They offer a wide scan area; however, they are very expensive.

An example of a space based experiment is the Cosmic Background Explorer (COBE). It was launched on November 1989 and is a satellite designed to investigate the CMB from an orbit of 900.2 km above the Earth's surface. It is equipped with three instruments; Diffuse Infrared Background Experiment (DIRBE), Far-Infrared Absolute Spectrometer (FIRAS) and Differential Microwave Radiometer (DMR). The DIRBE instrument was a multi-wavelength infrared detector and was used to map dust emission. The FIRAS instrument was used as a spectrophotometer to measure the spectrum of the CMB and the DMR instrument was a microwave instrument that was used to map the temperature anisotropies in the CMB. COBE was the first experiment to produce a complete sky map of the CMB; it finished its measurements in 1993. The most recent CMB experiment was the Planck satellite, which finished its measurements in 2013. This experiment will be discussed in more detail in Chapter 5. Other space based experiments are outline below (Table 1.3).

Table 1.3 A list of some of ground based experiments

Name	Year	Instruments	Frequency (GHz)
RELIKT	1983	Radiometer	37
COBE	1989	Radiometer	31.5-90
WMAP	2001	Radiometer	23-94
Planck	2009	Bolometer	30-857

1.3 Other Terahertz Applications

Advances in THz technology have led to THz radiation being exploited in fields outside of astronomy. The main applications for THz radiation can be divided into two categories: sensing and communication. With advanced technological methods such as Terahertz Time Domain Spectroscopy (TDS) and

Frequency Domain Spectroscopy (FDS), the sensing capabilities for many research fields including biology, pharmacy, medical science, material science, environment monitoring and security have improved. The use of THz also improves technology for information and communication. In areas such as wireless communication, high speed data processing and satellite communication.

THz radiation has biomedical applications because it is non-ionizing and isn't scattered in tissues. Terahertz Pulse imaging or TPI is one of these biomedical applications which uses pulses of electromagnetic radiation in a frequency range of 0.1 to 10 THz [19] and it has been used to image teeth and skin (Figure 1.12). Skin cancer imaging is a popular area of THz medical research due to its location on the surface of the body thus avoiding the difficulty of tissue penetration that rendered imaging on living specimen impossible. A great deal of work has been done on this topic by groups in Leeds, and Teraview in Cambridge [20].

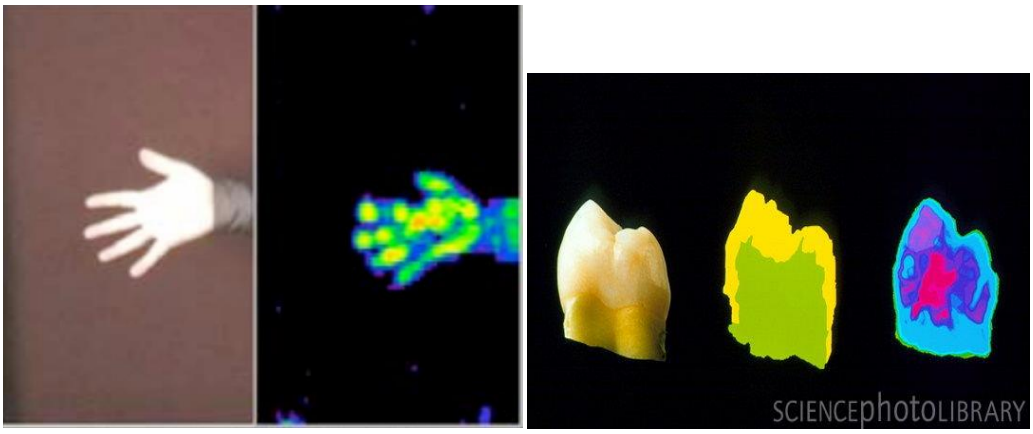

Figure 1.12 Image of a hand and dried tooth in the terahertz region.[21]

Industries use THz radiation to inspect and analyse their products. It can be used to inspect silicon solar cells, nanocomposites, polymer films and dielectric films for example. The most prominent industry for THz technology is the semiconductor industry. It has already been used to examine certain

semiconductor wafer properties such as mobility, conductivity, carrier density and plasma oscillations. THz radiation is used in the identification of explosives and narcotics, using reflective time domain spectroscopy (THz-RTDS)[22]. This is due to the fact that every explosive and narcotic has a distinct signature in the THz range. Waves below 3.0 THz can pass through envelopes so their contents can be identified without the need to open them. THz radiation can be used in the detection of concealed weapons, for example (Figure 1.13) using a stand-off imaging system [23].

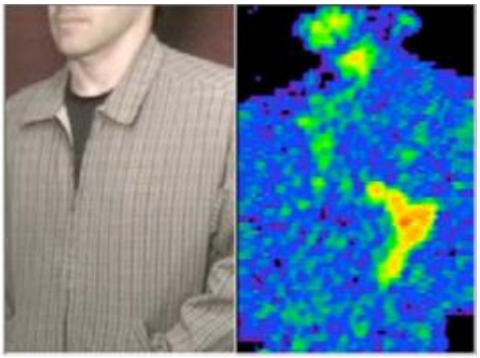

Figure 1.13 Shows a concealed weapon.[23]

Within the information and communication sector, there is also potential for THz applications. Fibre optical communication is growing rapidly with data rates exceeding a terabyte per second, whereas the data rate for wireless communication remains relatively low. The introduction of THz wireless communication would be of great benefit for applications, such as communication in rural areas, communication between buildings during disasters, and high-vision data delivery for entertainment. Communication with THz radiation is secure from eavesdropping, due to the fact that the radiation doesn't propagate far through the atmosphere, and it also has a very high capacity, greater than 10 Gb/s.

1.4 Summary and Thesis Outline

In this chapter, I have discussed the THz region of the EM spectrum, its importance and role in submillimeter astronomy. I have also introduced the theory of the origin of the CMB and the importance of making accurate measurements of the CMB's temperature and polarization fluctuations. I have described some of the instruments used in the measuring of the CMB and I have discussed some of the past experiments. This Thesis is concerned with the design and analysis of CMB astronomical instrumentation at GHz and THz frequencies. A precise analysis of the electromagnetic and optical performance of such instruments is required if they are to reach the sensitivity goals required. I have concentrated on corrugated horn structures in the Planck and QUBIC experiments.

In Chapter 2, I will discuss the optical analytical techniques used throughout this thesis. In Chapter 3, I will describe some of the modifications and improvements made to some of the in-house software used to model horn structures in particular. In Chapter 4, I will introduce the QUBIC experiment and some of the issues that can arise from the use of platelets in the fabrication of corrugated horns. In Chapter 5, I will discuss the Planck satellite and some of the issues that can arise from using electroformed corrugated horns. Finally Chapter 6 will summarise the work done in this project.

Chapter 2

Techniques For Modelling Horn Antennas

2.1 Introduction

This chapter outlines the techniques used in the modelling and analysis of horn antennas. There are two techniques used throughout this thesis: one implemented in commercial simulation software called "CST Studio Suite" [24] and the other in an in-house analytical software program called "Scatter" [25]. This chapter will also outline the properties of waveguides and corrugated horns.

2.2 Waveguides

2.2.1 Solutions to Maxwell's Equations in Waveguides

Waveguides are used to transfer electromagnetic power from one point in space to another. The design of the waveguide depends on the frequency of the radiation detected, the amount of power to be transferred and the amount of transmission losses that can be tolerated.

When dealing with waveguides, we look for the solutions to Maxwell's equations for electromagnetic radiation which is propagating in one direction (usually called the z direction) and is confined within the boundaries of the guiding structure. The following derivations of the electric and magnetic fields are from [26]. The electric and magnetic fields are assumed to have the form:

$$\mathbf{E}(x,y,z,t) = \mathbf{E}(x,y)e^{j\omega t - j\beta z} \quad \textbf{(2.1)}$$

$$\mathbf{H}(x,y,z,t) = \mathbf{H}(x,y)e^{j\omega t - j\beta z} \quad \textbf{(2.2)}$$

where β is the propagating wave number along the direction of the waveguide. The guide wavelength is denoted by $\lambda_g = 2\pi/\beta$. The fields cannot be uniform because they are confined in the transverse directions (the *x*, *y* directions). They can be decomposed into components:

$$\mathbf{E}(x,y) = \hat{\mathbf{x}}E_x(x,y) + \hat{\mathbf{y}}E_y(x,y) + \hat{\mathbf{z}}E_z(x,y) \equiv \mathbf{E}_T(x,y) + \hat{\mathbf{z}}\mathrm{E}_z(x,y) \quad \textbf{(2.3)}$$

with $$\boldsymbol{\nabla} = \hat{\mathbf{x}}\partial_x + \hat{\mathbf{y}}\partial_y + \hat{\mathbf{z}}\partial_z = \nabla_T - j\beta\hat{\mathbf{z}}. \quad \textbf{(2.4)}$$

These fields can be introduced to the source-free Maxwell's equations giving us:

$$\boldsymbol{\nabla} \times \mathbf{E} = -j\omega\mu\mathbf{H} \rightarrow (\boldsymbol{\nabla}_T - j\beta\hat{\mathbf{z}}) \times (\mathbf{E}_T + \hat{\mathbf{z}}E_z) = -j\omega\mu(\mathbf{H}_T + \hat{\mathbf{z}}H_z) \quad \textbf{(2.5)}$$

$$\boldsymbol{\nabla} \times \mathbf{H} = j\omega\varepsilon\mathbf{E} \rightarrow (\boldsymbol{\nabla}_T - j\beta\hat{\mathbf{z}}) \times (\mathbf{H}_T + \hat{\mathbf{z}}H_z) = j\omega\varepsilon(\mathbf{E}_T + \hat{\mathbf{z}}E_z) \quad \textbf{(2.6)}$$

$$\boldsymbol{\nabla} \cdot \mathbf{E} = 0 \rightarrow (\boldsymbol{\nabla}_T - j\beta\hat{\mathbf{z}}) \cdot (\mathbf{E}_T + \hat{\mathbf{z}}E_z) = 0 \quad \textbf{(2.7)}$$

$$\boldsymbol{\nabla} \cdot \mathbf{H} = 0 \rightarrow (\boldsymbol{\nabla}_T - j\beta\hat{\mathbf{z}}) \cdot (\mathbf{H}_T + \hat{\mathbf{z}}H_z) = 0\,. \quad \textbf{(2.8)}$$

where ε is the dielectric constant and μ the relative permeability of the medium. Depending on whether both, one or none of the longitudinal components are equal to zero, we classify the solutions as transverse electric and magnetic (TEM), transverse electric (TE) or transverse magnetic (TM), or hybrid:

$$E_z = 0 \quad , \; H_z = 0 \quad \text{(TEM)}$$

$$E_z = 0 \quad , \; H_z \neq 0 \quad \text{(TE)}$$

$$E_z \neq 0 \quad , \; H_z = 0 \quad \text{(TM)}$$

$$E_z \neq 0 \quad , \; H_z \neq 0. \quad \text{(Hybrid)}$$

In most of the cases at least one of the longitudinal components E_z and H_z are non-zero and we can write transverse field components $\mathbf{E_T}$ and $\mathbf{H_T}$ in terms of

longitudinal components. Equating the transverse and longitudinal components of the first two Maxwell equations gives a linear system with two unknowns $\hat{\mathbf{z}}\times \mathbf{E_T}$ and $\mathbf{H_T}$, that is,

$$\beta\hat{\mathbf{z}} \times \mathbf{E}_T - \omega\mu\mathbf{H}_T = j\hat{\mathbf{z}} \times \nabla_{\mathrm{T}} E_z \qquad \textbf{(2.9)}$$

$$\omega\varepsilon\hat{\mathbf{z}} \times \mathbf{E}_T - \beta\mathbf{H}_T = -j\nabla_T H_z \, . \qquad \textbf{(2.10)}$$

The solution to these equations are

$$\hat{\mathbf{z}} \times \mathbf{E}_T = -\frac{j\beta}{k_c^2}\hat{\mathbf{z}} \times \nabla_T E_z - \frac{j\omega\mu}{k_c^2}\nabla_T H_z \, , \qquad \textbf{(2.11)}$$

$$\mathbf{H}_{\mathrm{T}} = -\frac{j\beta}{k_c^2}\hat{\mathbf{z}} \times \nabla_T E_z - \frac{j\omega\mu}{k_c^2}\nabla_T H_z \, , \qquad \textbf{(2.12)}$$

where k_c is the cutoff wavenumber, ω_c and λ_c are the cutoff frequency and wavelength respectively and are defined by:

$$k_c^2 = \omega^2\varepsilon\mu - \beta^2 = \frac{\omega^2}{c^2} - \beta^2 = k^2 - \beta^2,$$

$$\omega_c = ck_c,$$

$$\lambda_c = \frac{2\pi}{k_c}.$$

At this point we introduce the transverse impedances for TE and TM modes which are defined as:

$$\eta_{TE} = \frac{\omega\mu}{\beta} = \eta\frac{\omega}{\beta \mathrm{c}} \quad , \eta_{TM} = \frac{\beta}{\omega\varepsilon} = \eta\frac{\beta c}{\omega}$$

where the medium impedance is $\eta = \sqrt{\frac{\mu}{\epsilon}}$, so that $\eta/c = \mu$ and $\eta c = 1/\epsilon$. With these definitions we rewrite equations (2.11) and (2.12) as:

$$\hat{\mathbf{z}} \times \mathbf{E}_T = -\frac{j\beta}{k_c^2}(\hat{\mathbf{z}} \times \nabla_T E_z + \eta_{TE}\nabla_T H_z) \qquad \textbf{(2.13)}$$

$$\mathbf{H}_T = -\frac{j\beta}{k_c^2}\left(\frac{1}{\eta_{TM}}\hat{\mathbf{z}} \times \boldsymbol{\nabla}_T E_z + \boldsymbol{\nabla}_T H_z\right). \quad \textbf{(2.14)}$$

Since $\hat{\mathbf{z}} \times (\hat{\mathbf{z}} \times \mathbf{E_T}) = -\mathbf{E_T}$,we solve for $\mathbf{E_T}$ and $\mathbf{H_T}$

$$\mathbf{E_T} = -\frac{j\beta}{k_c^2}\left(\boldsymbol{\nabla_T} E_z - \eta_{TE}\hat{\mathbf{z}} \times \boldsymbol{\nabla}_T H_z\right) \quad \textbf{(2.15)}$$

$$\mathbf{H}_T = -\frac{j\beta}{k_c^2}\left(\boldsymbol{\nabla}_T E_z + \frac{1}{\eta_{TM}}\hat{\mathbf{z}} \times \boldsymbol{\nabla}_T E_z\right). \quad \textbf{(2.16)}$$

Hence Maxwell's equations are written in the following forms:

$$\boldsymbol{\nabla} \times \mathbf{E_T} + j\omega\mu\hat{\mathbf{z}}H_z = \frac{j\omega\mu}{k_c^2}\hat{\mathbf{z}}(\nabla_T^2 H_z + k_c^2 H_z) \quad \textbf{(2.17)}$$

$$\boldsymbol{\nabla} \times \mathbf{H_T} - j\omega\varepsilon\hat{\mathbf{z}}E_z = -\frac{j\omega\epsilon}{k_c^2}\hat{\mathbf{z}}(\nabla_T^2 E_z + k_c^2 E_z) \quad \textbf{(2.18)}$$

$$\boldsymbol{\nabla} \cdot \mathbf{E_T} - j\beta E_z = -\frac{j\beta}{k_c^2}(\nabla_T^2 E_z + k_c^2 E_z) \quad \textbf{(2.19)}$$

$$\boldsymbol{\nabla} \cdot \mathbf{H}_T - j\beta H_z = -\frac{j\beta}{k_c^2}(\nabla_T^2 H_z + k_c^2 H_z) \quad \textbf{(2.20)}$$

where ∇_T^2 is a two dimensional Laplacian operator:

$$\nabla_T^2 = \boldsymbol{\nabla_T} \cdot \boldsymbol{\nabla_T} = \partial_x^2 + \partial_y^2 .$$

The longitudinal fields $E_z(x,y)$, $H_z(x,y)$ must satisfy the two dimensional Helmholtz equations

$$\nabla_T^2 E_z + k_c^2 E_z = 0 \quad \textbf{(2.21)}$$

$$\nabla_T^2 H_z + k_c^2 H_z = 0 \quad \textbf{(2.22)}$$

in order for Maxwell's equations to be satisfied. In the case of rectangular and circular waveguides the wave solutions can be in either Cartesian or cylindrical coordinates [26].

Transverse Electric (TE) Modes

Transverse Electric modes are characterized by the conditions that $H_z \neq 0$ and E_z=0. The equations that describe the transverse components (equations 2.15 and 2.16) and longitudinal components (equations 2.21 and 2.22) become:

$$\nabla_T^2 H_z + k_c^2 H_z = 0 \quad \textbf{(2.23)}$$

$$\mathbf{H_T} = -\frac{j\beta}{k_c^2}\nabla_T H_z \quad \textbf{(2.24)}$$

$$\mathbf{E_T} = \eta_{TE}\mathbf{H_T} \times \hat{\mathbf{z}}\,. \quad \textbf{(2.25)}$$

In cartesian coordinates the equations become:

$$(\partial_x^2 + \partial_y^2)H_z + k_c^2 H_z = 0 \quad \textbf{(2.26)}$$

$$H_x = -\frac{j\beta}{k_c^2}\partial_x H_z \;, \quad H_y = -\frac{j\beta}{k_c^2}\partial_y H_z \quad \textbf{(2.27)}$$

$$E_x = \eta_{TE} H_y \;, E_y = -\eta_{TE} H_x\,. \quad \textbf{(2.28)}$$

In cylindrical coordinates the equations become:

$$\frac{1}{\rho}\frac{\partial}{\partial\rho}\left(\rho\frac{\partial H_z}{\partial\rho}\right) + \frac{1}{\rho^2}\frac{\partial^2 H_z}{\partial\phi^2} + k_c^2 H_z = 0 \quad \textbf{(2.29)}$$

$$H_\rho = -\frac{j\beta}{k_c^2}\left(\frac{\partial H_z}{\partial\rho}\right), H_\phi = -\frac{j\beta}{k_c^2}\frac{1}{\rho}\left(\frac{\partial H_z}{\partial\phi}\right) \quad \textbf{(2.30)}$$

$$E_\rho = \eta_{TE} H_\phi \;, E_\phi = -\eta_{TE} H_\rho. \quad \textbf{(2.31)}$$

Transverse Magnetic (TM) Modes

The transverse magnetic (TM) modes are characterised by the conditions that H_z = 0 and $E_z \neq 0$. With these conditions in mind the equations that describe the transverse and the longitudinal components become:

$$\nabla_T^2 H_z + k_c^2 H_z = 0 \quad \textbf{(2.32)}$$

$$\mathbf{E_T} = -\frac{j\beta}{k_c^2}\nabla_T E_z \quad \textbf{(2.33)}$$

$$\mathbf{H_T} = \frac{1}{\eta_{TM}}\hat{\mathbf{z}} \times \mathbf{E_T}\ . \quad \textbf{(2.34)}$$

The relationship between H_z and E_z is the same as that of uniform plane waves propagating in the z-direction but the wave impedance is replaced by η_{TM}.

In cartesian coordinates the equations become:

$$(\partial_x^2 + \partial_y^2)E_z + k_c^2 E_z = 0 \quad \textbf{(2.35)}$$

$$E_x = -\frac{j\beta}{k_c^2}\partial_x E_z \ , \quad E_y = -\frac{j\beta}{k_c^2}\partial_y E_z \quad \textbf{(2.36)}$$

$$H_x = \eta_{TE} E_y \ , H_y = -\eta_{TE} E_x\ . \quad \textbf{(2.37)}$$

In cylindrical coordinates the equations become:

$$\frac{1}{\rho}\frac{\partial}{\partial\rho}\left(\rho\frac{\partial E_z}{\partial\rho}\right) + \frac{1}{\rho^2}\frac{\partial^2 E_z}{\partial\phi^2} + k_c^2 E_z = 0 \quad \textbf{(2.38)}$$

$$E_\rho = -\frac{j\beta}{k_c^2}\left(\frac{\partial E_z}{\partial\rho}\right), E_\phi = -\frac{j\beta}{k_c^2}\frac{1}{\rho}\left(\frac{\partial E_z}{\partial\phi}\right) \quad \textbf{(2.39)}$$

$$H_\rho = \eta_{TE} E_\phi \ , H_\phi = -\eta_{TE} E_\rho. \quad \textbf{(2.40)}$$

2.2.2 Rectangular Waveguides

Consider a rectangular waveguide with conducting walls, as shown in Figure 2.1, where the lengths *a*, *b* of the inner sides satisfy $b \leq a$.

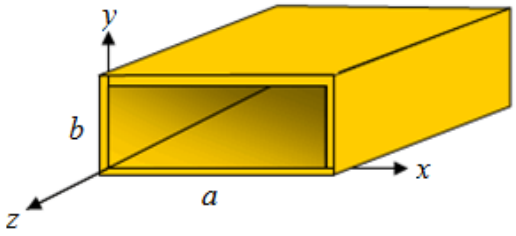

Figure 2.1 Rectangular Waveguide [27]

Rectangular Waveguide TE modes

The expressions for the TE (and TM) modes are derived using cartesian coordinates. We start by looking at the solutions for the Helmholtz equation that are factorable in their *x* and *y* dependence:

$$H_z(x,y) = F(x)G(y). \qquad \textbf{(2.41)}$$

Then equation (2.35) becomes:

$$F''(x)G(y) + F(x)G''(y) + k_c^2 F(x)G(y) = 0 \;\rightarrow\; \frac{F''(x)}{F(x)} + \frac{G''(y)}{G(y)} + k_c^2 = 0. \qquad \textbf{(2.42)}$$

These must be valid for all *x*, *y*, therefore the *F* and *G* terms must be constants, independent of *x* and *y*. Therefore we can write:

$$\frac{F''(x)}{F(x)} = -k_x^2 \text{ and } \frac{G''(y)}{G(y)} = k_y^2,$$

where $k_c^2 = k_x^2 + k_y^2$, $k_x = \frac{m\pi}{a}$ and $k_y = \frac{n\pi}{b}$. The *m* and *n* indices indicate that only discrete solutions for the transverse wavenumber (k_c) are allowed. Physically, this occurs because we've bounded the system in the *x* and *y* directions [28]. The solutions that will satisfy the boundary conditions are $F(x) = \cos k_x x$

and $G(y) = \cos k_y y$ for $TE_{m,n}$ modes. Therefore the longitudinal magnetic field will be :

$$H_z(x, y) = H_0 \cos k_x x \cos k_y y. \quad \textbf{(2.43)}$$

The equations (2.26, 2.27 and 2.28) then have solutions:

$$H_x(x, y) = H_1 \sin k_x x \cos k_y y \quad \textbf{(2.44)}$$

$$H_y(x, y) = H_2 \sin k_y y \cos k_x x \quad \textbf{(2.45)}$$

$$E_x(x, y) = E_1 \sin k_x x \cos k_y y \quad \textbf{(2.46)}$$

$$E_y(x, y) = E_2 \sin k_y y \cos k_x x, \quad \textbf{(2.47)}$$

where the constants are:

$$H_1 = \frac{j\beta k_x}{k_c^2} H_0 \text{ , } H_2 = \frac{j\beta k_y}{k_c^2} H_0$$

$$E_1 = j\eta \frac{\omega k_y}{\omega_c k_c} H_0 \text{ , } E_2 = -j\eta \frac{\omega k_x}{\omega_c k_c} H_0.$$

where

$$|H_0| = \frac{k_c^2}{\omega\mu\pi} \sqrt{\frac{4ab}{m^2a^2 + n^2b^2}}.$$

The fundamental mode for a rectangular waveguide is the TE_{10} mode (n = 1, m = 0). More modes can propagate by increasing the frequency of the radiation. The order in which the modes propagate depends on the dimensions of the waveguide but most rectangular waveguides have dimensions $a = 2b$. Below is a table (Table 2.1) of the order of mode excitation for a waveguide with dimensions $a = 2b$. Figure 2.2 shows 2D plots of a few low order modes.

Order of mode excitation	
1	TE_{01}, TE_{10}
2	TE_{20}
3	TE_{11},TM_{11}
4	TE_{21},TM_{21}
5	TE_{30}
6	TE_{31},TM_{31}

Table 2.1 The order of mode excitation for a rectangular waveguide with *a=2b*.

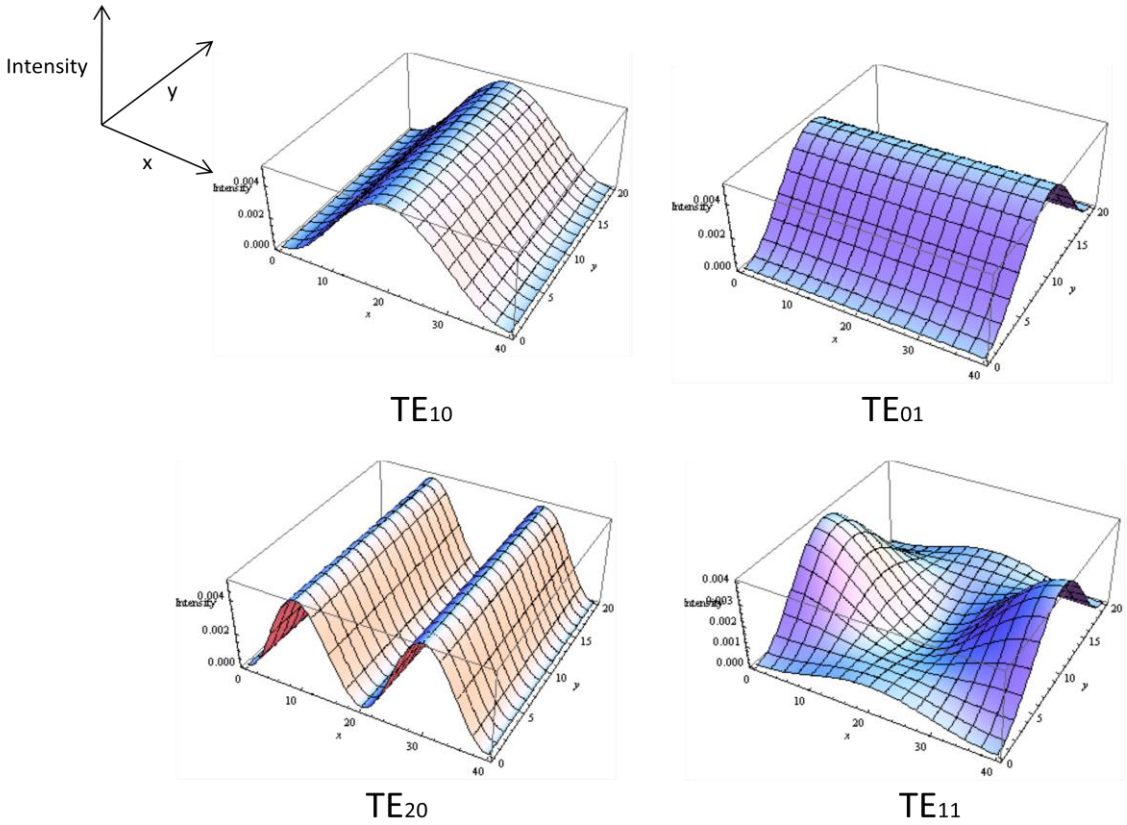

Figure 2.2 2D plots of low order TE modes

Rectangular Waveguide TM modes

The expressions for the TM modes are obtained in the same way. We assume $E_z = F(x)\,G(y)$, and use the solutions $F(x) = \sin k_x x$ and $G(y) = \sin k_y y$. The equations will become:

$$H_z(x,y) = H_0 \cos k_x x \cos k_y y \qquad \textbf{(2.48)}$$

for the longitudinal components and

$$H_x(x,y) = H_1 \sin k_y y \cos k_x x, \quad \textbf{(2.49)}$$

$$H_y(x,y) = H_2 \sin k_x x \cos k_y y, \quad \textbf{(2.50)}$$

$$E_x(x,y) = E_1 \sin k_y y \cos k_x x, \quad \textbf{(2.51)}$$

$$E_y(x,y) = E_2 \sin k_x x \cos k_y y, \quad \textbf{(2.52)}$$

for the transverse components where the constants are:

$$E_1 = -\frac{j\beta k_x}{k_c^2} E_0 \ , E_2 = -\frac{j\beta k_y}{k_c^2} E_0,$$

$$H_1 = \frac{j}{\eta} \frac{\omega k_y}{\omega_c k_c} E_0 \ , H_2 = \frac{j}{\eta} \frac{\omega k_y}{\omega_c k_c} E_0.$$

and

$$|E_0| = \frac{k_c^2}{\beta\pi} \sqrt{\frac{4ab}{m^2a^2+n^2b^2}}.$$

Figure 2.3 shows plots of some low order TM modes

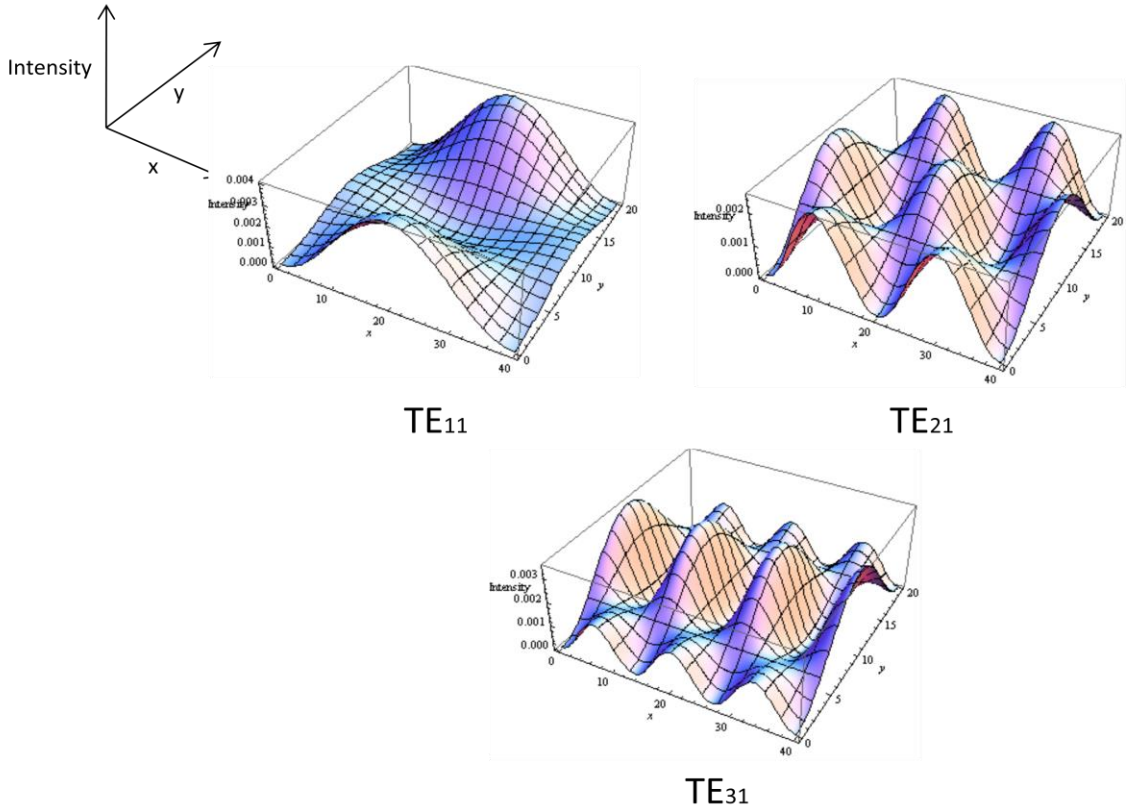

Figure 2.3 2D plots of low order TM modes

2.2.3 Cylindrical Waveguides

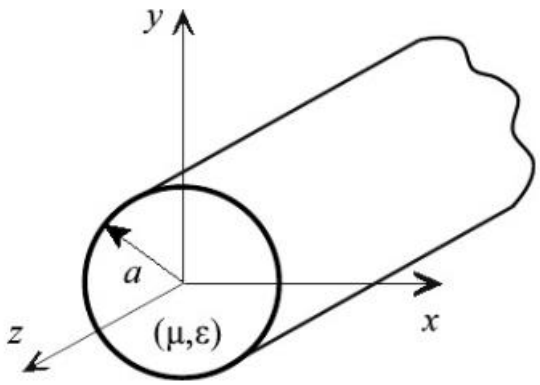

Figure 2.4 Circular waveguide [29]

We now consider a cylindrical waveguide of radius *a*, again with the cross-section in the *x*-*y* plane and the radiation propagating in the *z* direction (Figure 2.4). In this case, since it is a cylindrical geometry that we are dealing with, it is convenient to use cylindrical coordinates. The transverse field components are:

$$\mathbf{E_T} = \hat{\boldsymbol{\rho}} E_\rho + \hat{\boldsymbol{\phi}} E_\phi \quad \textbf{(2.53)}$$

$$\mathbf{H_T} = \hat{\boldsymbol{\rho}} H_\rho + \hat{\boldsymbol{\phi}} H_\phi \quad \textbf{(2.54)}$$

Using Maxwell's equations (where the curl is applied in cylindrical coordinates) leads us to:

$$H_\rho = \frac{j}{k_c^2}\left(\frac{\omega\epsilon}{\rho}\frac{\partial E_z}{\partial \phi} - \beta\frac{\partial H_z}{\partial \rho}\right) \quad \textbf{(2.55)}$$

$$H_\phi = \frac{-j}{k_c^2}\left(\omega\epsilon\frac{\partial E_z}{\partial \rho} - \frac{\beta}{\rho}\frac{\partial H_z}{\partial \phi}\right) \quad \textbf{(2.56)}$$

$$E_\rho = -\frac{j}{k_c^2}\left(\beta\frac{\partial E_z}{\partial \rho} - \frac{\omega\mu}{\rho}\frac{\partial H_z}{\partial \phi}\right) \quad \textbf{(2.57)}$$

$$E_\phi = -\frac{j}{k_c^2}\left(\frac{\beta}{\rho}\frac{\partial E_z}{\partial \phi} - \omega\mu\frac{\partial H_z}{\partial \rho}\right) \quad \textbf{(2.58)}$$

where the symbols have their usual meanings. Cylindrical waveguides can only support TE and TM modes.

Cylindrical Waveguide TE modes

We assume that we have a wave that propagates as $e^{-j\beta z}$. The wave equation for H_z is given as:

$$(\nabla^2 + k^2)H_z = 0 \quad \textbf{(2.59)}$$

which in cylindrical coordinates is:

$$\left(\frac{\partial^2}{\partial \rho^2} + \frac{1}{\rho}\frac{\partial}{\partial \rho} + \frac{1}{\rho^2}\frac{\partial^2}{\partial \phi^2} + \frac{\partial^2}{\partial z^2} + k^2\right)H_z(\rho, \phi, z) = 0. \quad \textbf{(2.60)}$$

We use the separation of variables method, letting $H_z(\rho, \phi, z) = R(\rho)P(\phi)e^{-j\beta z}$, and we obtain:

$$\left(R^{"}P + \frac{1}{\rho}R'P + \frac{1}{\rho^2}RP^{"} + (k^2 - \beta^2)RP\right)e^{-j\beta z} = 0\,. \quad \textbf{(2.61)}$$

Then by multiplying by a common factor this leads to

$$\rho^2 \frac{R^{"}}{R} + \rho \frac{R\prime}{R} + \rho^2 k_c^2 + \frac{P"}{P} = 0\ . \qquad \textbf{(2.62)}$$

All the terms in this equation sum up to a constant and only depend on a single coordinate; therefore each term must be a constant:

$$\frac{P"}{P} = -k_\phi^2 \ \ \rightarrow \ \ P" + k_\phi^2 P = \ 0, \qquad \textbf{(2.63)}$$

so that

$$P(\phi) = A_0 \sin\left(k_\phi \phi\right) + B_0 \cos\left(k_\phi \phi\right). \qquad \textbf{(2.64)}$$

Now using this result in equation 2.57 leads to

$$\rho^2 \frac{R"}{R} + \rho \frac{R\prime}{R} + \left(\rho^2 k_c^2 - k_\phi^2\right) = 0. \qquad \textbf{(2.65)}$$

This equation is known as Bessel's Differential Equation. This equation can be solved using a method called the Frobenius Method. The solution we obtain is:

$$R(\rho) = C_0 J_{k_\phi}(k_c \rho) + D_0 N_{k_\phi}(k_c \rho) \qquad \textbf{(2.66)}$$

where $J_v(x)$ is the Bessel function of the first kind of order *v* and $N_v(x)$ is the Bessel function of the second kind of order *v*. Now using the values we obtained for $R(\rho)$ and $P(\phi)$ we get:

$$H_z(\rho, \phi, z) = \left(A_0 \sin\left(k_\phi \phi\right) + B_0 \cos(k_\phi \phi)\right)\left(C_0 J_{k_\phi}(k_c \rho) + D_0 N_{k_\phi}(k_c \rho)\right) e^{-j\beta z} \qquad \textbf{(2.67)}$$

and we have $H_z(\rho, \phi, z) = \ H_z(\rho, \phi + 2\pi l, z)$ where *l* is an integer. This can only be true if $k_\phi = v$ where *v* is an integer and

$$H_z(\rho,\phi,z) = \left(A_0 \sin\left(k_\phi \phi\right) + B_0 \cos(k_\phi \phi)\right)(C_0 J_v(k_c\rho) + D_0 N_v(k_c\rho))e^{-j\beta z}.$$

(2.68)

However, $N_v(k_c\rho) \to -\infty$ as $\rho \to 0$ and $\rho = 0$ is in the domain of the waveguide so we cannot have an infinite wave intensity at this point. We therefore conclude that $D_0 = 0$ and $C_0 = 1$. So now we are left with:

$$H_z(\rho,\phi,z) = \left(A_0 \sin\left(k_\phi \phi\right) + B_0 \cos(k_\phi \phi)\right)J_v(k_c\rho)e^{-j\beta z}. \quad \textbf{(2.69)}$$

The values of A_0 and B_0 are related to the absolute coordinate frame we use to define the waveguide. We let $A_0 = F\cos(v\phi_0)$ and $B_0 = -F\sin(v\phi_0)$. Then we have:

$$A_0 \sin\left(k_\phi \phi\right) + B_0 \cos(k_\phi \phi) = F\sin(v(\phi - \phi_0))\,. \quad \textbf{(2.70)}$$

The value of ϕ_0 that makes this work can be thought of as the coordinate reference for measuring ϕ. So now we're only left with finding the value of F, which is the mode amplitude and is therefore determined by the excitation. We are now left with the z-component of the H field:

$$H_z = F\sin(v\phi)J_v(k_c\rho)e^{-j\beta z}\,. \quad \textbf{(2.71)}$$

From this expression for H_z the remaining transverse components are derived as [30]

$$E_{vl,\rho} = C_{vl}\left[\frac{vJ_v(k_c\rho)}{k_c\rho}\right]\cos v\phi\; e^{-j\beta z} \quad \textbf{(2.72)}$$

$$E_{vl,\phi} = -C_{vl}J'_v(k_c\rho)\;\sin v\phi\; e^{-j\beta z} \quad \textbf{(2.73)}$$

$$H_{vl,\rho} = \frac{C_{vl}}{Z_{TE}}J'_v(k_c\rho)\;\sin v\phi\; e^{-j\beta z} \quad \textbf{(2.74)}$$

$$H_{vl,\rho} = \frac{C_{vl}}{Z_{TE}}\left[\frac{vJ_v(k_c\rho)}{k_c\rho}\right]\cos v\phi\; e^{-j\beta z} \quad \textbf{(2.75)}$$

where $C_{vl} = \frac{-j\omega\mu F}{k_c}$ and $J'_v = \frac{dJ_v(z)}{dz}$ is the derivative of the Bessel function J_v with respect to this argument. The E-field along the surface of a perfect conductor must be zero and therefore $E_z = 0$ at $\rho = a$. This means that $J'_v(k_c\rho)=0$ and therefore the argument of the derivative of the Bessel function must be one of its roots. That is,

$$k_c a = \frac{2\pi a}{\lambda_c} = \omega_c\sqrt{\mu\epsilon}a = p'_{vl}$$

where p'_{vl} is the l^{th} root of the derivative of the *v* th order of the Bessel function J'_v, the values of which are given in Table 2.2 The cut-off frequency for any TE circular waveguide can be calculated by using $k_c = \frac{p'_{vl}}{a}$. Also the wave impedance is given by

$$Z_{TE,vl} = \frac{Z_0}{\sqrt{1 - \left(\frac{p'_{vl}\lambda_0}{2\pi a n_d}\right)^2}}$$

where $n_d = \sqrt{\mu\epsilon}$ is the refractive index of the waveguide medium, $Z_0 = \eta$ is the characteristic impedance of the waveguide medium. Figure 2.5 shows plots of low-order TEmodes.

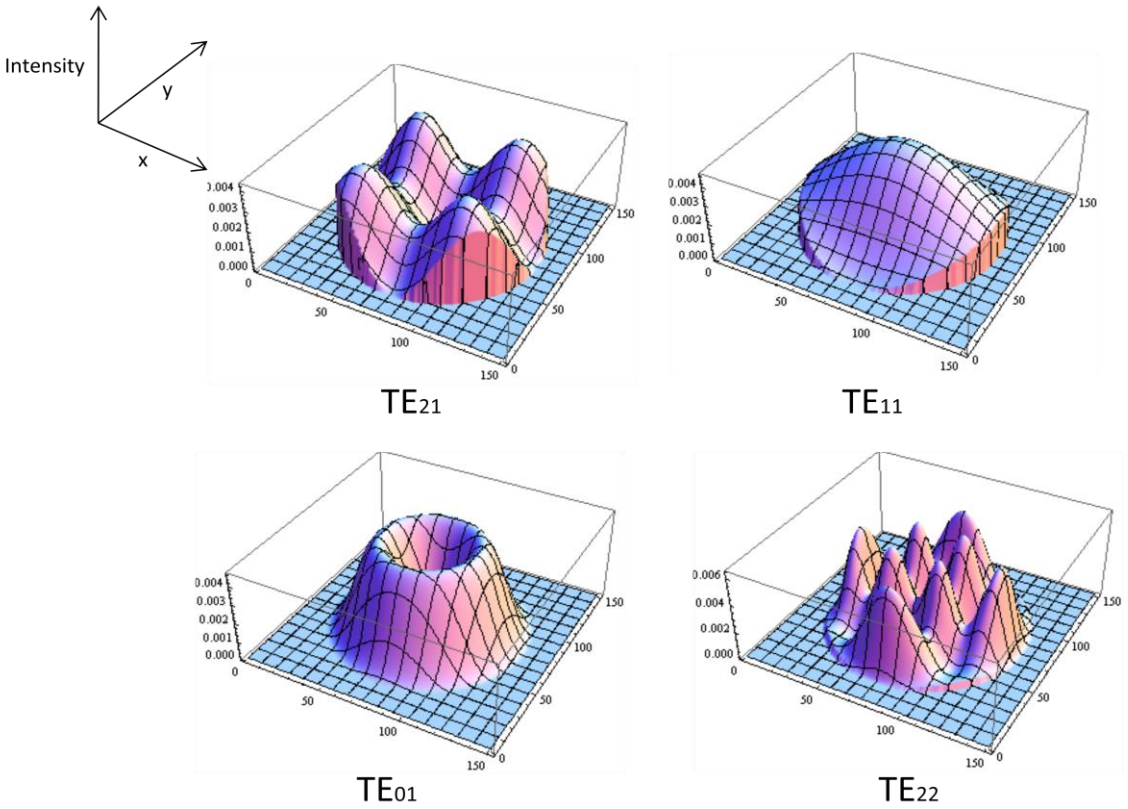

Figure **2.5** Plots of some TE circular waveguide modes.

$J'_\nu(k_c a) = 0$	$n = 1$	$n = 2$	$n = 3$
$\nu = 0$	0.0000	3.8317	7.0156
$\nu = 1$	1.8412	5.3314	8.5363
$\nu = 2$	3.0542	6.7061	9.9695

Table 2.2 The roots of the derivative of bessel functions of different orders (*v*).

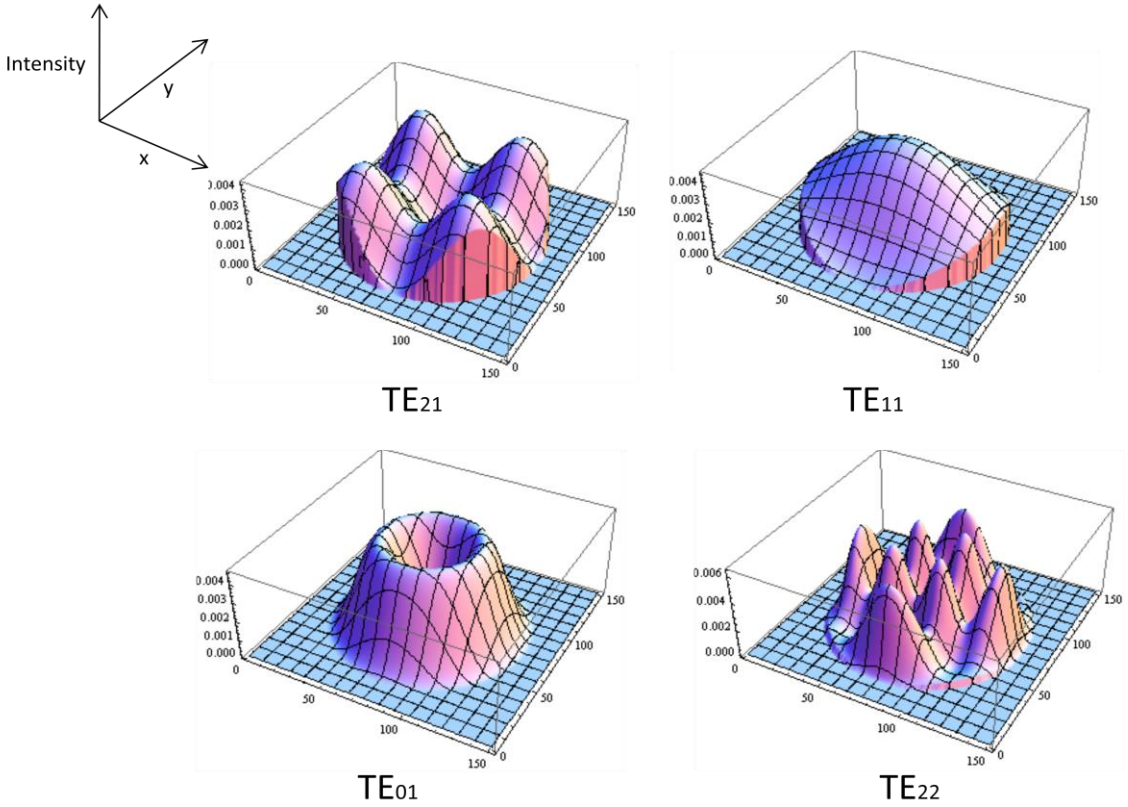

Figure 2.5 Plots of low order TE circular waveguide modes.

Cylindrical Waveguide TM modes

For the TM modes of the circular waveguide we solve the wave equation for E_z giving

$$E_{vl,z} = B_{vl}\cos(v\phi)J_v(k_c\rho)e^{-j\beta z}\ . \tag{2.76}$$

Just like the TE modes this can be used to derive the transverse field components which are given by [31],

$$E_{vl,\rho} = D_{vl}J'_v(k_c\rho)\cos v\phi e^{-j\beta z}\ , \tag{2.77}$$

$$E_{vl,\phi} = D_{vl}\left[\frac{vJ_v(k_c\rho)}{k_c\rho}\right] - \sin v\phi\ e^{-j\beta z}, \tag{2.78}$$

$$H_{vl,\rho} = -\frac{D_{vl}}{Z_{TM}}\left[\frac{vJ_v(k_c\rho)}{k_c\rho}\right] - \sin v\phi\ e^{-j\beta z}, \tag{2.79}$$

$$H_{vl,\phi} = \frac{D_{vl}}{Z_{TM}} J'_v(k_c\rho)\cos v\phi\, e^{-j\beta z}, \qquad \textbf{(2.80)}$$

where $C_{vl} = \frac{-j\beta B_{nl}}{k_c}$. Again, like the TE modes the E-field along the surface of a perfect conductor must be zero and therefore E_z = 0 at ρ = a. This means that $J_v(k_c\rho)$=0 and therefore the argument of the Bessel function must be one of its roots. That is,

$$k_c a = \frac{2\pi a}{\lambda_c} = \omega_c\sqrt{\mu\epsilon}a = p_{vl}$$

where p_{vl} is the l^{th} root of the *v*th order of the Bessel function J_v, the values of which are given in Table 2.3. The cut-off frequency for any TM circular waveguide mode can be calculated by using $k_c = \frac{p_{vl}}{a}$. Also the wave impedance is given by

$$Z_{TM,vl} = Z_0\sqrt{1 - \left(\frac{p_{vl}\lambda_0}{2\pi a n_d}\right)^2}.$$

where the variables have the same definitions as before. Plots of some low-oreder TM modes are shown in Figure 2.6.

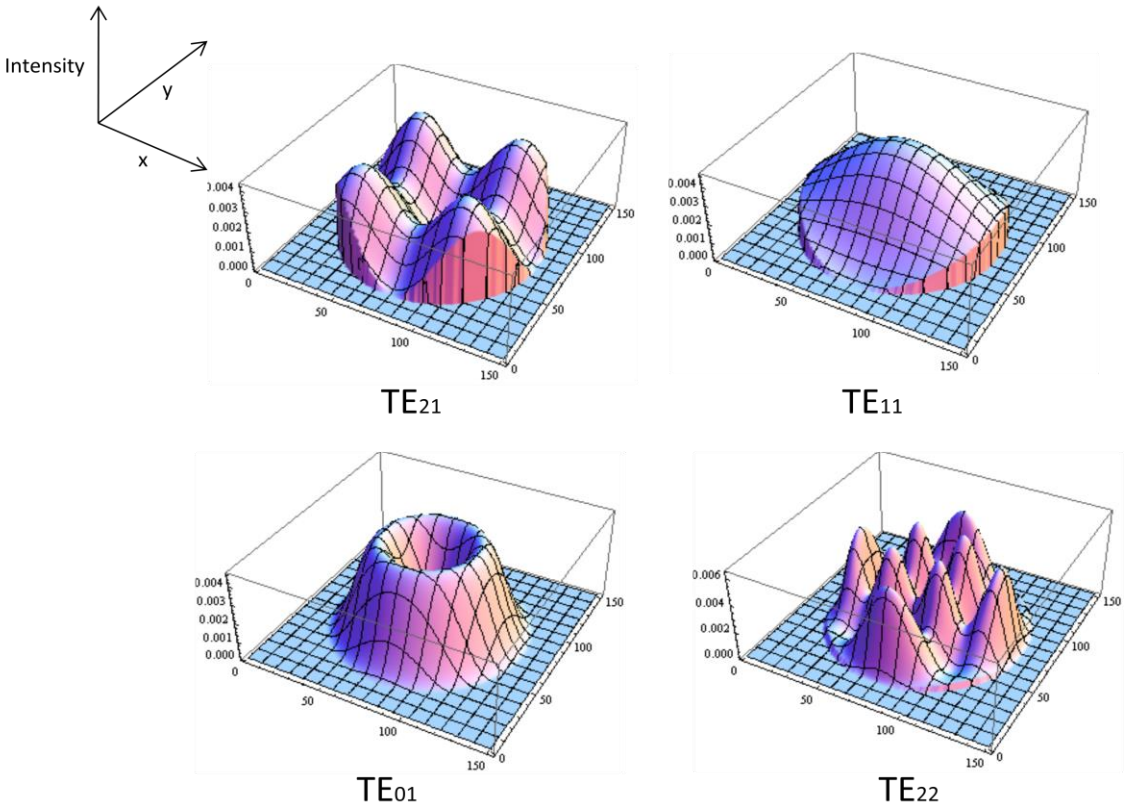

Figure **2.5** shows some of the TM circular waveguide modes.

$J_\nu(k_c a) = 0$	$n = 1$	$n = 2$	$n = 3$
$\nu = 0$	2.4048	5.5201	8.6537
$\nu = 1$	3.8317	7.0156	10.1735
$\nu = 2$	5.1356	8.4172	11.6198

Table 2.3 The roots of the bessel functions of different orders.

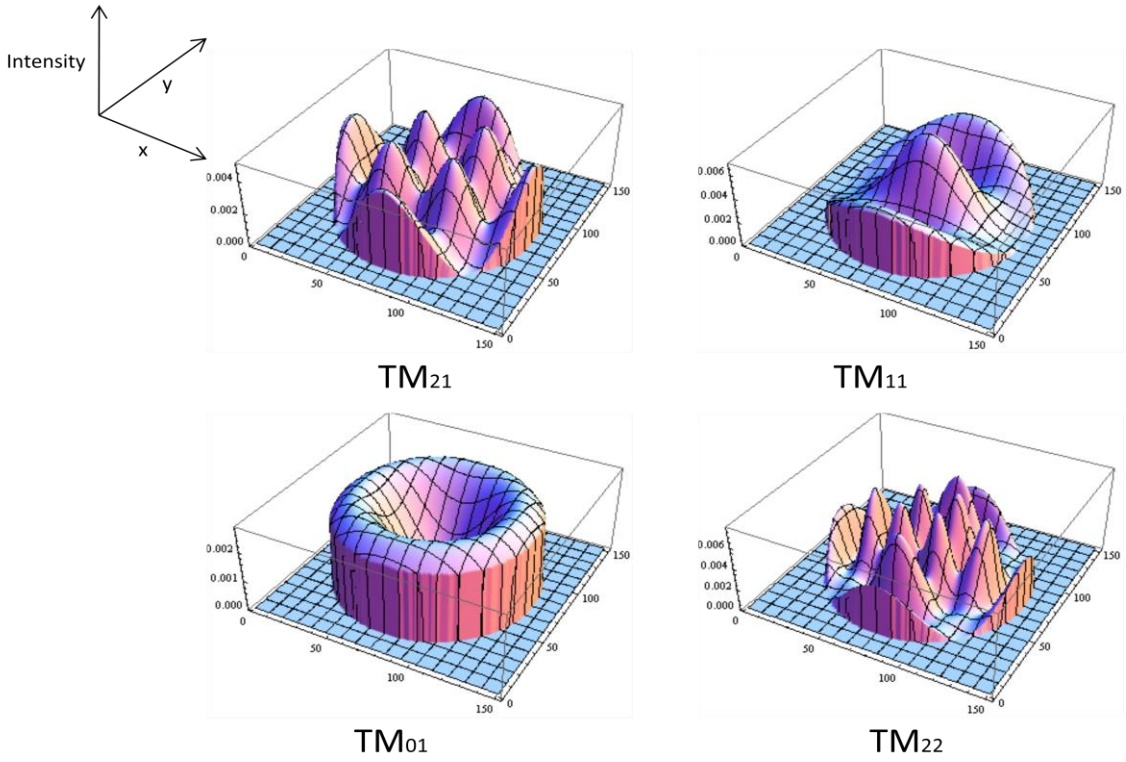

Figure 2.6 Plots of the low order TM circular waveguide modes.

2.3 Corrugated Horns

The principal application of conical corrugated horns (fed by waveguides) is to produce a symmetrical beam pattern with low side lobes and low cross-polarization as shown in Figure 2.7 and 2.8.

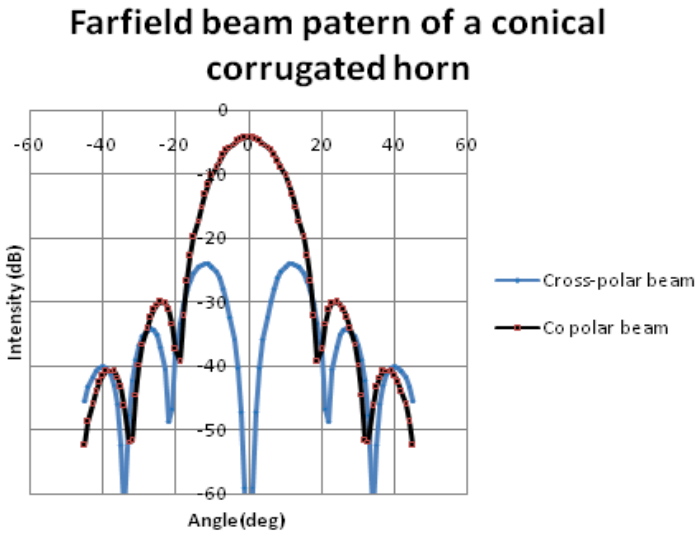

Figure 2.7 The ideal beam and cross-polarization pattern of a conical corrugated horn, calculated using Scatter code.

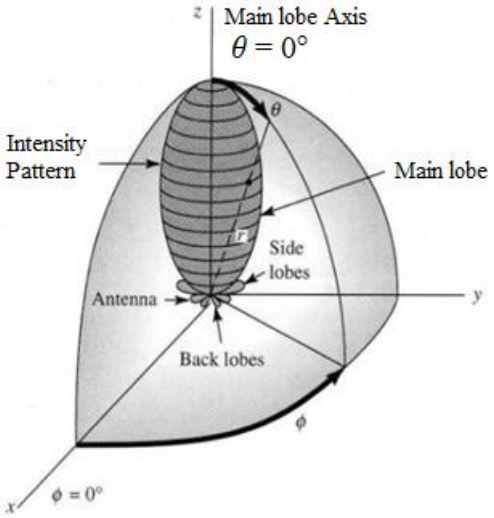

Figure 2.8 An almost perfect beam showing the symmetry of the main beam with low side-lobes.

Producing this beam symmetry requires a uniform field distribution which cannot be produced with only a TE_{11} or TM_{11} mode propagating because both of these modes have asymmetric aperture electric fields. The only way to produce the desired field distribution is to form a hybrid mode which is produced by taking the sum of both the TE_{11} and TM_{11} modes as shown in Figure 2.9. To achieve this, the hybrid boundary conditions need to be met. These conditions are met by corrugating on the wall of the horn. The corrugations of depth R provide a reactance to the impedance of free space given by

$$\frac{\boldsymbol{X_s}}{\boldsymbol{Z_0}} = \tan\left(\frac{2\pi R}{\lambda}\right).$$

where X_s is the reactance and Z_0 is the impedance of free space.

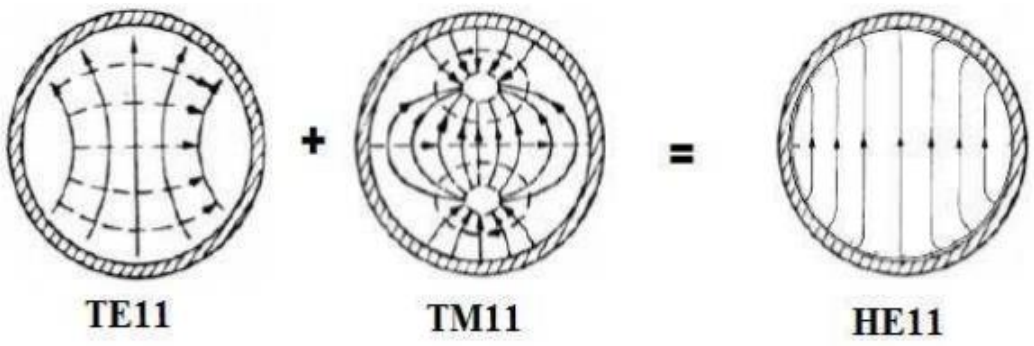

Figure 2.9 The sum of TE and TM modes [32].

A hybrid-mode has aperture elecric field [32]:

$$E_x = A_1.J_0.(Kr) - \frac{(X-Y)}{kr_1}.A_2.J_2.(Kr).\cos 2\phi, \quad \textbf{(2.81)}$$

$$E_y = \frac{(X-Y)}{kr_1}.A_2.J_2.(Kr).\sin 2\phi, \quad \textbf{(2.82)}$$

where $J_0(kr)$ and $J_2(Kr)$ are the Bessel functions of the first kind, K and k are transverse and free space wave numbers, A_1 and A_2 are the amplitude coefficients and X and Y are the impedance and admittance at the boundary $r = r_1$ given by:

$$X = -j.\frac{E_\emptyset}{H_z}.y_0,$$

$$Y = +j.\frac{H_\emptyset}{E_z}.y_0,$$

and y_0 is the admittance of free space.

If the corrugation depth is equal to $\frac{\lambda}{4}$ then both X and Y are zero. The desired balanced hybrid mode is then achieved because the electric and magnetic fields are balanced to produce pattern symmetry and low cross-polarization. When the term (X-Y) vanishes the aperture field is independent of the angular variable ϕ and $E_y = 0$ so that no cross-polarised field exists.

In many cases we have a non-standard corrugated horn design which we must model numerically. In the work described in this thesis two simulation software packages were used, and these are described next.

2.4 CST Studio Suite

In this section the use of CST Studio Suite in the analysis of horn antennas is discussed. CST is a commercial software package which performs electromagnetic simulations using the finite integration technique (FIT), a technique proposed by Weiland in 1977 [33]. Instead of discretising the differential form of Maxwell's equations, like other numerical methods, FIT discretises the integral form:

$$\oint \mathbf{E}(t) \cdot \widehat{\mathbf{dl}} = -\frac{d}{dt} \int \mathbf{B}(t) \cdot \widehat{\mathbf{ds}}, \tag{2.83}$$

$$\oint \mathbf{H}(t) \cdot \widehat{\mathbf{dl}} = \frac{d}{dt} \int \mathbf{D}(t) \cdot \widehat{\mathbf{ds}} + \int \bar{J}(t) \cdot \widehat{\mathbf{ds}}, \tag{2.84}$$

$$\oint \mathbf{D}\,(t) \cdot \widehat{\mathbf{ds}} = \int \rho_v(t)\, dv, \tag{2.85}$$

$$\oint \mathbf{B}(t) \cdot \widehat{\mathbf{ds}} = 0. \tag{2.86}$$

To solve these equations a finite calculation domain needs to be defined. This calculation domain encloses the system that is to be analysed eg. a corrugated horn or waveguide. This domain is split into small segments by a meshing system. CST uses two mesh systems, the primary mesh which can be viewed in CST using the "Mesh View" option, and a second internal mesh which is orthogonal to the primary one (Figure 2.10).

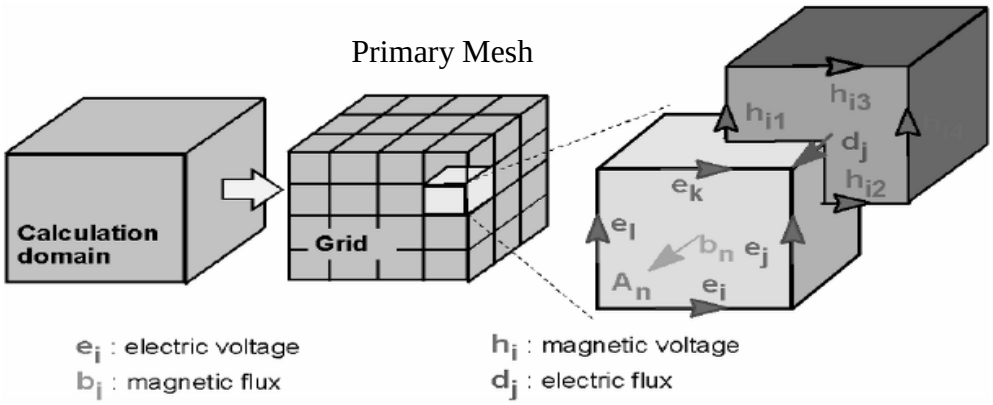

Figure 2.10 Image of CST mesh system [24].

The discretisation of Maxwell's equations is performed on these two orthogonal grid systems. They are formulated for each cell individually. To illustrate the FIT technique we consider Faraday's Law (equation 2.83)

$$\oint \mathbf{E}(t) \cdot \widehat{\mathbf{dl}} = -\frac{d}{dt} \int \mathbf{B}(t) \cdot \widehat{\mathbf{ds}}. \qquad \textbf{(2.87)}$$

The left hand side of this equation can be rewritten in terms of the four grid electric voltages and for the right hand side of the equation we get the time derivative of the magnetic field.

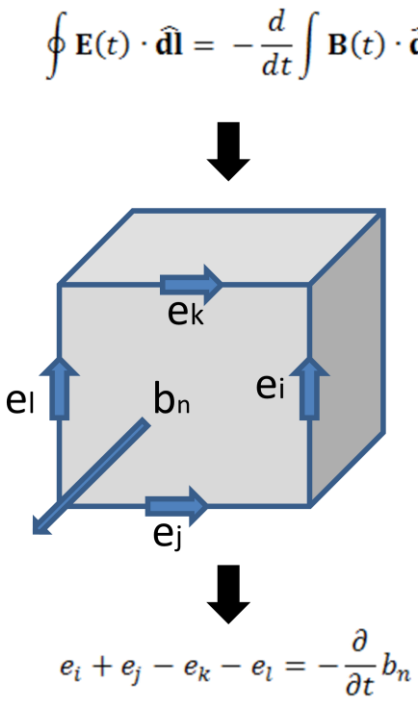

Figure 2.11 Substituting parts of Maxwell's equation with the four grid electric voltages and the time derivative of the magnetic field [24].

If we apply this to all cells we can summarise the calculation in a matrix formulation where we introduce a discrete matrix operator **C** which consists of elements such as '0', '1', and '-1'. This gives us equation 2.88 which is the discrete form of Maxwell's first equation.

$$\underbrace{\begin{pmatrix} \vdots & \vdots & \vdots & \vdots \\ 1 & 1 & -1 & -1 \\ \vdots & \vdots & \vdots & \vdots \end{pmatrix}}_{\mathbf{C}} \underbrace{\begin{pmatrix} e_i \\ \vdots \\ e_j \end{pmatrix}}_{e} = -\frac{d}{dt} \underbrace{\begin{pmatrix} \vdots \\ b_n \\ \vdots \end{pmatrix}}_{b} .$$

$$\mathbf{C}\boldsymbol{e} = -\frac{d}{dt}\mathbf{b} \qquad \textbf{(2.88)}$$

When we apply the same technique to Ampère's law, where we use the internal mesh system, we define a new discrete matrix operator $\tilde{\mathbf{C}}$. Similarly the discretization of the remaining Maxwell's equations introduces discrete divergence operators $\mathbf{S}$ and $\tilde{\mathbf{S}}$. This gives us the discrete forms of Maxwell's equations.

$$\mathbf{Ce} = -\frac{d}{dt}\mathbf{b}, \tag{2.89}$$

$$\tilde{\mathbf{C}}\mathbf{h} = -\frac{d}{dt}\mathbf{d} + \mathbf{j}, \tag{2.90}$$

$$\tilde{\mathbf{S}}\mathbf{d} = \mathbf{q}, \tag{2.91}$$

$$\mathbf{Sb} = 0. \tag{2.92}$$

To account for the numerical inaccuracies due to spatial discretization CST defines relations between voltages and fluxes, and their integral values are approximated over the grid edges and cell areas. The resulting coefficients depend on the averaged material parameters as well as the number of grid cells and are summarized in matrices :

$$\mathbf{D} = \varepsilon\mathbf{E} \quad \rightarrow \quad \mathbf{d} = \mathbf{M}_{\boldsymbol{\varepsilon}}\mathbf{e} \tag{2.93}$$

$$\mathbf{B} = \mu\mathbf{H} \quad \rightarrow \quad \mathbf{b} = \mathbf{M}_{\boldsymbol{\mu}}\mathbf{h} \tag{2.94}$$

$$\mathbf{J} = \sigma\mathbf{E} + \mathbf{J}_{\mathbf{s}} \quad \rightarrow \quad \mathbf{j} = \mathbf{M}_{\boldsymbol{\sigma}}\mathbf{e} + \mathbf{j}_{\mathbf{s}} \tag{2.95}$$

2.4.1 CST Solver

CST offers three solvers that work for high-frequency electromagnetic field problems. They are the Transient, Frequency Domain and Eigenmode solvers [24]. The work done in this thesis only concerned simulations carried out using the Transient solver. This solver is capable of running a simulation of a structure's behaviour over a wide frequency band in a single computation. It is a solver that is best suited for the analysis of devices with open boundaries or large dimensions.

The Transient solver is based on the descretized form of Maxwell's equations. It substitutes the central differences for time derivatives (equation 2.96 & 2.97).

$$e^{n+1/2} = e^{n-1/2} + \Delta t \mathrm{M}_{\epsilon}^{-1}\left(\hat{\mathrm{C}}\mathrm{M}_{\mu}^{-1} b^{n} + j_{s}^{n}\right), \quad \textbf{(2.96)}$$

$$b^{n+1} = b^{n} - \Delta t \hat{\mathrm{C}} \mathrm{e}^{n+1/2}. \quad \textbf{(2.97)}$$

The variables in the relations above are given by electric voltages and magnetic fluxes. Both variables are located alternately in time, and the approach implemented as a leap-frog scheme (figure below).

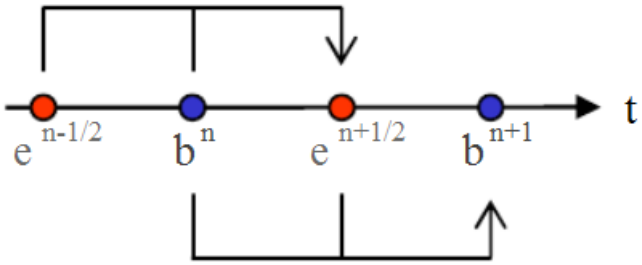

Figure 2.12 The leap frog scheme [24].

For an example, the magnetic flux at $t = (n+1)\Delta t$ is computed from the magnetic flux at the previous time step $t = n\Delta t$ and for the electric voltage at half a time step before, at $t = (n+1/2)\Delta t$.

2.4.2 CST Setup

Generating a CAD Model

The main work of this thesis deals with analysis of corrugated horn antennas, therefore corrugated horns will be used as an example for setting up a simulation in CST. The first step is to create a computer aided design (CAD) model of the object to be analysed. A CAD model can either be imported from a previously generated model, or created in CST using a macro called a .mcs file. This macro can read an ASCII file with details of the horns geometry. For the work in this thesis the macro used was called "Horn.mcs" from [34]. The lengths

and radii of the corrugations of the horn are written in two different .txt files and read by the macro. The macro then creates the horn out of a series of cylinders (Figure 2.13. The macro can be selected using the "macro" tab in CST).

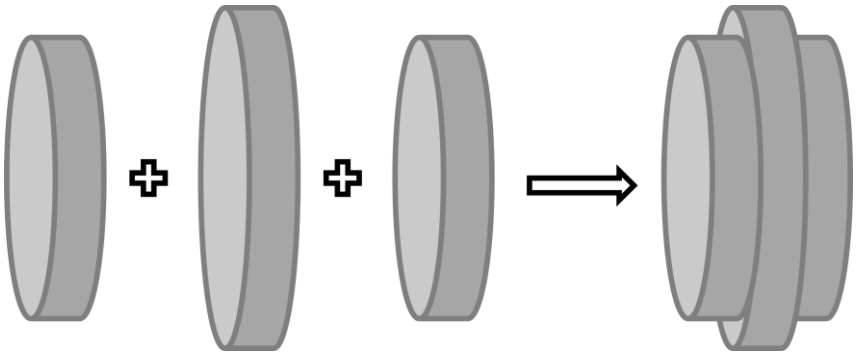

Figure 2.13 A series of cylinders illustrating the way in which CST generates horns.

The Simulation Set Up

Once the CAD model has been generated certain parameters need to be established. The first parameter is the frequency range which is set to cover the region the user is interested in. Next is the input port which is defined at the back of the horn. The port is where the horn is excited by a specific waveguide mode or modes. There is an option in CST to exploit the electrical boundaries of the model. The *yz* plane can be set as magnetically symmetric and the *xz* plane can be set as electrically symmetric (Figure 2.14). This reduces the computational time and power. However, it is important to ensure that the horn or waveguide is in reality symmetric. Another method of reducing computational time is to alter the mesh density which can be accessed using the "Mesh" tab in CST. Increasing and decreasing the number of lines per wavelength will alter the number of times a field is sampled. This option will increase or reduce the accuracy of the results. The work done in this thesis typically had the lines per wavelength set at 10. The

field monitors are then set up to record the E/M properties of the model. The type of solver is then selected and the simulation is then set running.

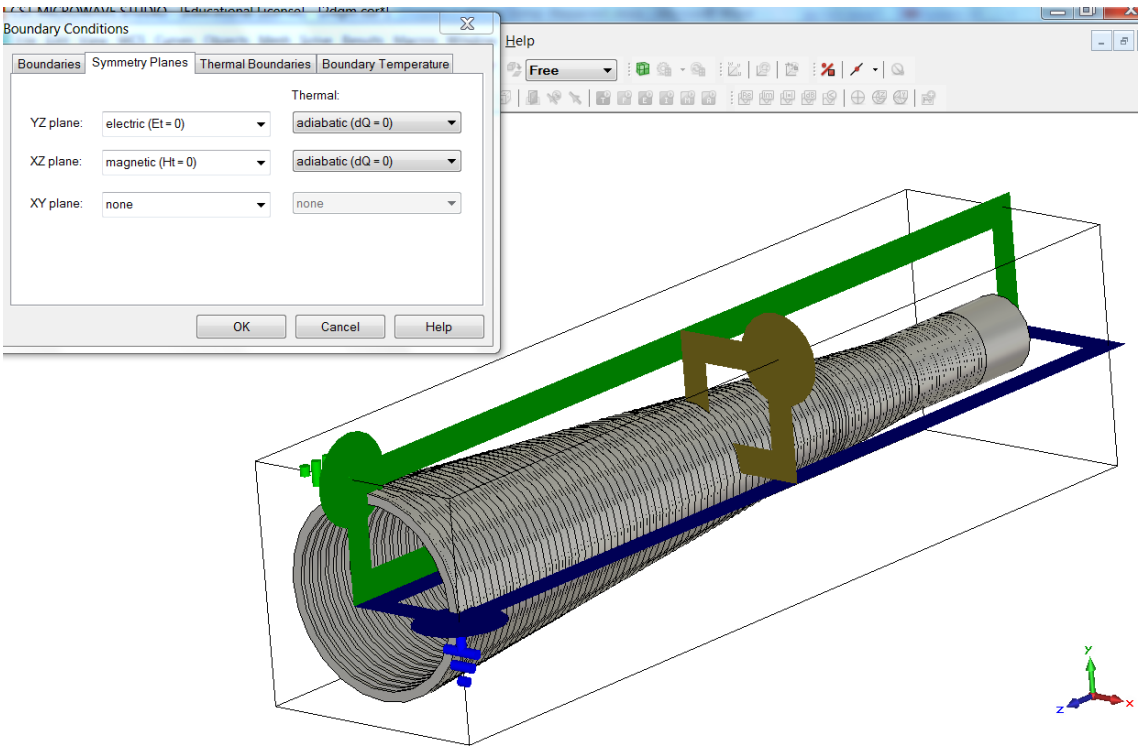

Figure 2.14 Setting up the symmetry planes to reduce computational time.

2.4.3 Advantages & Disadvantages

There are many advantages of using CST and they are as follows:

- CST models the exact system and the results obtained are very accurate as long as the sampling rate is sufficient.
- It can solve complex models.
- It can run an assembly of models.
- Models are easy to construct using CAD software and the simulations are easy to set up.
- It is flexible and can be used to analyse any optical components.

The disadvantages in using CST are:

- The larger and more complex the model is, the more computational power and time it uses.
- The time needed to obtain a simple far-field pattern from one horn can be several hours.

2.5 Scatter Matrix Method

This section discusses the use of mode matching and scatter matrices for analysing horn antennas. This method is implemented by the in-house software package called "Scatter"[25]. The Scatter code works by first dividing the corrugated horn into cylindrical or rectangular sections. Each section is described in terms of transmission and reflection for fields propagating both forwards and backwards within each section. Between the sections (but not within) power is scattered between the modes (TE/TM). In the mode-matching technique, the total transverse field in the two sections at a junction is matched so that total complex power is conserved. The scatter matrix describes these characteristics as the redistribution of power between waveguide modes.

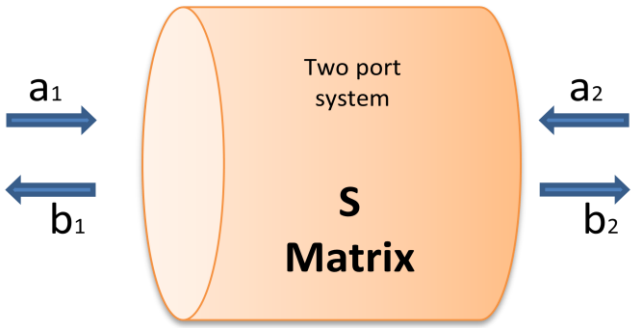

Figure 2.15 Schematic of the scatter matrix that describes the characteristics of a modular section of an optical system.

Letting [S] be the scatter matrix for the section to be analysed, the input and output mode coefficients are related through the following matrix equation:

$$\begin{bmatrix}[b_1]\\[b_2]\end{bmatrix} = [S]\begin{bmatrix}[a_1]\\[a_2]\end{bmatrix} \quad \textbf{(2.98)}$$

where $[a_1]$ and $[b_1]$ are the incident and reflected mode coefficients of the wave as viewed from the input side (Figure 2.15), and $[a_2]$ and $[b_2]$ are the incident and transmitted coefficients on the output side. To account for the scattering of forward and backward modes at the input and output, the matrix [S] is divided into sub-matrix components as shown by the following equation:

$$[S] = \begin{bmatrix}[S_{11}] & [S_{12}]\\[S_{21}] & [S_{22}]\end{bmatrix}. \quad \textbf{(2.99)}$$

We can now write that:

$$[b_1]=[S_{11}][a_1]+[S_{12}][a_2],\ [b_2]=[S_{21}][a_1]+[S_{22}][a_2]. \quad \textbf{(2.100)}$$

It is often assumed that there is no reflection back into the system and that the matrix $[a_2]$ is zero for that system. The reflection and transmission coefficients are then given by

$$[b_1]=[S_{11}][a_1],\ [b_2]=[S_{21}][a_1]. \quad \textbf{(2.101)}$$

The total transmission and reflection for optical systems are obtained by cascading the scatter matrices of each of the constituent subsystems, which are obtained by analysing each section separately. We let $[S^a]$ and $[S^b]$ be the two matrices that describe consecutive sections of an optical system and they have the form:

$$[S^a] = \begin{bmatrix}[S_{11}^a] & [S_{12}^a]\\[S_{21}^a] & [S_{22}^a]\end{bmatrix},\ [S^b] = \begin{bmatrix}[S_{11}^b] & [S_{12}^b]\\[S_{21}^b] & [S_{22}^b]\end{bmatrix}. \quad \textbf{(2.102)}$$

The cascaded matrix elements are then of the form

$$[S^c] = \begin{bmatrix} [S_{11}^c] & [S_{12}^c] \\ [S_{21}^c] & [S_{22}^c] \end{bmatrix} \quad \textbf{(2.103)}$$

with the cascade elements defined as [31]

$$[S_{11}^c] = [S_{12}^a][[I]\text{-}[S_{11}^b][S_{22}^a]]^{-1}\,[S_{11}^b][S_{21}^a]\text{+}[S_{11}^a] \quad \textbf{(2.104)}$$

$$[S_{12}^c] = [S_{12}^a][[I]\text{-}[S_{11}^b][S_{22}^a]]^{-1}[S_{12}^B] \quad \textbf{(2.105)}$$

$$[S_{21}^c] = [S_{21}^b][[I]\text{-}[S_{22}^b][S_{11}^a]]^{-1}[S_{21}^b] \quad \textbf{(2.106)}$$

$$[S_{22}^c] = [S_{21}^b][[I]\text{-}[S_{22}^a][S_{11}^b]]^{-1}\,[S_{22}^a][S_{12}^b]\text{+}[S_{22}^b] \quad \textbf{(2.107)}$$

where $[S^c]$ represents the cascaded matrix, $[I]$ is the identity matrix and $[\ ]^{-1}$ represents the inverse of the matrix. A complete matrix describing the propagation for all the modes in a quasi-optical system is obtained by cascading the scattering matrices for each section. The resulting mode coefficients at the horn aperature are then multiplied by individual fields to give the antenna output field.

Advantages & Disadvantages

The advantages of using the mode matching scatter matrix method are:

- It solves the near field and far-field analytically making it much faster that CST.
- It does not use a lot of computational power and can easily be left running in the background.
- It is cheaper to run compared to that of CST because it does not need a licence.

The disadvantages of using the Scatter matrix method are;

- It assumes horns are symmetric.

- It doesn't consider the last step (jump to free space) accurately.

2.6 Far-Field Beam Patterns

As the name suggests the far-field radiation pattern of a horn antenna is the region far away from the aperture of the horn. This region is often considered to be beyond a distance of $^{2D^2}/_{\lambda}$ where *D* is the maximum linear dimensions of the horn. In this region the radiation pattern doesn't change shape with propagation distance (Figure 2.16).

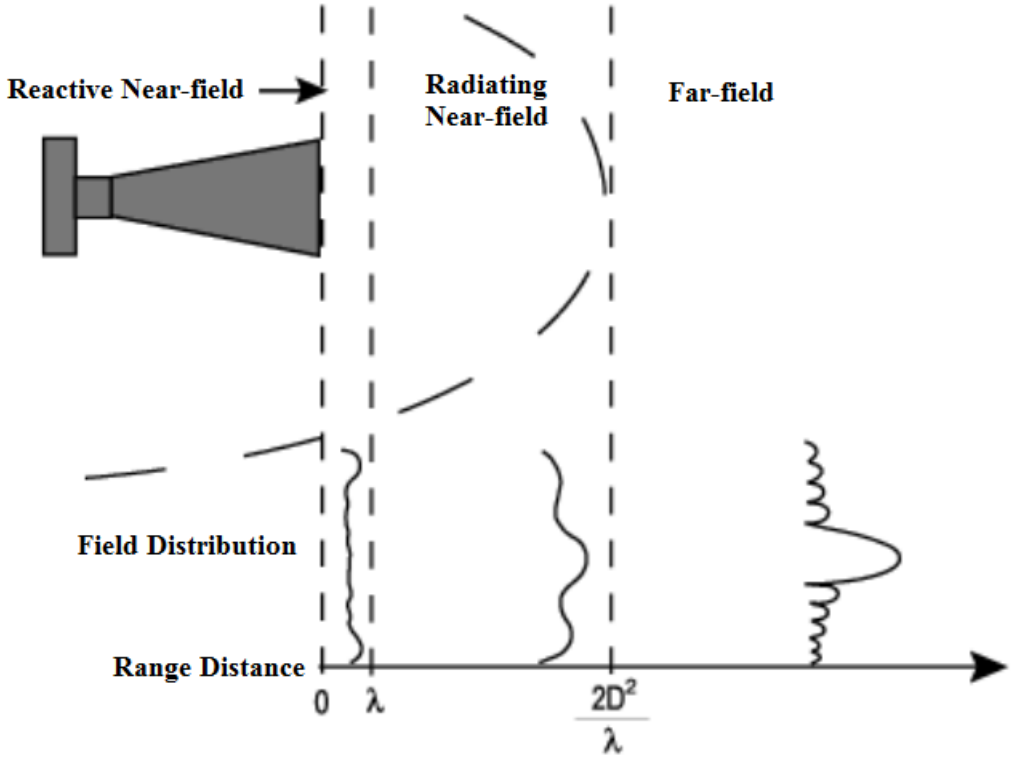

Figure 2.16 A diagram of the different radiation regions in front of a horn antenna.[35]

The far-field region is important for THz astronomy since the sources of the radiation are great distance away from the horn. From the theory of reciprocity, a horn antenna that is a good transmitter of radiation is a good receiver [36]. Accurately testing the far-field radiation emitted from a horn antenna is essential

in creating accurate models of CMB recievers. Both CST and Scatter calculate the far-field of the horn by Fourier transforming the aperature field.

2.7 Summary

In this chapter I have discussed the properties of waveguides and corrugated horns, and outlined the derivation of the forms of the TE and TM modes propagating in them. I have also described CST and Scatter, the two main methods used in the analysis of horn antennas in this thesis. I have discussed the advantages and disadvantages in using these two techniques. In the next Chapter I will discuss some modifications made to Scatter to improve its accuracy, in certain circumstances.

Chapter 3

Improvements to Scatter

3.1 Introduction

Extensive use is made of the mode-matching software Scatter throughout this thesis as it is significantly faster than finite-element software such as CST and can be used for cylindrically symmetric systems. Scatter was initially written in Mathematica [25] but a C version was also produced for flexibility and speed. In this chapter I describe some developments that were made to the C version of the code. These developments were useful for modelling work related to both the Planck and QUBIC CMB experiments.

3.2 Specification of horn geometries for Scatter

To analyse corrugated horns in Scatter a horn geometry file has to be input into it. A horn geometry file contains information about the horn, information such as its operating frequency, the number of modes (whether it is single or multi-moded - all horns used in this thesis were single moded) and the horn's dimensions (lengths and radii of the corrugations). Figure 3.1 shows a sample of a geometry file. The number of TE and TM modes to propagate through the horn was set in the Scatter user interface (in this thesis most simulations used 50 modes, 25 TE and 25 TM). The first line of the geometry file gives the frequency, the number of modes and the number of corrugations respectively. The second line gives the throat length of the horn (length of the first section). Then there is a series of values for the lengths of the corrugations and then values for the radii of the corrugations.

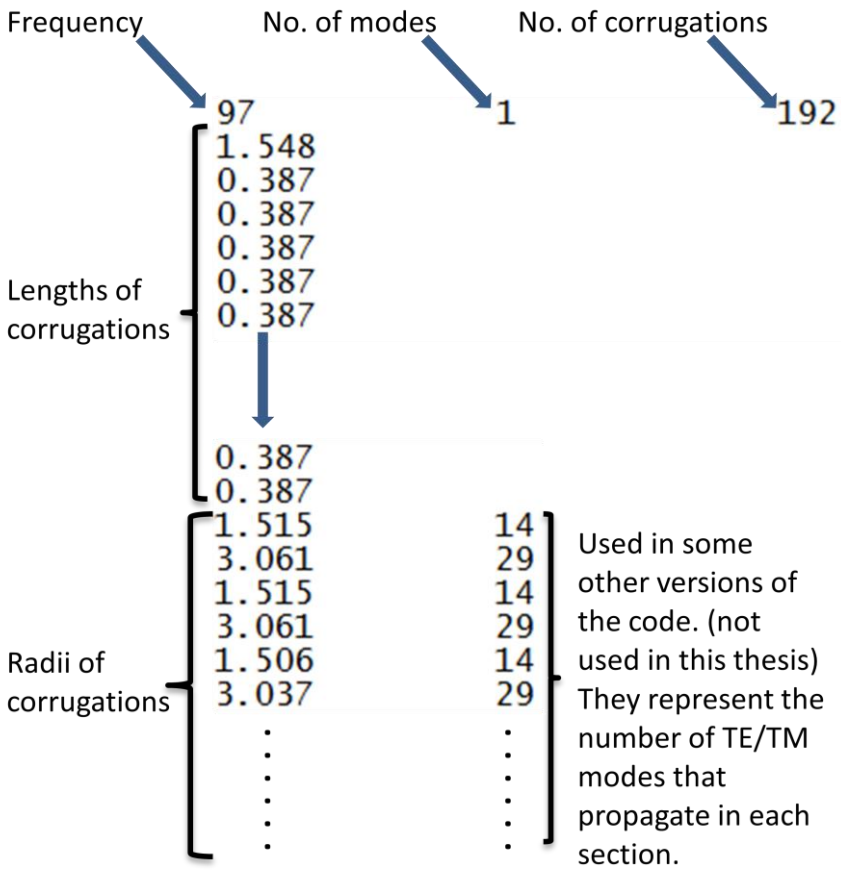

Figure 3.1 The different components of a horn geometry file.

3.3 Matrix Inversion

In certain cases it was found that Scatter produced unexpected results, such as wider than expected Planck beams at particular frequencies and very high sidelobes for horn with small gaps (discussed in Chapter 4). One possible cause for this is numerical instability in the matrix inversion routine. This routine is involved when cascading the scatter matrices for each junction. Equations 3.1 to 3.4 (same as equations 2.104-2.107) show how the matrices are cascaded with the matrix inversions highlighted.

$$[S_{11}^c] = [S_{12}^a][[I]-[S_{11}^b][S_{22}^a]]^{-1}\,[S_{11}^b][S_{21}^a]+[S_{11}^a] \quad \textbf{(3.1)}$$

$$[S_{12}^c] =[S_{12}^a][[I]-[S_{11}^b][S_{22}^a]]^{-1}[S_{12}^B] \quad \textbf{(3.2)}$$

$$[S_{21}^c] = [S_{21}^b][[I]-[S_{22}^b][S_{11}^a]]^{-1}[S_{21}^b] \quad \textbf{(3.3)}$$

$$[S_{22}^{c}] = [S_{21}^{b}][[I]-[S_{22}^{a}][S_{11}^{b}]]^{-1}\,[S_{22}^{a}][S_{12}^{b}]+[S_{22}^{b}]. \quad \textbf{(3.4)}$$

Ian McAuley, of NUI Maynooth, successfully replaced the matrix inversion in the Mathematica code with Mathematica's "PseudoInverse[]" routine. Here I discuss the pseudoinverse and describe how the equivalent can be done for the C version of the Scatter code.

3.4 The Pseudoinverse

The $m \times n$ matrix $\mathbf{A}^+$ is called the pseudoinverse of matrix **A** if $\mathbf{A}^+$ satisfies the four (Moore-Penrose) conditions:

- $\mathbf{A}\,\mathbf{A}^+\,\mathbf{A} = \mathbf{A}$ (i.e. A^+ is the generalised inverse of A)
- $\mathbf{A}^+\,\mathbf{A}\,\mathbf{A}^+ = \mathbf{A}^+$
- $\mathbf{A}\,\mathbf{A}^+$ is a symmetric matrix
- $\mathbf{A}^+\,\mathbf{A}$ is a symmetric matrix.

The matrix **A**+ is unique and always exists. (In the case of complex matrices, the symmetric condition is substituted by the condition of being Hermitian.) The pseudoinverse is also known as the Moore-Penrose pseudoinverse.

Singular Value Decomposition (SVD), is one of the most powerful and efficient techniques for finding the pseudoinverse of a matrix, and I have chosen to use it in Scatter. SVD is based on the theorem that any $m \times n$ matrix **A** can be written as the product of an $m \times n$ column-orthogonal matrix **U**, an $n \times n$ diagonal matrix **W** (whose elements are ≥ 0 and termed the *singular values*) and the transpose of an $n \times n$ orthogonal matrix **V**, that is

$$\mathbf{A} = \mathbf{U}\mathbf{W}\mathbf{V}^T \quad \textbf{(3.5)}$$

The matrices **U**, $\mathbf{V}^T$ and **W** are given by the SVD procedure.

$$\mathbf{W} = \begin{bmatrix} w_1 & 0 & 0 & \cdots & 0 \\ 0 & w_2 & 0 & \cdots & 0 \\ 0 & \vdots & w_3 & \cdots & 0 \\ \vdots & \vdots & \vdots & \ddots & \vdots \\ 0 & 0 & 0 & \cdots & w_n \end{bmatrix} \tag{3.6}$$

$$\mathbf{U}^T\mathbf{U} = \mathbf{1} \tag{3.7}$$

$$\mathbf{V}^T\mathbf{V} = \mathbf{1} \tag{3.8}$$

(in the case of Scatter we are always dealing with square matrices so $m = n$). For complex matrices the transpose is replaced by the conjugate transpose (also called the Hermitian transpose). Once the SVD of a matrix has been computed, the pseudoinverse is constructed as

$$\mathbf{A}^+ = \mathbf{V}\mathbf{W}^{-1}\mathbf{U}^T \tag{3.9}$$

if all the w_j are non-zero, while if one or more of the w_j are zero the best solution is given by

$$\mathbf{A}^+ = \mathbf{V}\bar{\mathbf{W}}^{-1}\mathbf{U}^T \tag{3.10}$$

where the inverse of the zero singular values are replaced with zeros:

$$\bar{\mathbf{W}}^{-1} = \begin{bmatrix} \frac{1}{w_1} & 0 & \cdots & 0 & 0 & \cdots & 0 \\ 0 & \frac{1}{w_2} & \cdots & 0 & 0 & \cdots & 0 \\ \vdots & \vdots & \ddots & \vdots & \vdots & \cdots & \vdots \\ 0 & 0 & \cdots & \frac{1}{w_N} & 0 & \cdots & 0 \\ 0 & 0 & \cdots & 0 & 0 & \cdots & 0 \\ \vdots & \vdots & \vdots & \vdots & \vdots & \ddots & \vdots \\ 0 & 0 & \cdots & 0 & 0 & \cdots & 0 \end{bmatrix}. \tag{3.11}$$

It can happen that some of the w_j's are very small but non-zero so that **W** is ill-conditioned. In this case each reciprocal should also be replaced by zero. The value below which the w_j are set to zero (the *tolerance level* or *precision*) is arbitrary and can be chosen for a specific problem.

It was decided to replace the matrix inversions in the Scatter code with pseudoinverses as was done with the version written in Mathematica. It had been demonstrated (I. McAuley, private communication) that using the pseudoinverse with a suitable tolerance level solved the issue with the Planck beams being wider than predicted at very specific frequencies.

3.4.1 Calculating the Pseudoinverse of a Matrix in C

The optimised and robust algorithm, given in Press et al. [37] was used to compute the SVD, the routine

```
void svdcmp(float **a, int m, int n, float w[], float **v)
```

computes the SVD of a *real* matrix **a** ($\mathbf{UWV}^T$) and replaces **a** with **U** on output. The vector w contains the singular values of **W** and the matrix **V** is also available. Because Scatter needs the inverse of *complex* matrices, either this routine would have to be re-written using complex arithmetic, or else the problem would have to be re-cast in terms of real matrices. The decision was made to test the latter option in the first instance.

Say we want to solve the following system of equations

$$(\mathbf{Ar} + i\mathbf{Ai}).(\mathbf{x} + i\mathbf{y}) = (\mathbf{b} + i\mathbf{d}) \qquad \textbf{(3.12)}$$

where $\mathbf{Ar} + i\mathbf{Ai}$ is an $n \times n$ complex matrix and $\mathbf{x} + i\mathbf{y}$ and $\mathbf{b} + i\mathbf{d}$ are n-element complex vectors, we can solve for $\mathbf{x} + i\mathbf{y}$ by inverting the complex matrix $\mathbf{Ar} + i\mathbf{Ai}$

$$(\mathbf{x} + i\mathbf{y}) = (\mathbf{Ar} + i\mathbf{Ai})^{-1}(\mathbf{b} + i\mathbf{d})\,. \qquad \textbf{(3.13)}$$

Alternatively, we can multiply the terms in brackets and take the real and imaginary parts to give

$$\mathbf{Ar}.\mathbf{x} - \mathbf{Ai}.\mathbf{y} = \mathbf{b} \tag{3.14}$$

$$\mathbf{Ai}.\mathbf{x} + \mathbf{Ar}.\mathbf{y} = \mathbf{d} \tag{3.15}$$

which can be re-written as a set of $2n \times 2n$ equations

$$\begin{pmatrix} \mathbf{Ar} & -\mathbf{Ai} \\ \mathbf{Ai} & \mathbf{Ar} \end{pmatrix} . \begin{pmatrix} \mathbf{x} \\ \mathbf{y} \end{pmatrix} = \begin{pmatrix} \mathbf{b} \\ \mathbf{d} \end{pmatrix} . \tag{3.16}$$

To solve this equivalent set of equations we need to invert a $2n \times 2n$ real matrix. When the inverse of this matrix is found, the real and imaginary components of the inverse of the original complex matrix can be found from subsections of the $2n \times 2n$ real matrix:

$$\begin{pmatrix} [\text{real}] & -[\text{imaginary}] \\ [\text{imaginary}] & [\text{real}] \end{pmatrix} .$$

So our method for finding the pseudoinverse of a complex matrix **A** becomes:

1. Construct real matrices **Ar** and **Ai** from the real and imaginary components of **A**
2. Construct the real matrix **NewA=** $\begin{pmatrix} \mathbf{Ar} & -\mathbf{Ai} \\ \mathbf{Ai} & \mathbf{Ar} \end{pmatrix}$
3. Use the routine `svdcmp()` to perform the singular value decomposition of this real matrix to give $\mathbf{U}, \mathbf{W},$ and $\mathbf{V}$.
4. If any of the elements of **W** are < a user-defined tolerance value then replace them by 0, otherwise invert them to give $\bar{\mathbf{W}}^{-\mathbf{1}}$
5. Construct the pseudoinverse of the real matrix in step 2 from $\mathbf{V}\bar{\mathbf{W}}^{-\mathbf{1}}\mathbf{U}^{T}$.
6. Find the pseudoinverse of the complex matrix by taking real and imaginary components from two quadrants of the matrix in 5.

The algorithm is illustrated with the following example.

We want to find the inverse of the 3×3 complex matrix:

$$\mathbf{A} = \begin{bmatrix} 1 & 0 & -1-i \\ 0 & 2+5i & 0 \\ 0 & 0 & i \end{bmatrix}. \tag{3.17}$$

We construct matrices from the real and imaginary components (step 1)

$$\mathbf{Ar} = \begin{bmatrix} 1 & 0 & -1 \\ 0 & 2 & 0 \\ 0 & 0 & 0 \end{bmatrix}, \tag{3.18}$$

$$\mathbf{Ai} = \begin{bmatrix} 0 & 0 & -1 \\ 0 & 5 & 0 \\ 0 & 0 & 1 \end{bmatrix}, \tag{3.19}$$

and make a 6×6 matrix (step 2)

$$\mathbf{NewA} = \begin{bmatrix} 1 & 0 & -1 & 0 & 0 & -1 \\ 0 & 2 & 0 & 0 & 5 & 0 \\ 0 & 0 & 0 & 0 & 0 & 1 \\ 0 & 0 & -1 & 1 & 0 & -1 \\ 0 & 5 & 0 & 0 & 2 & 0 \\ 0 & 0 & 1 & 0 & 0 & 0 \end{bmatrix}. \tag{3.20}$$

We find the singular value decomposition of this matrix (step 3) which gives

$$\mathbf{U} = \begin{bmatrix} 0 & 0 & 0 & -0.888074 & 0.459701 & 0 \\ -1 & 0 & 0 & 0 & 0 & 0 \\ 0 & 0 & 0.325058 & 0.325058 & 0.627963 & -0.627963 \\ 0 & 0 & 0.888074 & 0 & 0 & 0.459701 \\ 0 & -1 & 0 & 0 & 0 & 0 \\ 0 & 0 & -0.325058 & 0 & 0.627963 & 0.627963 \end{bmatrix}$$

$$\mathbf{W} = \begin{bmatrix} 5.38516 & 0 & 0 & 0 & 0 & 0 \\ 0 & 5.38516 & 0 & 0 & 0 & 0 \\ 0 & 0 & 1.93185 & 0 & 0 & 0 \\ 0 & 0 & 0 & 1.93185 & 0 & 0 \\ 0 & 0 & 0 & 0 & 0.517638 & 0 \\ 0 & 0 & 0 & 0 & 0 & 0.517638 \end{bmatrix}$$

and

$$\mathbf{V} = \begin{bmatrix} 0 & 0 & 0 & -0.459701 & 0.888074 & 0 \\ -0.371391 & -0.928477 & 0 & 0 & 0 & 0 \\ 0 & 0 & -0.627963 & 0.627963 & 0.325058 & 0.325058 \\ 0 & 0 & 0.459701 & 0 & 0 & 0.888074 \\ 0.928477 & -0.371391 & 0 & 0 & 0 & 0 \\ 0 & 0 & -0.627963 & -0.627963 & -0.325058 & 0.325058 \end{bmatrix}$$

We invert the w_j to give $\bar{\mathbf{W}}^{-1}$ (step 4, in this case we apply no tolerance level)

$$\mathbf{W} = \begin{bmatrix} 0.185695 & 0 & 0 & 0 & 0 & 0 \\ 0 & 0.185695 & 0 & 0 & 0 & 0 \\ 0 & 0 & 0.517638 & 0 & 0 & 0 \\ 0 & 0 & 0 & 0.517638 & 0 & 0 \\ 0 & 0 & 0 & 0 & 1.93185 & 0 \\ 0 & 0 & 0 & 0 & 0 & 1.93185 \end{bmatrix}$$

and find the pseudoinverse from $\mathbf{V}\bar{\mathbf{W}}^{-1}\mathbf{U}^T$ (step 5)

$$\begin{bmatrix} 1 & 0 & 1 & 0 & 0 & 1 \\ 0 & 0.0689655 & 0 & 0 & 0.172414 & 0 \\ 0 & 0 & 0 & 0 & 0 & 1 \\ 0 & 0 & -1 & 1 & 0 & 1 \\ 0 & -0.172414 & 0 & 0 & 0.0689655 & 0 \\ 0 & 0 & -1 & 0 & 0 & 0 \end{bmatrix}.$$

We then use 3×3 sub-matrices of this to construct the (complex) inverse of the complex matrix **A**:

$$\mathbf{A} = \begin{bmatrix} 1 & 0 & 1-i \\ 0 & 0.0689655 - 0.172414i & 0 \\ 0 & 0 & -i \end{bmatrix}.$$

This technique has the advantage of making use of an existing optimised routine; however, it is a factor of 2 more inefficient in both storage and computation time, and so in the longer-term it would be better to re-write the SVD routine for complex matrices.

A technique, suggested by other authors, to improve the efficiency of the real SVD technique [38] involves calculating the real components of the inverse from

$$\mathbf{Real} = [\mathbf{Ar} + \mathbf{Ai} \,.\, \mathbf{Ar}^{-1} .\, \mathbf{Ai}]^{-1}$$

and the imaginary from

$$\mathbf{Imag} = -\mathbf{Real} \,.\, \mathbf{Ai} \,.\, \mathbf{Ar}^{-1}$$

or from a set of similar equations if **Ar** is singular; however, this approach would not work if both **Ar** and **Ai** are singular, as is the case for the example given above.

The function `svdcmp()` in [37] was adapted as follows (additions in blue). First complex numbers were defined using structures (double precision), and the tolerance level set using PSEUDOPRECISION

```
#define PSEUDOPRECISION 0.01
typedef struct DCOMPLEX {double r,i;} dcomplex;
//define a structure for complex nos. real & imaginary part

dcomplex **dCinvsvdcmp(dcomplex **ca, int m, int n)
{
 dcomplex **cainv;          // this will be the inverse of the input complex matrix ca
 int flag,i,its,j,jj,k,l,nm;
 double anorm,c,f,g,h,s,scale,x,y,z,*rv1;
 double **a, **v, **wm, **ut;
 double *w;

 a=dmatrix(1,2*m,1,2*n); // the function dmatrix initialised a matrix of doubles
 v=dmatrix(1,2*m,1,2*n); // these matrices are twice size of the input matrix
 wm=dmatrix(1,2*m,1,2*n);
 w=dvector(1,2*m);
 ut=dmatrix(1,2*m,1,2*n);
 cainv=dCmatrix(1,m,1,n);   // the function dCmatrix initialises a complex matrix

 for(i=1;i<=2*m;i++){
                            // make 2m * 2m matrix from real and imag coeffs
             for(j=1;j<=2*n;j++){
                    // if A is matrix of real C is matrix of imag then make large
                    if (i<=m && j<=n) a[i][j]=(double)ca[i][j].r;
                            // matrix as {{A -C},{C A}} See Num Rec p.49
             else if (i>m && j>n)a[i][j]=(double)ca[i-m][j-n].r;
             else if (i>m && j<=n) a[i][j]=(double)ca[i-m][j].i;
                    else a[i][j]=(double)-ca[i][j-n].i;
  }
 }
```

```
  m*=2;
  n*=2; // matrix of real nos. is of size2m*2n

 rv1=dvector(1,n);          // this begins SVD (real) from Numerical Recipes
        .
        .
        .
 free_dvector(rv1,1,n);
                                  // this ends SVD (real) from Numerical Recipes

// now we reconsruct the pseudoinverse
// make 2D matrix from the inverse of singular values
 wm=dinvsingval(w,1,m,1,n);
// dsingval() constructs a matrix from the inverse of the values of a vector

// make U transpose
 ut=dtranspose(a,1,m,1,n); // dtranspose() transposes a matrix
// now we reconsruct the pseudoinverse from V 1/w Ut
 a= dmulm(v, m, n, dmulm(wm, m, n, ut, m,n), m,n);
                  // dmulm() multiplies 2 matrices
// now take sections sub-sections of this large matrix to make real and imaginary
components
 for(i=1;i<=m/2;i++){
        for(j=1;j<=n/2;j++){
        cainv[i][j].r=(double)a[i][j]; // see numerical recipes p49-50
              cainv[i][j].i=(double)a[i+m/2][j];
        }
  }
        // free memory
 free_dvector(w,1,n);
 return cainv;
}
```

The routine above makes use of the following functions

```
double **dmulm(double **m, int r1, int c1, double **n, int r2, int
c2)
{
 int i,j,k;
 double **mn;
 double czero;
```

```
 if (c1!=r2) nrerror("matrix size error in multiplication");
 czero=0.0;
 mn= dmatrix(1,r1,1,c2);

 for(i=1;i<r1+1;i++){
       for(j=1;j<c2+1;j++) {
                   mn[i][j]=czero;
                   for(k=1;k<c1+1;k++)
                         mn[i][j]= mn[i][j]+m[i][k]*n[k][j];
             }
 }
 return mn;
}
double **dtranspose(double**m, long nrl, long nrh, long ncl, long
nch)
{
 double **mt;
 int i,j;

 mt=dmatrix(1,nch-ncl+1,1,nrh-nrl+1); //swap row and col dimensions
       for (i=nrl;i<nrh+1;i++)  {
       for (j=ncl;j<nch+1;j++)
             mt[j][i]=m[i][j];
       }
 return mt;
}



double **dinvsingval(double*v, long nrl, long nrh, long ncl, long
nch)
{
 double **mt;
 int i,j;

 mt=dmatrix(1,nrh-nrl+1,1,nch-ncl+1);
       for (i=nrl;i<nrh+1;i++)  {
             for (j=ncl;j<nch+1;j++)
if (i==j && v[i]>PSEUDOPRECISION) mt[j][i]=1/v[i];          // invert
diagonal values so long as they are not too small
             else mt[j][i] =0.0;
       }
```

```
 return mt;
}
```

3.5 Examples Utilizing the Pseudoinverse Code

The pseudoinverse was implemented in the Scatter code in situations where there was believed to be numerical instability. The first case, Planck, follows the work carried out by Ian McAuley of NUI Maynooth in the Mathematica version of the Scatter code.

3.5.1 The 857-GHz Planck Horn

The Planck telescope will be described in more detail in Chapter 5. The beam pattern of the front-end 857-GHz Planck horn (Figure 3.2) was calculated across 30% of its full bandwidth. The horn had been designed to give a uniform beam pattern across the band, and this was found to be the case, with the exception of a small number of frequency intervals where the beam suddenly got wider than expected. This behaviour was unphysical, and so the original C code was modified to use the pseudoinverse when inverting matrices, as described in the previous section. Figure 3.3 shows results from the C-code. For example, the beam at 840 GHz was originally found to be substantially wider than at 830 GHz. The pseudoinverse was implemented and the tolerance level (`PSEUDOPRECISION` in the code listed above) incrementally reduced. It was found that below a certain level, the 840-GHz beam produced was narrower and similar to the pattern at other frequencies. This would be a difficult process to automate, as the tolerance level required had to be found by trial-and-error, but at least this technique could be used to flag if singular values were especially small and likely to lead to errors. The situations when this occurred could then be further studied.

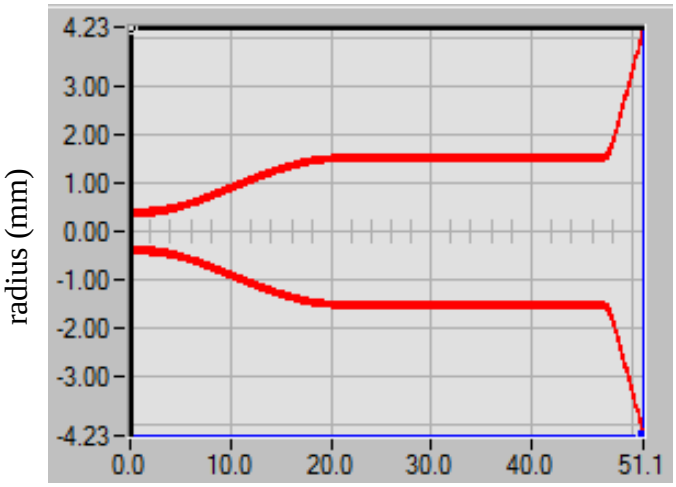

Figure 3.2 Profile of the Planck 857-GHz horn

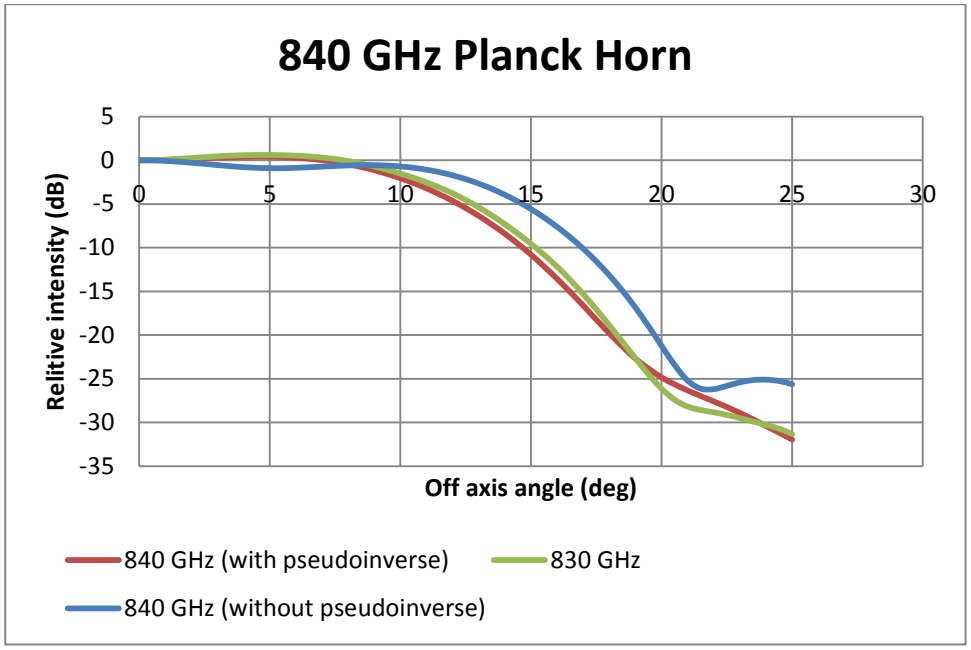

Figure 3.3 Plot of the far-field beam of the Planck 857-GHz horn. The beam patterns were calculated using Scatter at 830 and 840 GHz. The 840-GHz beam pattern was calculated with and without the pseudoinverse implemented. (40 TE/TM modes were used)

3.5.2 Small Gaps in Platelet Horns

The pseudoinverse was also used when investigating issues with platelet horns, discussed in Chapter 4. Specifically I wanted to find out whether small gaps between corrugations in horns designed for the QUBIC experiment would impact on beam quality. If the gaps were very small then CST could not be used as there was a practical limit to how finely the structure could be sampled ($\lambda/12$).

Scatter was found to produce unphysical results when small gaps were introduced and it was decided to investigate whether this was also due to problems with matrix inversion. Figure 3.4 shows results for adding a small gap of 0.003 mm (λ/666.6) between the corrugations with and without the pseudoinverse. The results show that the inverse matrix routine is stable and produces reasonable results when dealing with an unaltered 150 GHz QUBIC horn. However, when a small gap of λ/666.6 is introduced, the beam pattern produced by the inverse matrix routine has no distinct sidelobes. The pseudoinverse produces reasonable and expected results.

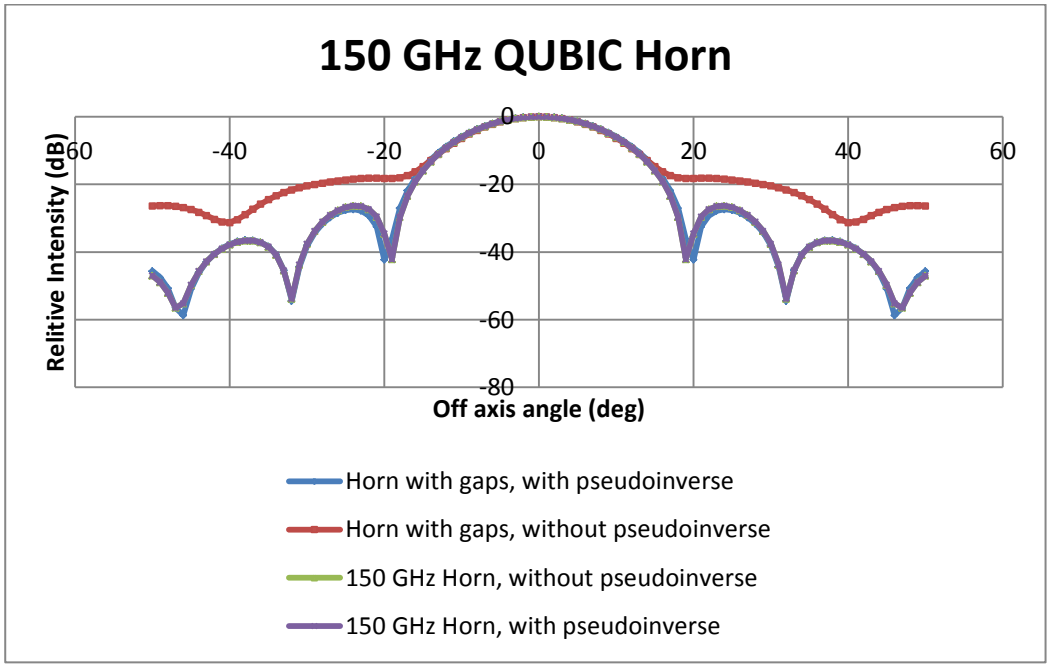

Figure 3.4 Plot of the far-field beam of the QUBIC 150-GHz horn. The beam patterns were calculated using Scatter with a gaps between the corrugations. The beam pattern was calculated with and without the pseudoinverse implemented. (60 TE/TM modes were used)

3.6 Summary

In this chapter I have described the modifications made to the mode-matching software Scatter. This software is used in many of the simulations throughout this thesis, making the accuracy and stability of this software vital.

When Scatter was used to predict the beam pattern of the 840-GHz Planck horn, it produced some unexpected results, such as a wider beam pattern and higher sidelobes. Ian McAuley discovered that the instability of the inverse matrix routine was the cause of these unusual results. To solve for this instability the pseudoinverse was introduced as a substitute for the inverse matrix. The pseudoinverse was integrated into the Scatter code for MatLab and Mathematica environments by Ian McAuley. This chapter describes the method for integrating the pseudoinverse matrix routine in the C (NI LabWindows) environment. I applied the new code to two examples: the Planck horn and also the platelet horns with small gaps (studied in Chapter 4). I found that using the pseudoinverse for the inverse of the matrix improved the operation of the Scatter code in both cases.

Chapter 4 Analysis of Platelet Horn Arrays for QUBIC

4.1 Introduction

This chapter investigates issues associated with the use of platelet horn arrays in an experiment called QUBIC, a bolometric interferometer designed to measure the CMB B-mode polarization anisotropies. These B-modes have yet to be discovered and are believed to have been created by gravitational waves during the inflationary stage of the big bang. The experiment makes use of a new technique known as ‘bolometric interferometry', which combines the sensitivity of bolometers and the systematic effect control of interferometry. After outlining the design of QUBIC, this chapter will discuss the results from the analysis of the platelet horn arrays that will be used.

4.2 QUBIC

As discussed in Chapter 1, to avoid absorption due to water vapour, THz experiments need to be either in space, airborne or located in a high dry areas on the ground. Therefore, the QUBIC experiment will be located in Dome C in Antarctica (Figure 4.1). The measurement of B-modes will be very difficult as they are predicted to have an amplitude of less than 0.1 μK but it is believed that measuring these B-modes is possible using 10^3 detectors working for 1 year [16]. QUBIC will take measurements at 97, 150 and 220 GHz using 144, 400 and 625 receiver horns respectively.

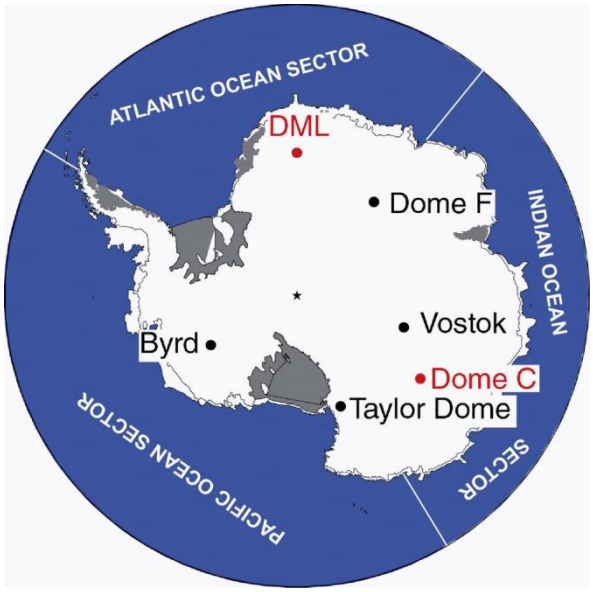

Figure 4.1 The location of Dome C in Antarctica (i.e. the location of QUBIC).[39]

The difficulty we encounter when trying to detect B-modes is reducing the background noise, due to for example polarized emission from Galactic dust and synchrotron radiation. However, from previous CMB experiments the removal of background noise is believed to be possible. Another challenge is the control or removal of systematic errors. Some systematic errors can cause saturation of the weak B signal by the stronger E modes or temperature anisotropy. It has been shown in past experiments that interferometry is a good technique for reducing systematic errors. Interferometers can use pure optics, resulting in low sidelobe levels, and are insensitive to time varying systematics. QUBIC will not only measure the B-mode linear polarization but can also measure circular polarization which can in turn provide a test of the standard model.

4.2.1 Instrumental Set Up

The QUBIC instrument is similar to a Fizeau interferometer. It uses an array of back-to-back horns, located at the aperture of a cryostat, to act as diffractive pupils. The electromagnetic radiation coming from the sky experiences phase differences due to the separation between the input horns. The back horns re-emit

the radiation keeping this phase difference inside the cryostat. The interference pattern due to radiation coming from all the horns is then formed on the focal plane of an optical beam combiner. A half-wave plate located after the re-emitting horns modulates the polarization of the field (Figure 4.2). A polarization grid separates the polarization onto two bolometric arrays (30×30) each measuring a linear combination of the Stokes parameters. The detector arrays will consist of a grid of TES bolometers (approx. one wavelength in width), most likely a bare array but QUBIC may make use of horns to couple the radiation from the telescope. Platelet technology, described next, will be used to manufacture the array of back-to-back sky (primary) horns and it is also a promising technique for coupling to large focal plane arrays.

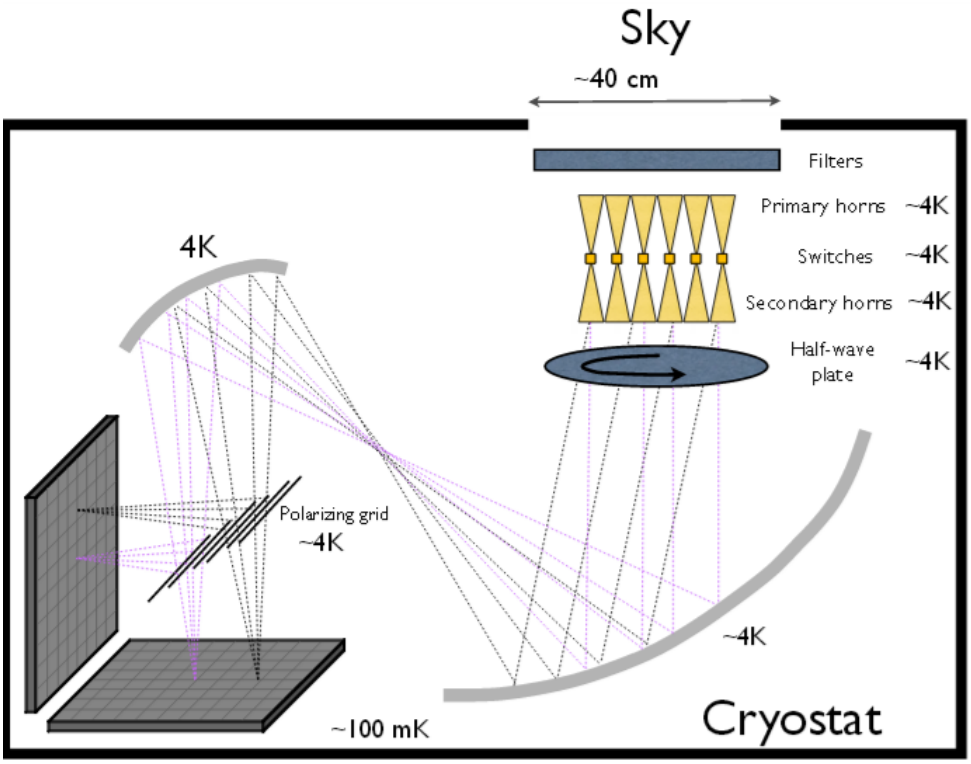

Figure 4.2 A schematic of a QUBIC module. [16]

The first QUBIC module is planned to be installed in 2014 at the Franco-Italian Concordia station in Dome C. It will comprise of 400 sky horns operating

at 150 GHz. When complete, the entire QUBIC instrument will consist of three modules operating at 95, 150 and 220 GHz.

4.3 Platelet Formed horns

One method of producing corrugated feed horns is to use platelet horn arrays which are fabricated using platelet technology. This process involves taking thin sheets of metal (platelets) and cutting a pattern of holes into the platelet. Figure 4.3 shows the process by which the corrugated horns are made.

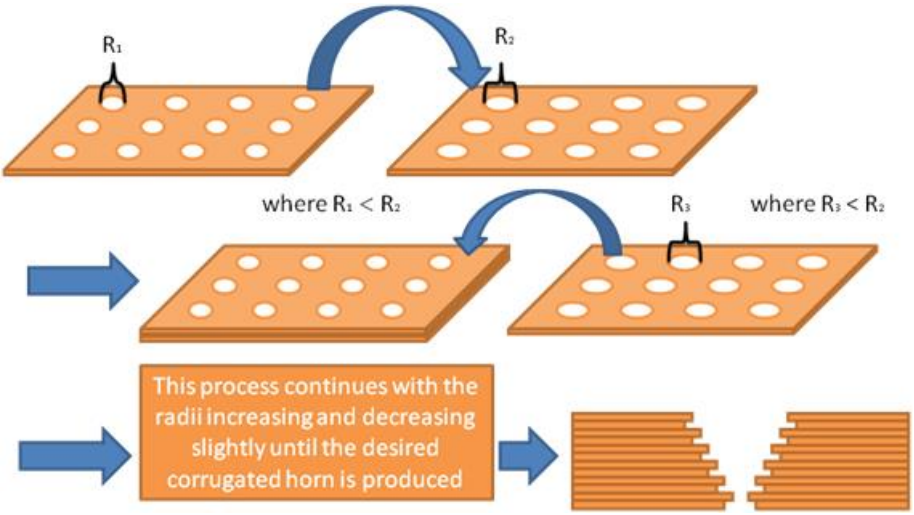

Figure 4.3 The platelet horn process.

There have been a number of different techniques that have been used to fabricate these platelet arrays. The difference between these techniques lies in the different materials used, different material removal methods and different methods for bonding the plates. Diffusion-bonded [40] platelet feed horn arrays were first fabricated by Haas et al [41] for remote sensing. Their first horn array of 9 elements used zirconium copper with the hole patterns chemically etched. In an earlier version they used dip brazing to connect the platelets into a single corrugated feed horn assembly. Recently a 1020-element platelet array for submillimeter work using etched copper platelets was developed [42].

4.3.1 Advantages and Disadvantages of Platelet Feed Horn Arrays

Advantages

Platelet arrays use a well-established machining and fabrication process for which metallic structures are compatible with reliable cryogenic end use. They also represent a step toward building a large number of detector elements in a focal plane. The theoretical predictions of platelet array performance are very mature.

Disadvantages

These arrays have a relatively high metal mass/volume meaning that they would be unsuitable for a space-born project. The detector coupling structures are waveguide based. As a result, the packaging requirement can be more demanding than planar array based approaches.

4.3.2 Adding a Thick Plate for Stability

When plates with a large number of holes are added together, the array can become unstable, i.e. it can start to bend and deform. This can affect the performance of the array. To solve this problem one of the solutions considered in the QUBIC project was to add a thick plate on top of the array for stability. Two scenarios were simulated. The first scenario tested the effects of adding a thick plate without any corrugations etched into it (Figure 4.4(a)) and the second scenario tested the a thick plate with corrugations (Figure 4.4(b)), which is significantly more challenging to manufacture. Adding a thick plate is also of interest when designing filters to place in front of the horns. These scenarios were tested using the CST and Scatter software.

(a) (b)

Figure 4.4 Corrugated Platelet horns with one solid thick plate. (a) Smooth walled thick plate, (b) corrugated thick plate.

The sky facing horns used in QUBIC are scaled versions of horns designed for the ClOVER [43] experiment which are optimised to give beams with very high gaussianity. These simulations used a similar horn design to a horn we have available here in NUI Maynooth and so we were able to compare the designs experimentally. To simulate adding a thick plate, the horn's geometry file was altered. Extra corrugations were added, using Mathematica, to the end of the geometry file to simulate a corrugated thick block (Figure 4.5) and one long corrugation was added to simulate a smooth thick plate (Figure 4.6). The geometry file could then be used as input to CST and Scatter.

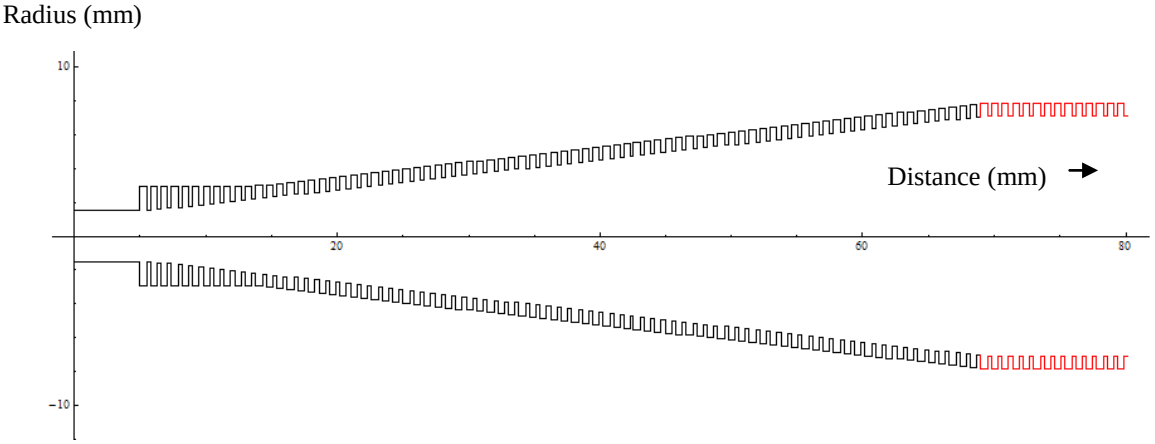

Figure 4.5 A corrugated horn with extra corrugations added to the end of the horn to simulate a corrugated thick block (highlighted in red).

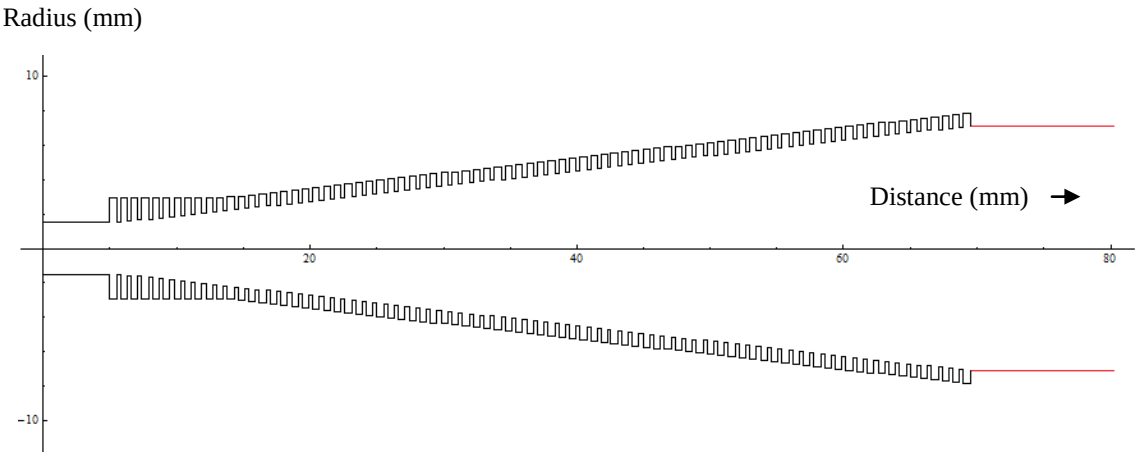

Figure 4.6 A corrugated horn with one long corrugation added to the end of the horn, to simulate a smooth thick block (highlighted in red).

4.3.3 Adding a Thick Plate (simulations with CST)

CST was used to test the effects on the farfield pattern when a smooth plate (Figure 4.7) and a corrugated plate (Figure 4.8) are attached to the end of a corrugated horn.

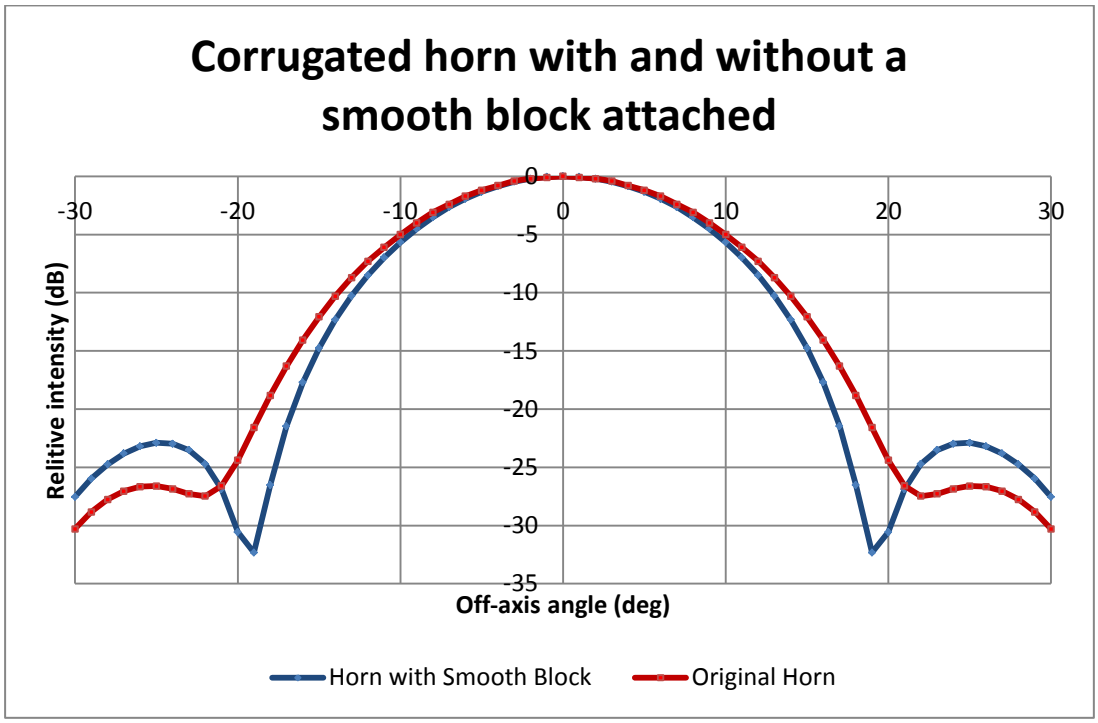

Figure 4.7 Co-polar power (E-cut) as a function of off-axis angle for a corrugated horn with a smooth block attached (see Figure 4.6). (CST simulations)

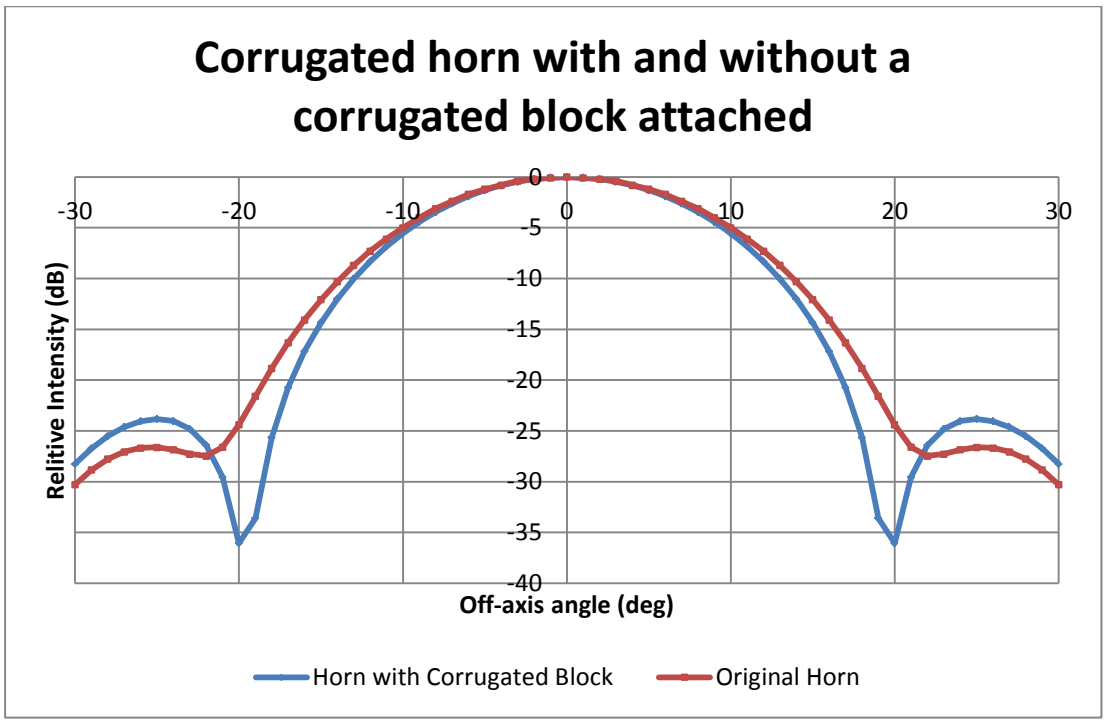

Figure 4.8 Co-polar power (E-cut) as a function of off-axis angle for a corrugated horn with a corrugated block attached (see Figure 4.5). (CST simulations)

The results (Figures 4.7 and 4.8) show in both cases that the beam width has narrowed and the sidelobe levels have increased. When comparing the beam patterns for both scenarios (Figure 4.9) the results show that there is no difference in beam width and only a slightly higher sidelobe level when adding a smooth thick plate as compared with a corrugations plate. This suggests that the effect of the plate must be modelled but that there is almost no advantage to corrugating the plate.

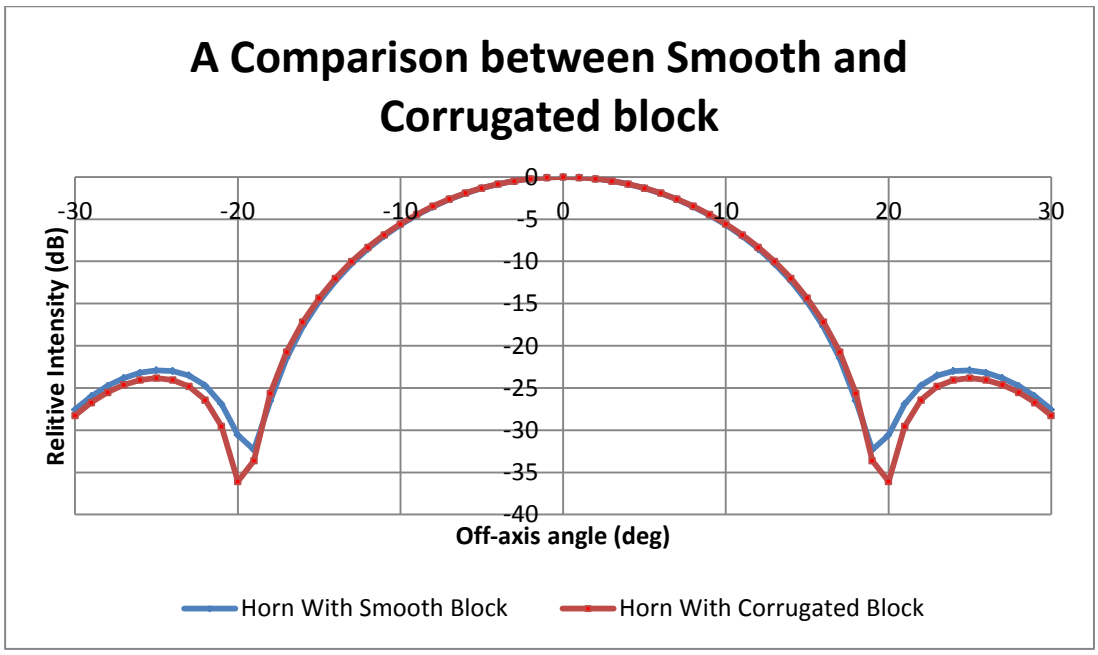

Figure 4.9 A plot comparing the co-polar power as a function of off-axis angle for a horn with a smooth block and a corrugated block. (CST simulations)

4.3.4 Adding a Thick Plate (simulations with CST)

To verify that the results measured by CST were accurate, the effects of adding a thick plate were then investigated using Scatter code and the results were in broad agreement with those obtained using CST.

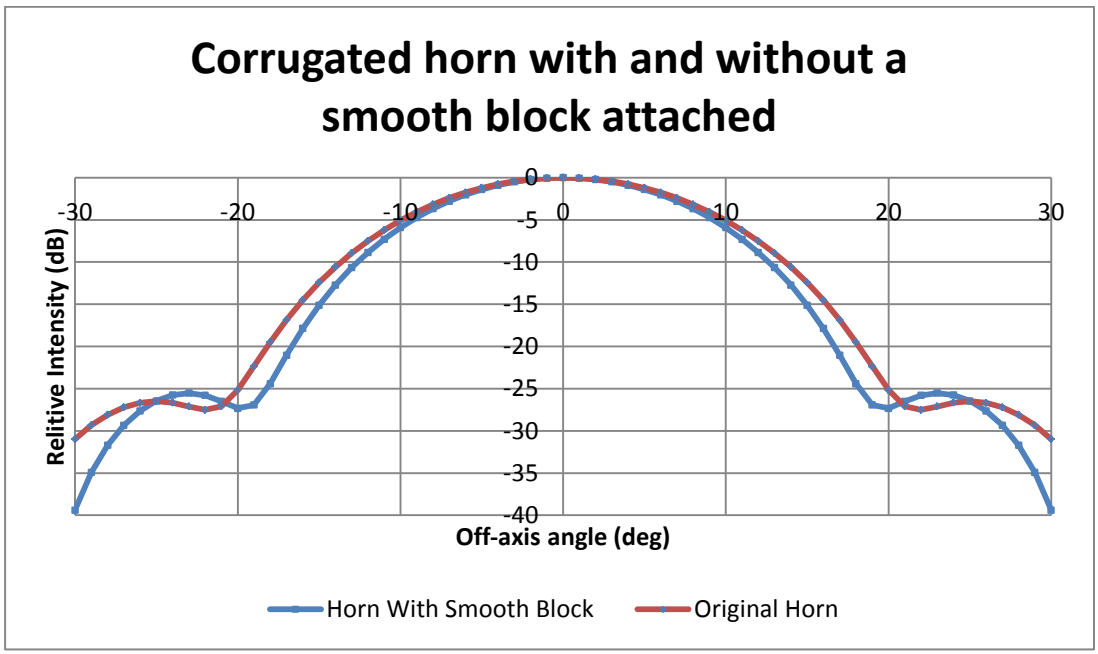

Figure 4.10 Co-polar power as a function of off-axis angle for a corrugated horn with a smooth block attached. (Scatter simulations)

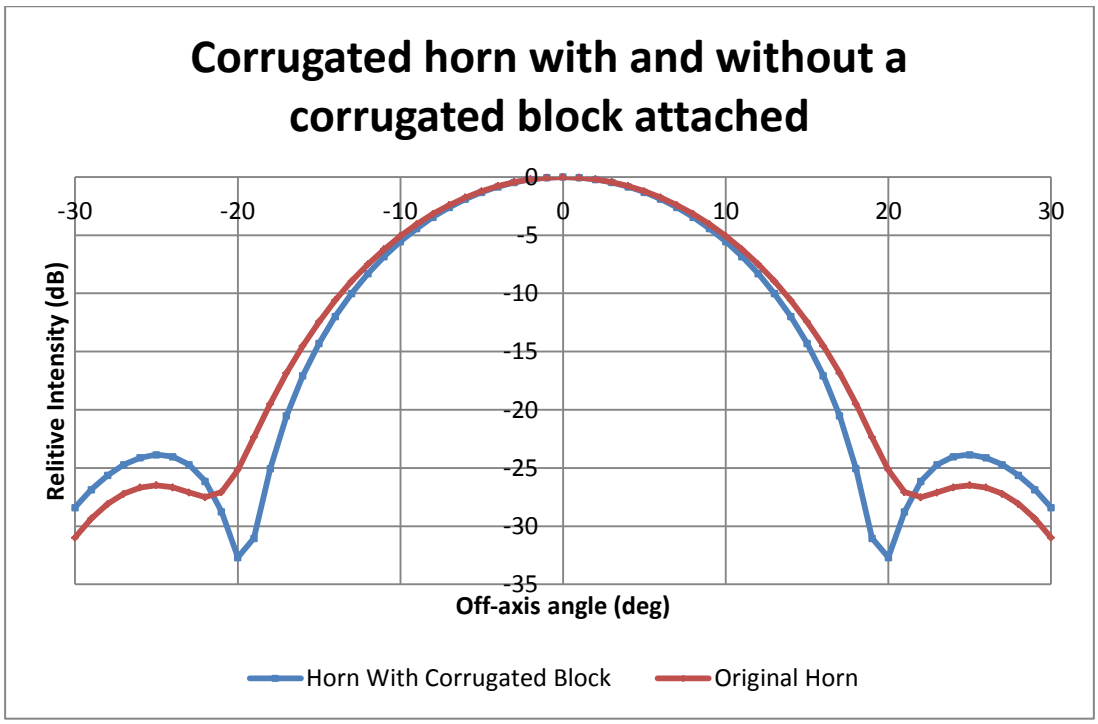

Figure 4.11 Co-polar power as a function of off-axis angle for a corrugated horn with a corrugated block attached. (Scatter simulations)

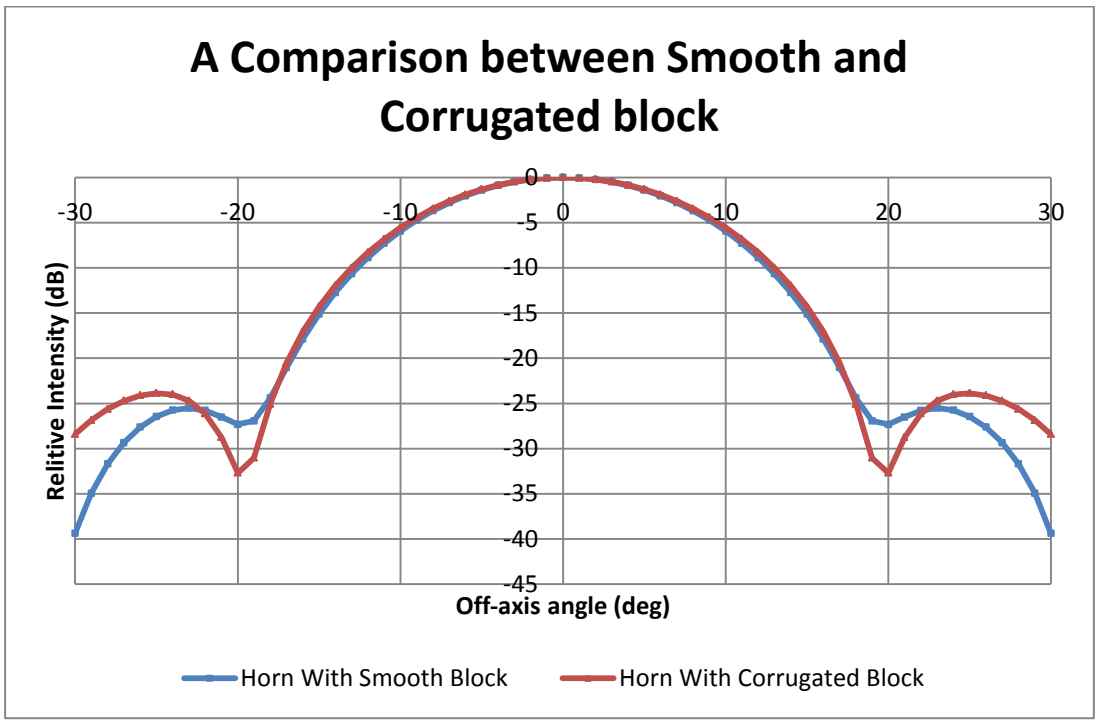

Figure 4.12 A plot comparing the co-polar power as a function of off-axis angle for both a horn with a smooth block and a corrugated block. (Scatter simulations)

The co-polar results (Figures 4.10 and 4.11) for adding a thick smooth and corrugated plate show that the main beam gets more narrow, the sidelobe levels

become slightly higher but are lower than the levels predicted by CST. When comparing the beam patterns, Scatter shows that the horn with a corrugated block attached produces sidelobe levels that are higher than the smooth block (Figure 4.12). The results only differ at the -25 to -35 dB level (about the expected accuracy of the simulations) and we can conclude from both that not corrugating the QUBIC thick plate will have little effect on the sidelobes and none at all on the main beam.

4.3.5 Experimental results

Vector Network Analyser

To experimentally measure the effects of adding a thick plate, a Vector Network Analyser (VNA) was used. The VNA is an instrument that can be used to accurately characterise quasioptical components, as it measures amplitude and phase. The parameters that are commonly measured are reflection and transmission of a test signal or the S-parameters. The VNA is a two port system where a sinusoidal test wave, known as the stimulus, is transmitted through a Device Under Test (DUT) from port 1 and the response is measured by port 2. The response measured at port two will be sinusoidal, but will generally have a different value for both phase and amplitude, an example of this is shown in Figure 4.13. For a two port system the relationship between the reflected waves and the transmitted waves is shown in equation 4.1.

$$\begin{bmatrix} b_1 \\ b_2 \end{bmatrix} = \begin{bmatrix} S_{11} & S_{12} \\ S_{21} & S_{22} \end{bmatrix} \begin{bmatrix} a_1 \\ a_2 \end{bmatrix}. \quad (4.1)$$

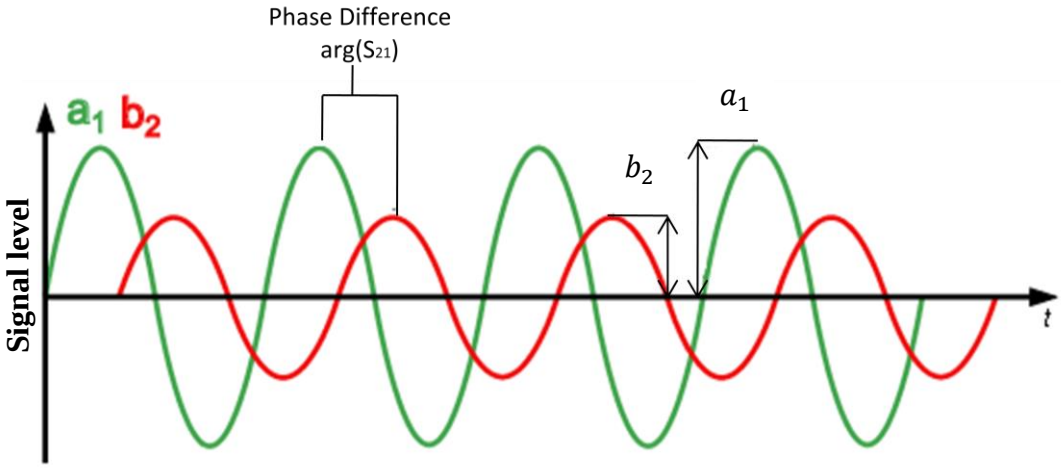

Figure 4.13 An example of the sinusoidal test signal, $\mathbf{a_1}$ is the transmitted wave from port 1 and $\mathbf{b_2}$ is the received signal at port 2. [44].

where S_{11}, S_{21}, S_{12} and S_{22} are the S-parameters and a_1 and b_2 are wave quantities. The system is calibrated before any measurements are made. This is done by the use of DUTs that have known S-parameters. These DUTs along with their characteristic data are provided by commercial companies. The calibration devices along with the in-house system consists of a match (Figure 4.14(a)), a short (Figure 4.14(b)) and an offset (Figure 4.14(c)). A match is made of a cone-shaped structure that acts as an attenuator; a short is a conductive plate that is mounted on the test port with a zero offset and is characterised by 100% return and an offset extends the distance between a short and the waveguide flange.

(a) (b)

(c)

Figure 4.14 The DUTs with known characteristics that are used to calibrate the VNA system: (a) shows the match, (b) the short and (c) the offset.

The DUTs in the case of this research is a corrugated horn with a solid cylinder (Figure 4.15(a)) at the front of the horn, acting as a section of a smooth thick plate, or 13 rings with different radii and thickness (Figure 4.15(b)) attached to the front of the horn, acting as a section of a corrugated plate. The horn attachments were designed by the author. The rings had the same radii and thicknesses as the corrugations of the horn being used. The rings were arranged to mimic the corrugations of the horn. They are held in place in front of the horn by a steel sleeve that could slide over the head of the horn (Figure 4.16(b)). Figure 4.17 shows a schematic drawing of the sleeve and screws that were used to hold the cylinder and rings in place. A 2D CAD drawing showing the dimensions of these components can be found in Appendix A.

(a) (b)

Figure 4.15 (a) A single cylinder, that mimicks the effects of adding a thick plate was placed in front of a corrugated horn. (b) Two examples of the rings used to measure the effects of adding a corrugated block in front of a corrugated horn.

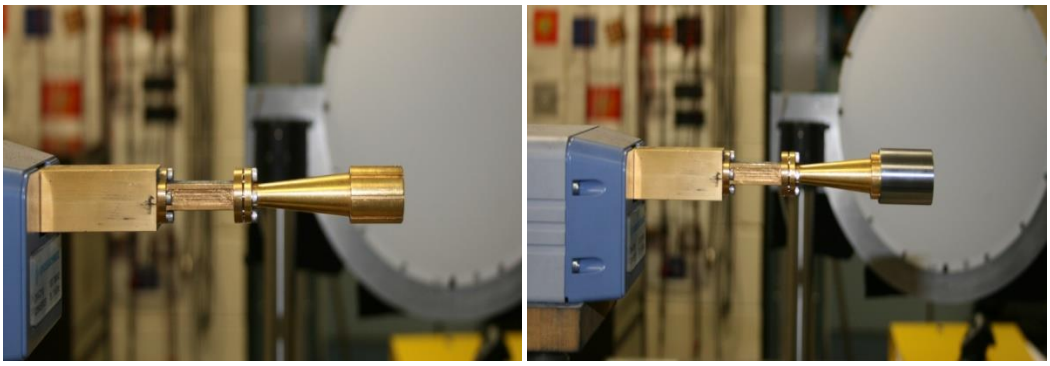

(a) (b)

Figure 4.16 (a) A corrugated horn without any attachments, (b) a corrugated horn with the steel sleeve that contained the cylinder or the rings (see Figure 4.15).

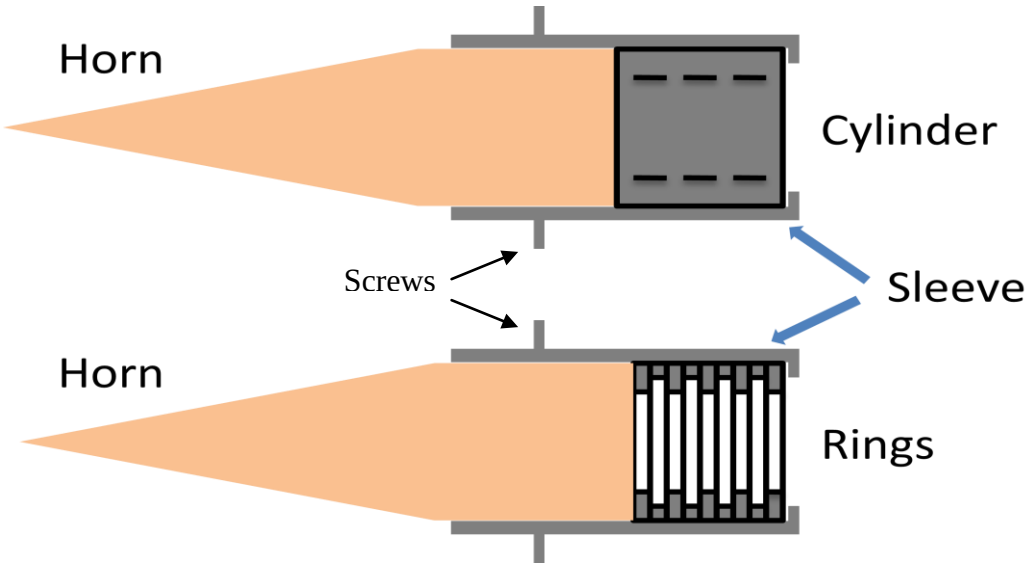

Figure 4.17 A schematic drawing showing how the sleeve was used to hold the cylinder and rings in place.

Since CST can simulate a large number of materials, it was used to determine what material to make these components. There were two materials available in the workshop that could be machined to make these components; these were copper and stainless steel. CST showed that both materials produced the same result and it was decided that stainless steel would be used since it was easier and cheaper to machine.

The distance between the horn and the receiver was adjusted so that the beam out to at least the first sidelobe could be measured by the reciever (which can cover an area of 200 mm^2) (Figure 4.18). It was found that the distance between the receiver and the horn, needed to measure the entire main beam and the first sidelobe (±30°), was approximatly 125 mm. This is ~3 times the confocal distance of the beam, and so sufficiently well into the far-field. At distances greater than this the scanner will not reach as far as the first sidelobe.

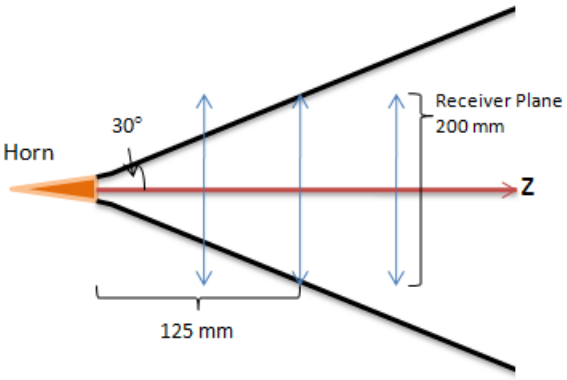

Figure 4.18 Determining the distance between the horn and the receiver to measure the beam pattern out to the first sidelobe (±30º).

The results measured by the VNA (Figure 4.19) show that adding a thick plate, smooth or corrugated, narrows the beam width and slightly increases the levels of the sidelobes, as predicted by CST and Scatter. These results also show that the effects for either a corrugated or a smooth thick plate are almost the same, with only a small difference in the sidelobe levels, again confirming predictions.

When comparing the measured results with the simulated results from CST and Scatter (Figures 4.20 - 4.22) we see reasonable agreement between the results. Figure 4.20 shows a comparison between the measured corrugated horn and the simulated corrugated horn without any attachments, here the agreement is excellent. There is only a difference of approximately 2 dB in the sidelobe level (at -25dB). The results (Figure 4.21) for adding a smooth thick plate show better agreement between Scatter and the measured results than CST which predicted higher and wider sidelobes. The results (Figure 4.22) for adding a corrugated plate show the biggest deviation between measured results and the predicted results. The measured results show a narrower beam and sidelobes. The VNA measurements were taken with a waveguide probe (WR10 waveguide, 2.54 mm x 1.27 mm) at the receiver end and this will have some effect on the measured results, not accounted for here.

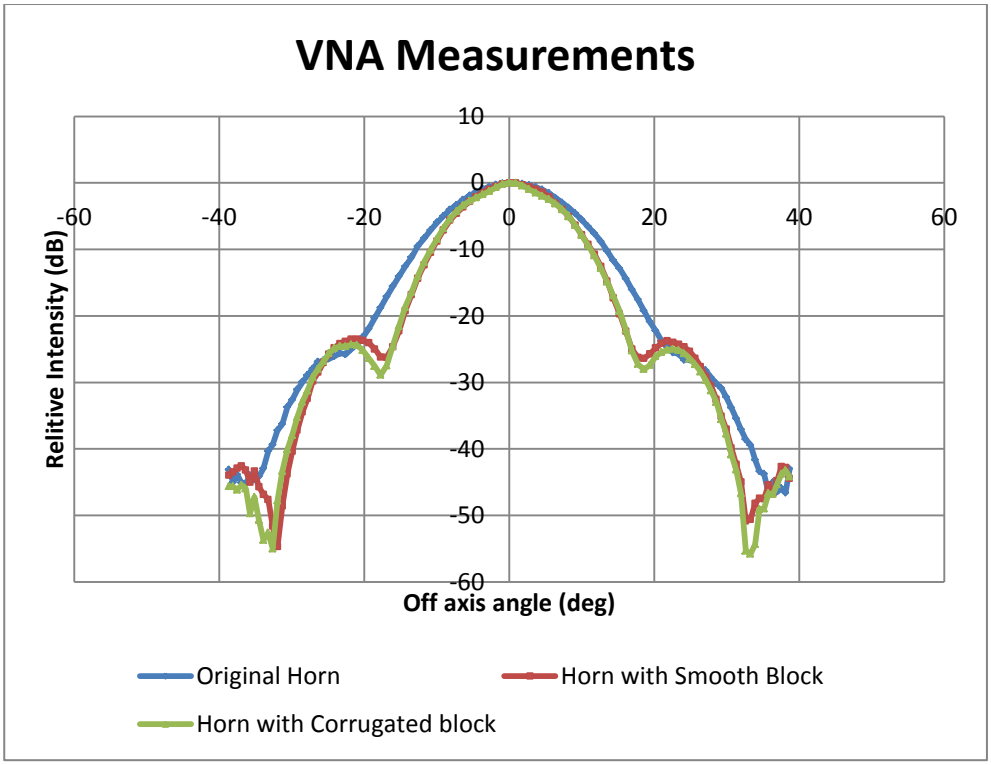

Figure 4.19 The measured co-polar beam pattern of a 100 GHz corrugated without any attachment, with a smooth block attached and with a corrugated block attached. The horn was located 125 mm from the receiver.

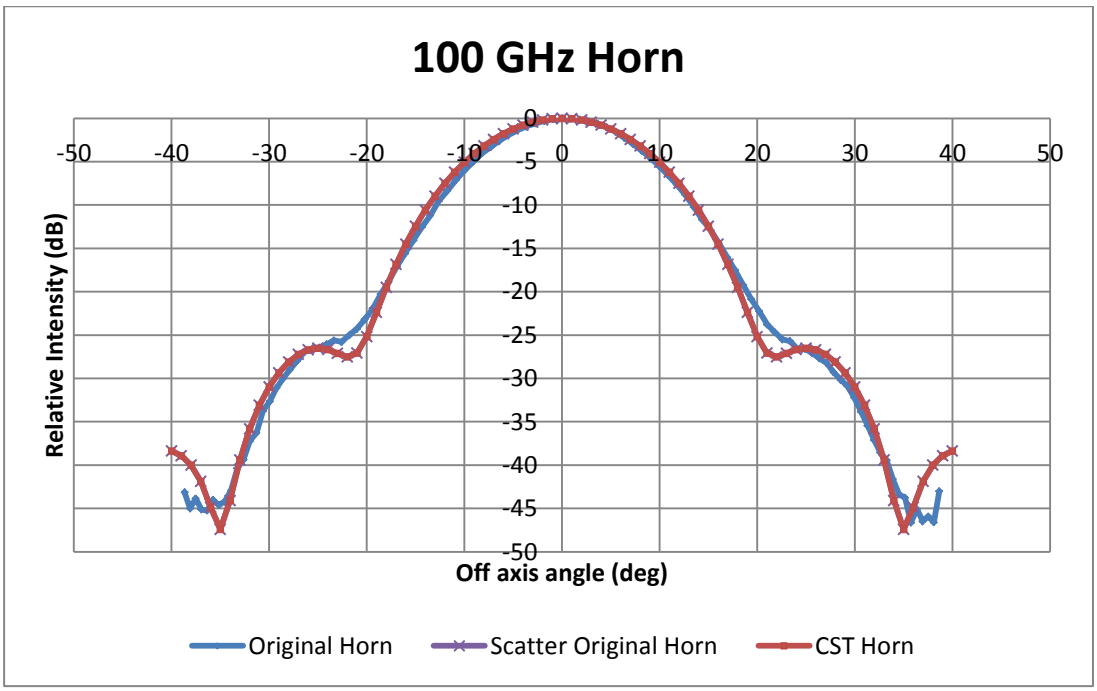

Figure 4.20 The co-polar measured and simulated beam pattern of a 100-GHz corrugated horn without any attachment. The SCATTER and CST traces are identical in this plot

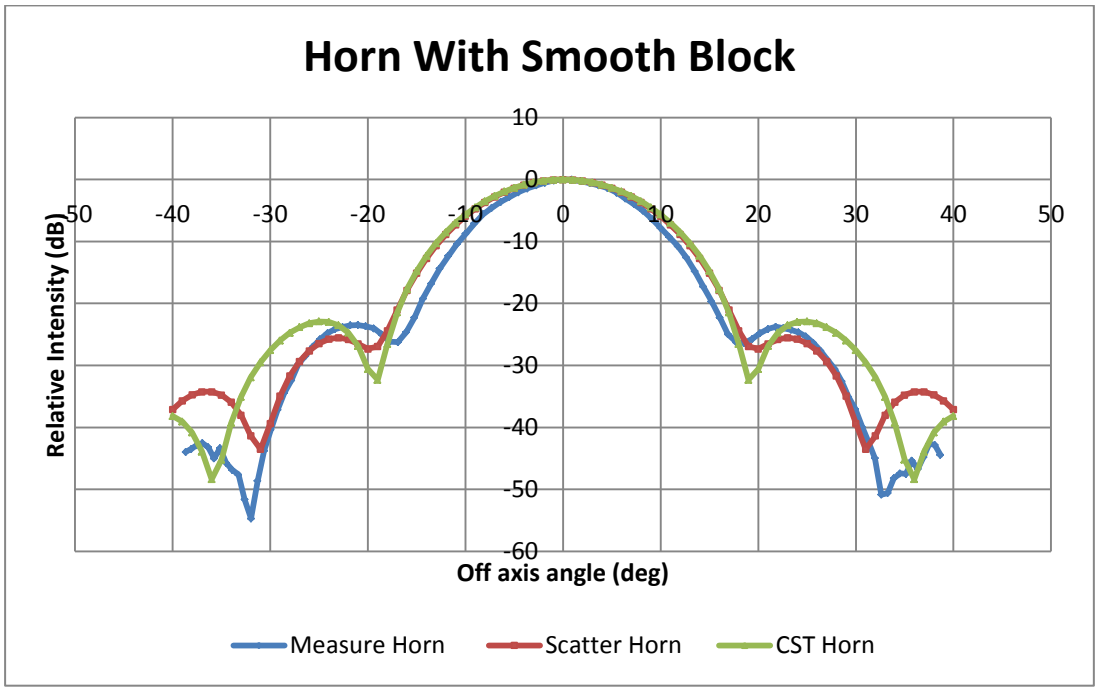

Figure 4.21 The co-polar measured and simulated beam pattern of a 100-GHz corrugated horn with smooth block attached.

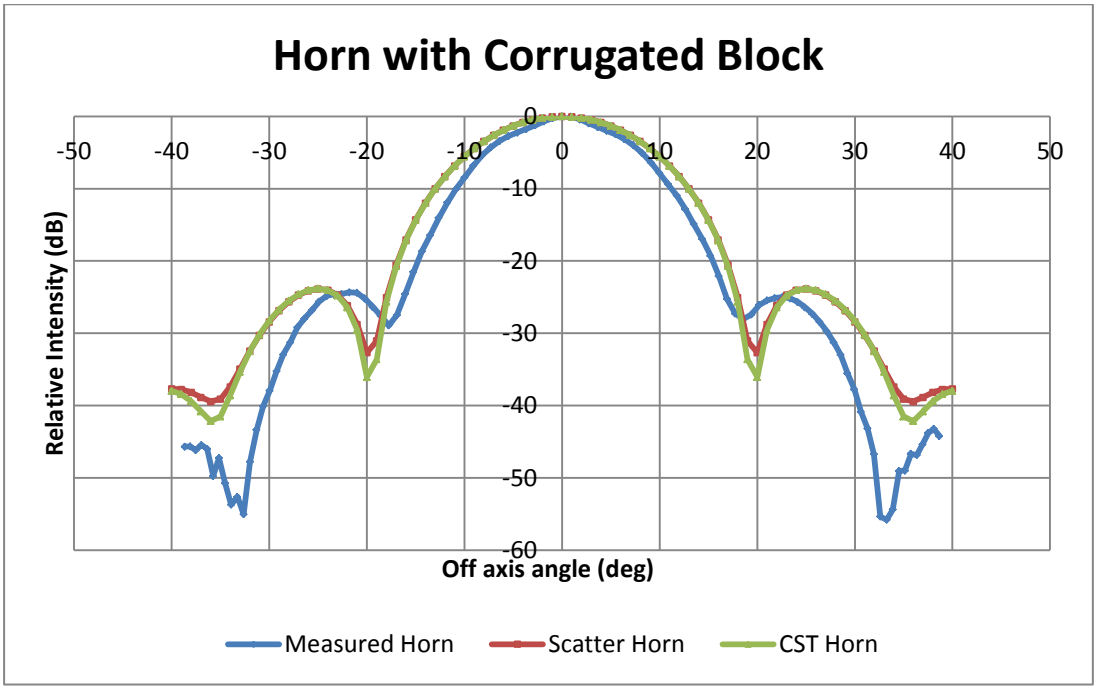

Figure 4.22 The co-polar measured and simulated beam pattern of a 100-GHz corrugated horn with smooth block attached.

The results of adding a block into the front of the horn are summarised in the table below.

Horn Configuration	Method	FWHM (dB)	Sidelobe Level (dB)
100 GHz Horn	Simulation	-13.75878815	-26.6745551
	Measured	-12.33267851	-26.59476262
100 GHz Horn (Smooth Thick Plate)	Simulation	-16.15	-23
	Measured	-13.08867418	-23.81258529
100 GHz Horn (Corrugated Thick Plate)	Simulation	-18.05	-23.8
	Measured	-14.4555772	-25.1264999

Table 4.2 A summary of the effects of adding a thick plate to the front of a horn has on the FWHM and Sidelobe levels

4.3.6 Gaps between platelets

Another concern with using a platelet horn array is the possibility that the plates aren't clamped down tightly enough, creating gaps in between the plates of the horn (Figure 4.21). This section discusses how the size of the gap between the plates affects the beam pattern of a 150-GHz corrugated horn that will be used in the QUBIC telescope. A range of different gap sizes were tested using both CST and the C (NI LabWindows) version of Scatter.

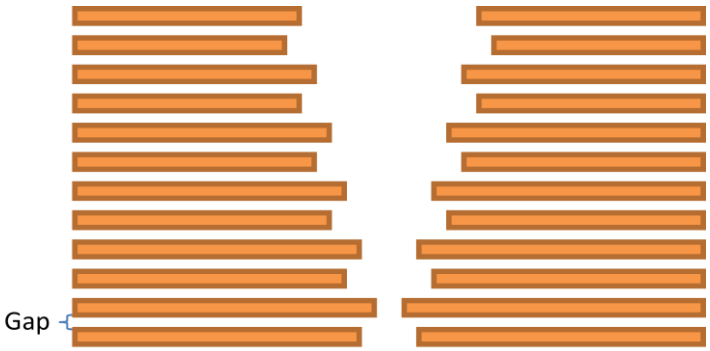

Figure 4.23 Corrugated horn with gaps between the platelets.

Since scatter cannot simulate a 3D model of the horn with gaps like CST can, the program's code needed to be altered. The altered code reads in the horn's geometry file, and from this it creates a new geometry, where every second corrugation had a large radius (to simulate a gap) and a length that can be set to the desired gap size. Figure 4.25 shows the alterations made to the corrugated horn by the program.

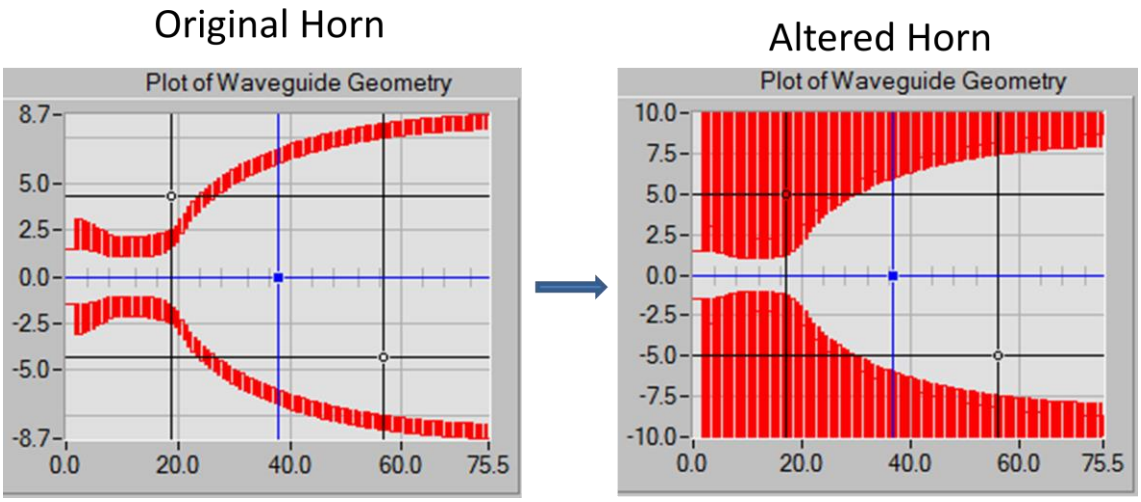

Figure 4.24 (Left) Shows the original horn read from the geometry file. (Right) shows the altered horn where the gap size is set to $\lambda/10^6$.

The results (Figure 4.26) show that an altered horn with a gap size of $\lambda/10^6$ is the same as an unaltered horn with no gap, which was expected as the gap size was very small. The results show that the alterations made to the Scatter software (pseudoinverse, Chapter 3) worked for adding a gap between the corrugations. The effects of having gaps between the corrugations was then measured using this

improved Scatter code. Figure 4.27 shows the co-polar results for a 150-GHz QUBIC horn with gap sizes ranging between 0.003 mm (λ/666) and 0.3mm (λ/6.66).

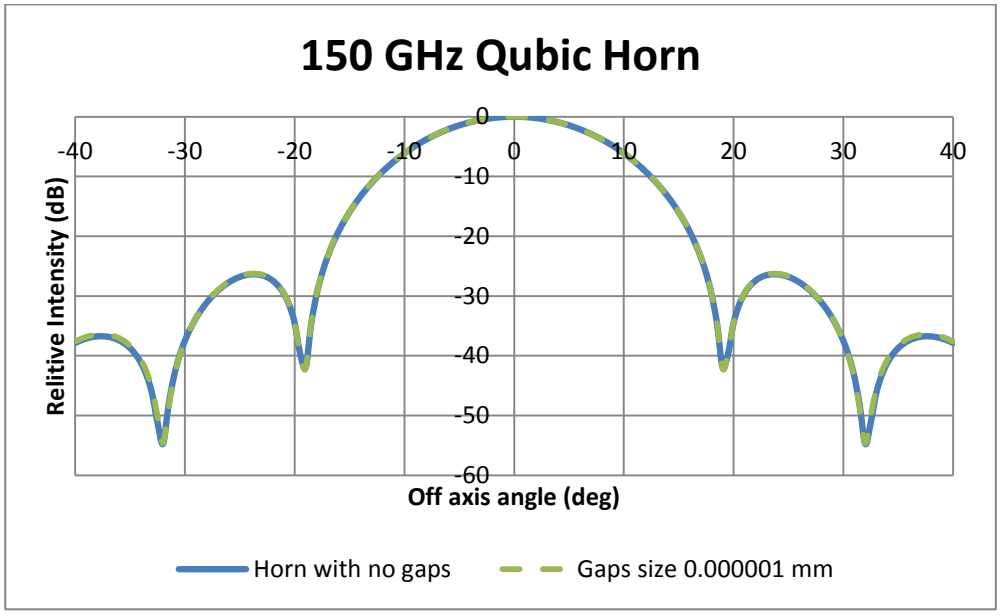

Figure 4.25 A test plot to ensure that the alterations made to the Scatter code have worked.

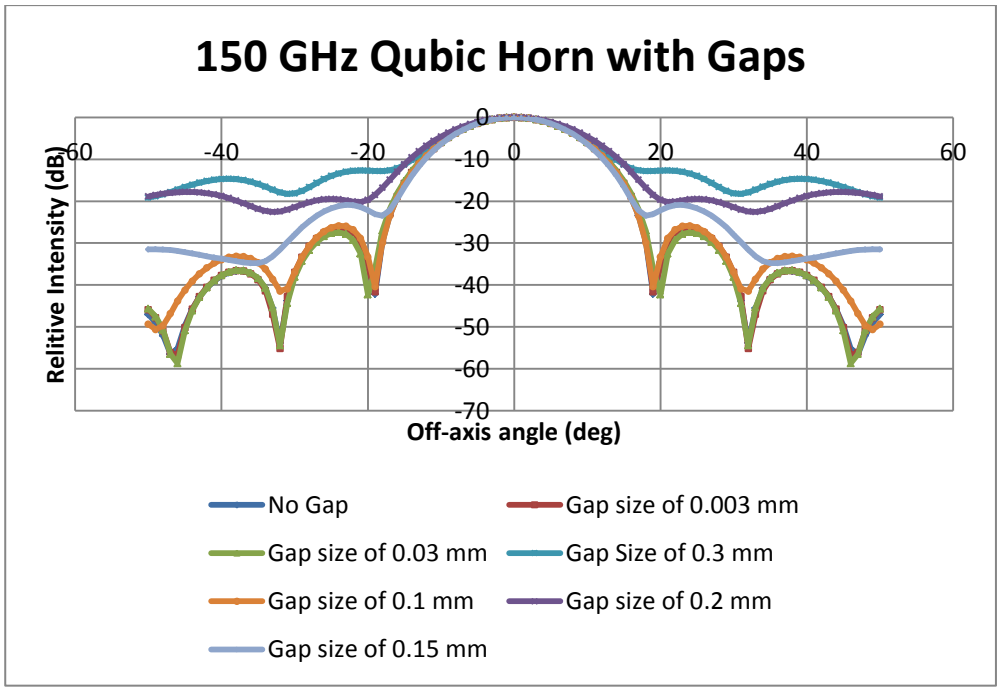

Figure 4.26 The co-polar beam patterns for the 150-GHz QUBIC horn with gap sizes ranging from 0 →0.3 mm.

The results (Figure 4.27) show that the gap sizes don't effect the beam pattern for gap sizes as small as 0.003 mm (λ/666) and 0.03 mm (λ/6.66). When we have a gap size of 0.1 mm, we see a small increase of about 3 dB in the third sidelobe. At 0.15 mm we see an increase in the first and second sidelobe. At 0.2 and 0.3 mm, we see the main beam width and sidelobe levels to be very high, the horn would not be able to be used for observations. In order to produce these results, the pseudoinverse was used for matrix inversion, as described in Chapter 3. The effects of adding gaps is summarised in the table below.

Horn Configuration	Gap Size (mm)	FWHM (dB)	Sidelobe Level (dB)
150 GHz Qubic Horn	0	-20.787	-25.899
150 GHz Qubic Horn	0.003	-20.787	-25.899
150 GHz Qubic Horn	0.03	-21.15135	-27.406
150 GHz Qubic Horn	0.1	-20.787	-25.899
150 GHz Qubic Horn	0.15	-11.7415	-20.982
150 GHz Qubic Horn	0.2	-10.095	-19.574
150 GHz Qubic Horn	0.3	-6.33	-12.747

Table 4.2 A summary of the effects of adding gaps has on the FWHM and Sidelobe levels

The effects of adding gaps between the corrugations was then investigated using CST however the results (Figure 4.28) showed that CST is not suitable for this, given the computing power available. Whereas CST was able to model the 100 GHz horn past the first sidelobe, at 150 GHz, anything outside the main beam is noisy. The best sampling rate achievable with the PC used for this thesis was λ/12 and so the CST mesh would not be fine enough to investigate gaps any narrower than this.

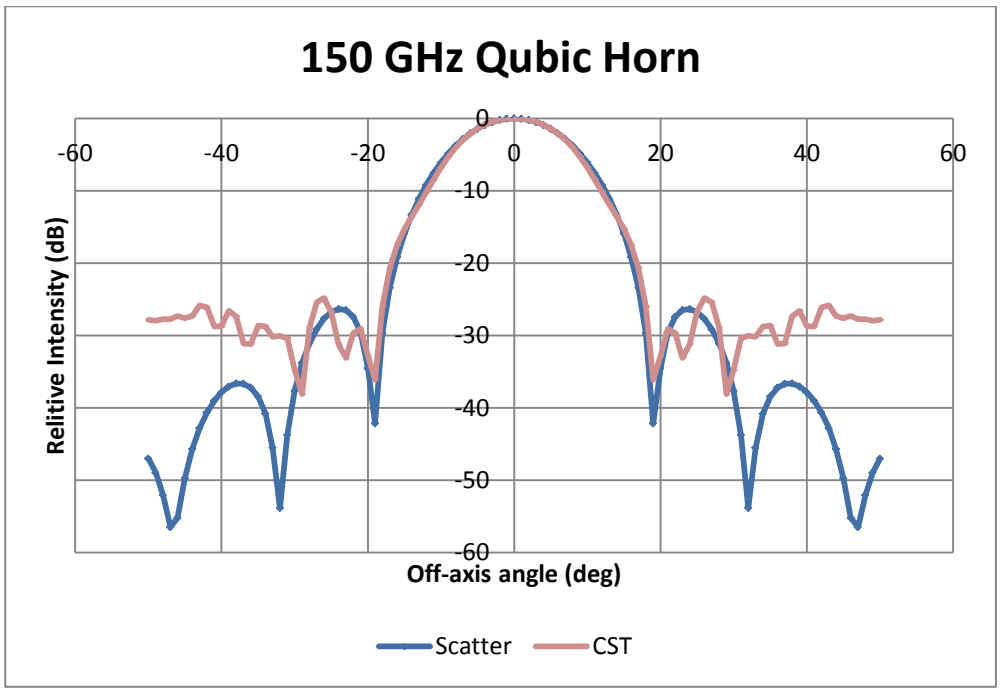

Figure 4.27 Co-polar beam patterns for the 150-GHz QUBIC horn without a gap. CST has a sampling rate of 12 lines per wavelength.

4.3.7 Random Variations to Corrugations

Next the effects of adding random variations to the radii of the corrugations horn was investigated. This simulated the effects of manufacturing errors (tolerances) when cutting the holes into the platelets. It was tested using Scatter code written on Wolfram's Mathematica 7.0 environment. To generate the random radii the code such as the following was added to the Scatter code:

$$\text{For}[i = 1, i < 192, i++; r[i] = r[i] - ((\text{RandomReal}[0.3]) - 0.15)]$$

This has the effect of adding a random variation between ±0.15 mm to each radius (r[i]). Figure 4.29 shows an example of a corrugated horn with random variations added to the radii of the corrugations. The random variations added to the radii of the corrugations varied between ±0.1 mm, ±0.15 mm, ±0.2 mm and ±0.25 mm. The simulations used uniformly distributed random numbers.

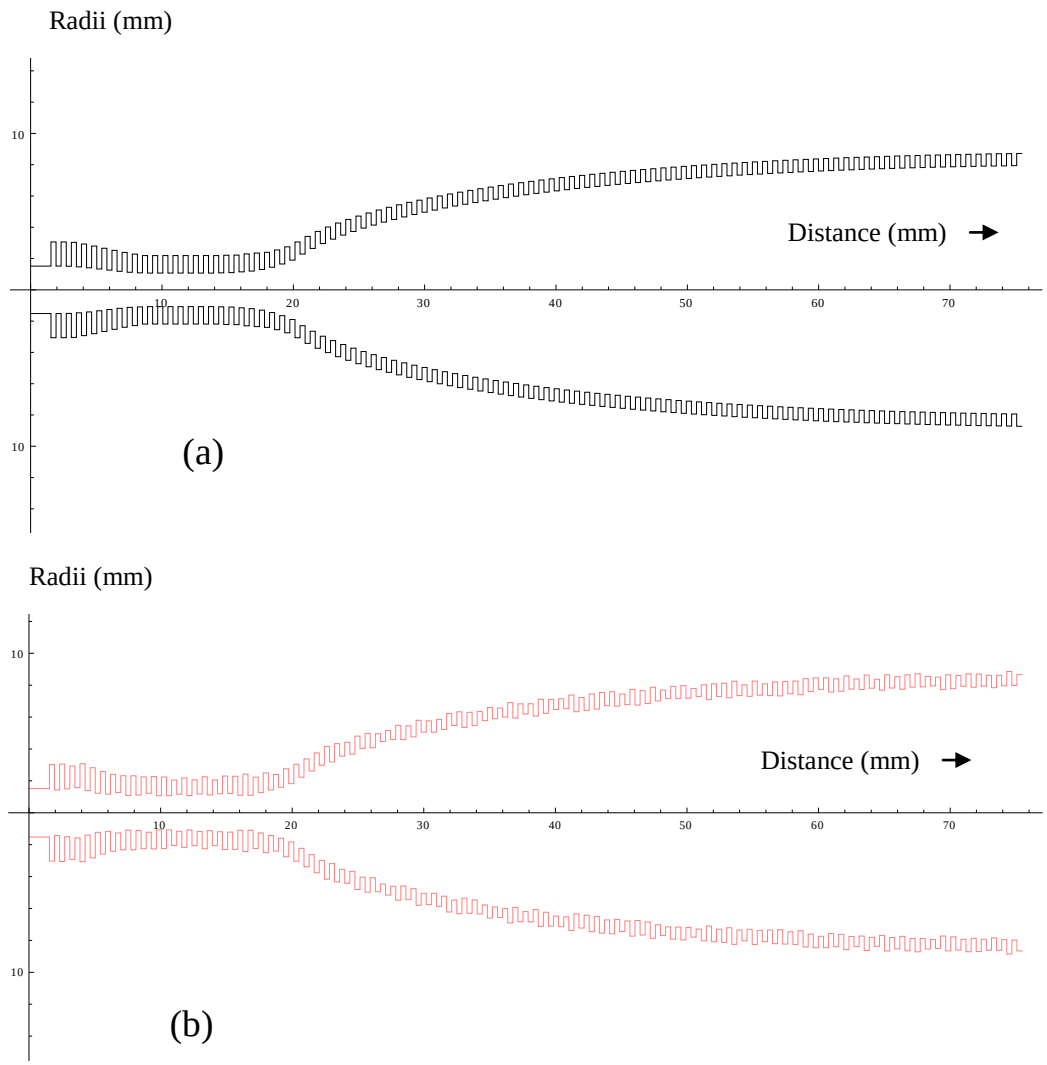

Figure 4.28 QUBIC horns generated using Scatter, (a) is the original unaltered QUBIC horn, (b) is the QUBIC horn with random variations introduced to the corrugations.

The results (Figures 4.30 and 4.31) for adding random variations between ±0.1 mm and ±0.15 mm shows very little effect on the main beam pattern. The most noticeable effect is in the sidelobe levels where they increase from -30 to -25 dB. The results (Figures 4.32) for adding random variations between ±0.2 mm show that the intensity of the main beam is lower (increased return loss), the main beam width is wider and lower sidelobes. At variations between ±0.25 mm the intensity of the main beam could reach as low as -30 dB and in some cases there are no distinct sidelobes.

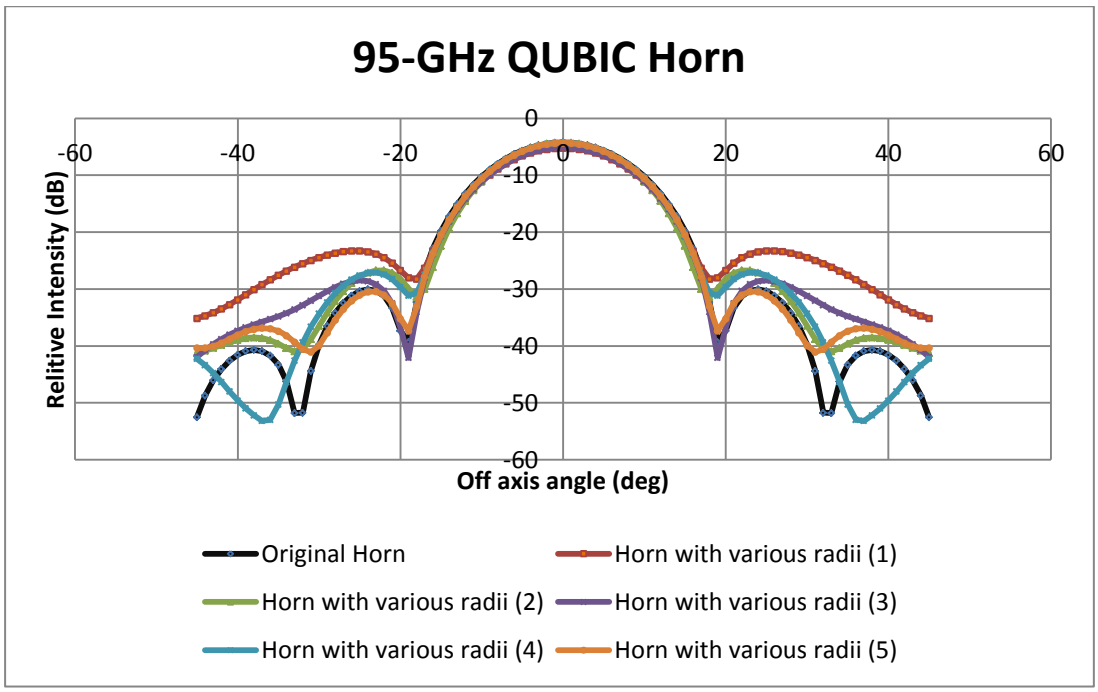

Figure 4.29 The co-polar (E-cut) beam patterns of a QUBIC horn operating at 95-GHz. The radius of the corrugations were changed by an amount varying between ±0.1mm

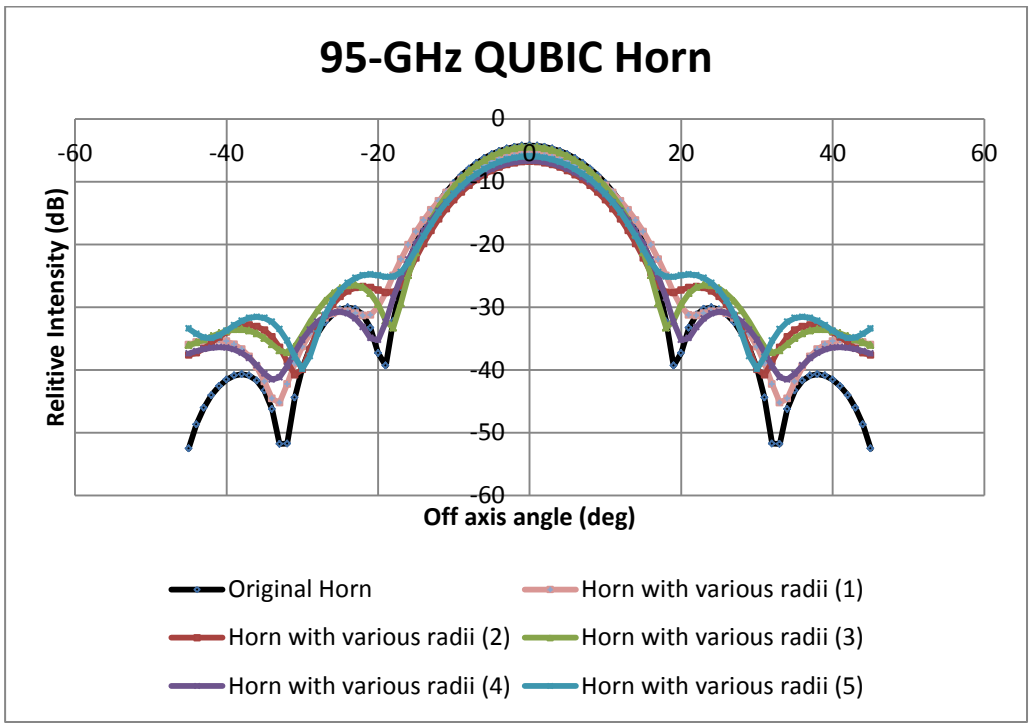

Figure 4.30 The co-polar (E-cut) beam pattern of a QUBIC horn operating at 95-GHz. The radius of the corrugations were changed by an amount varying between ±0.15 mm

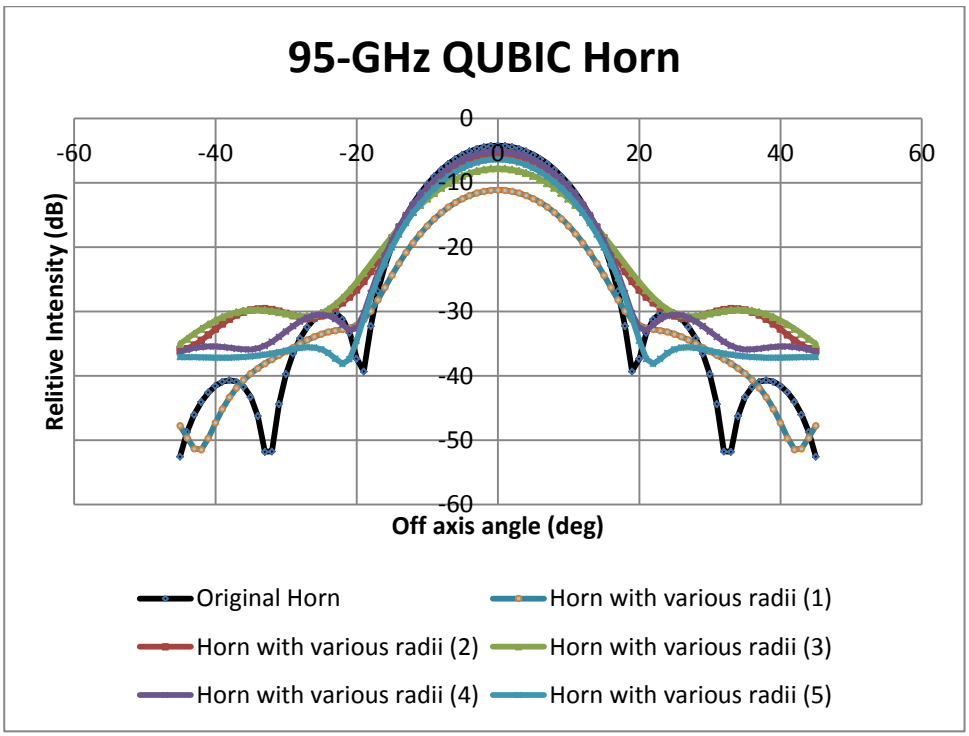

Figure 4.31 The co-polar (E-cut) beam pattern of a QUBIC horn operating at 95-GHz. The radius of the corrugations were changed by an amount varying between ±0.2 mm.

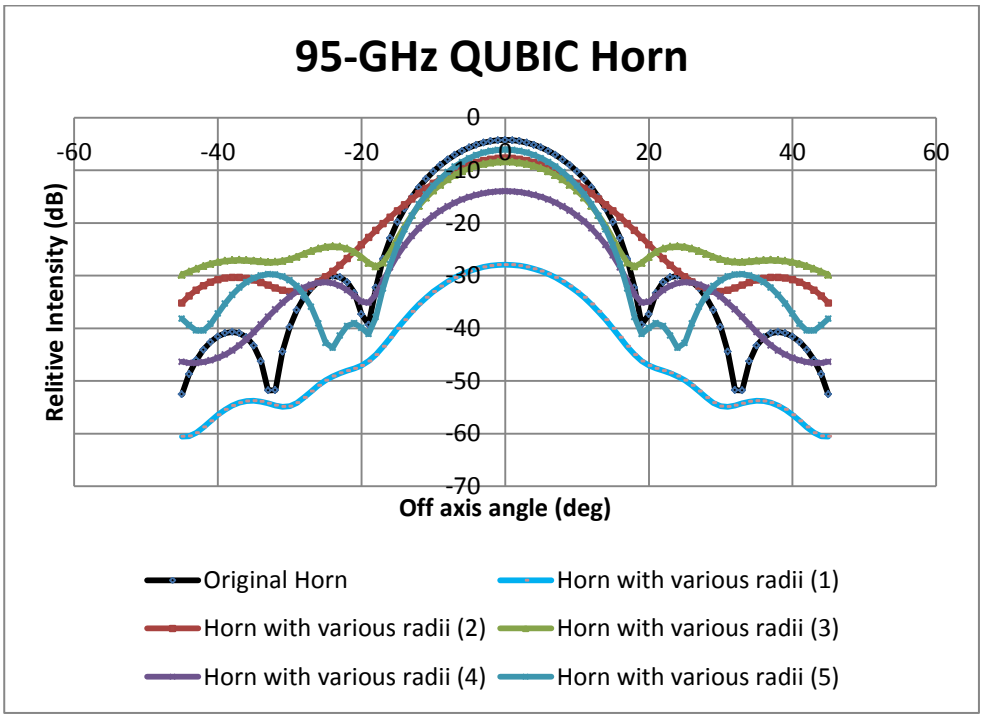

Figure 4.32 The co-polar (E-cut) beam pattern of a QUBIC horn operating at 95-GHz. The radius of the corrugations were changed by an amount varying between ±0.25 mm.

4.4 Summary

In this chapter, I have examined the use of platelet formed horns that will be used in the QUBIC telescope. QUBIC is a ground based telescope that will be mainly used to detect B-modes which were created during the inflationary stage of the big bang. To detect these B-modes sensitive and accurate detectors are needed. It was for this reason that the manufacturing issues that can arise when dealing with platelet formed horns were investigated in this chapter.

The first issue that can occur with platelets is the structural instability caused by cutting many holes into thin platelets. A possible solution to this is to add a single thick plate onto the array (the thick plate could also act as a filter holder). Two scenarios were tested, a smooth thick plate and a corrugated thick plate. They were both modelled in CST and Scatter. They were also tested experimentally using the VNA laboratory here at NUI Maynooth. The horn used in the simulations and experiment was the 100-GHz corrugated horn which was similar in design QUBIC horns. It was found that corrugating the thick plate would not be necessary.

The second issue that could occur is gaps between the platelets. This could happen if the platelets aren't clamped down tightly. Both Scatter and CST were used to test this, but due to the lack of computational power available the results obtained by CST were too inaccurate to use. Alterations were made to the C version of Scatter to generate a finite gap between the corrugations. A number of models were simulated with gap sizes ranging from $\lambda/10^3$ to $\lambda/10$. As the gap size approached $\lambda/10$ there was a significant degradation of the beam pattern. Experimental measurements showed that sufficiently small gaps (with no bonding between layers) could be achieved with rings simulating platelets.

The third and final issue investigated was the possibility that the holes in the plates weren't cut accurately enough. To test this, random variations were added to the radii of the corrugations. These random variations were added to the radii using Mathematica and the effects were measured using Scatter in the same environment. Again, results show that typical manufacturing tolerances are sufficient.

Chapter 5 Analysis of Electroformed Corrugated Horns for the Planck Telescope

5.1 Introduction

This chapter discusses the properties and, in particular, the tolerances of electroformed horns that were used in the Planck telescope. It first presents an overview of the Planck telescope which was designed for ESA's mission to map the cosmic microwave background temperature and polarization anisotropies. The reasons for making these measurements were discussed in Chapter 1. Then it describes the process involved in the making of the feedhorns used in Planck and the analysis of the possible errors that can occur with these types of horns.

5.2 Planck

The Plank mission [45] was designed to image the temperature and polarization anisotropies of the CMB radiation. It was equipped with two instruments: the radiometric Low Frequency Instrument (LFI)(cooled to 20 K) and the bolometric High Frequency Instrument (HFI)(cooled to 100 mK). They were attached to an optimized dual reflector off-axis telescope with a 1.5-m projected aperture. The LFI measured the radiation from the sky between 30 and 100 GHz and the HFI measured the radiation between 100 and 857 GHz. The telescope was cooled to 50 K and was protected from solar radiation by three shields.

5.2.1 Instrumental set up

The Planck satellite was designed as two main modules; the first being the payload module which contained the off-axis telescope and the detectors of the

LFI and the HFI, the second module contained the warm electronics used to run the instruments and satellite, the solar panel that provided power, the onboard computer, the command receivers and telemetry transmitters. The telescope was based on a dual mirror off-axis scheme. The mirrors, both primary and secondary, were elliptical as in the case of the Gregorian aplanatic design. LFI and HFI were located in the focal region (Figure 5.1). The Terahertz Group in NUI Maynooth was involved with the HFI instrument.

The HFI covered six bands centred at 100, 143, 217, 353, 545 and 857 GHz. It was designed with 52 bolometers, twenty of them sensitive to power only and thirty two of them sensitive to polarization. They were all operated at a temperature of 0.1 K. To couple radiation onto the bolometers HFI was equipped with 36 feeds (20 with single bolometers and 16 with 2 polarisation bolometers) with a triple horn configuration (Figure 5.2).

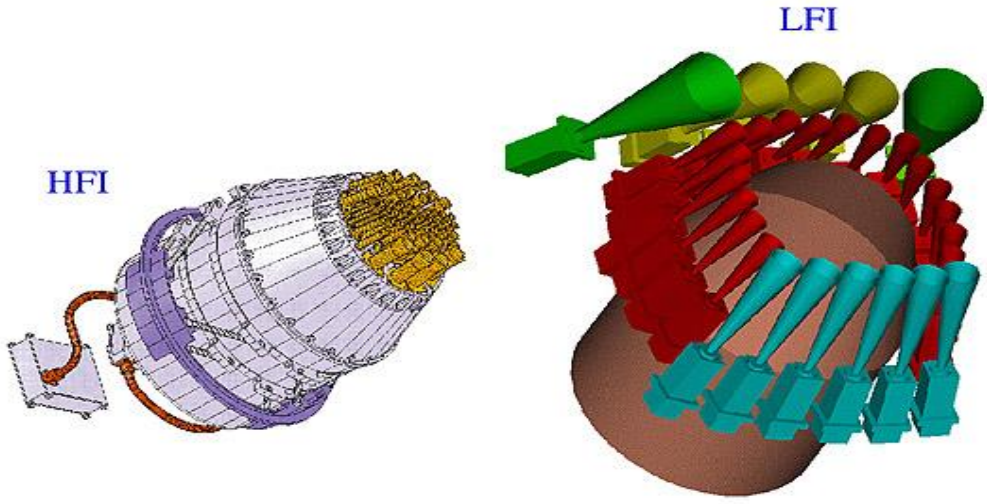

Figure 5.1 Schematic of both HFI and LFI on the Planck telescope focal plane [46].

The LFI consisted of 11 radiometric receivers operating at frequencies close to 30, 44 and 70 GHz. They were situated in a ring around the HFI. LFI had a dual corrugated horn design.

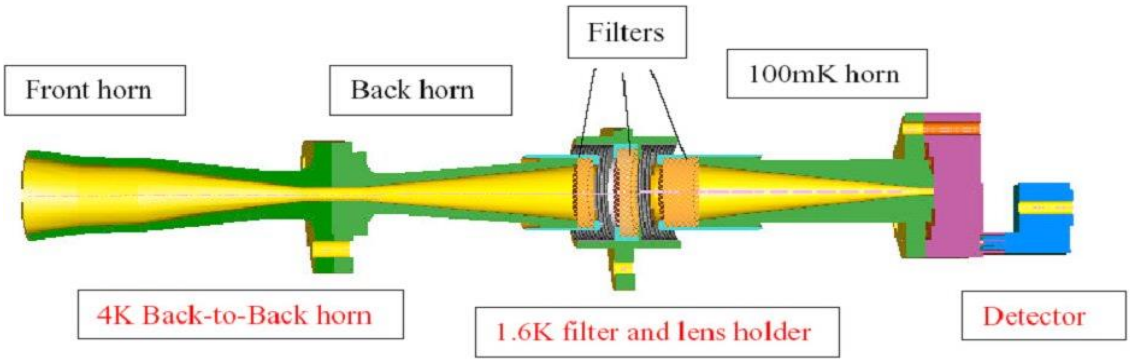

Figure 5.2 A schematic of the horn set up [47].

Because of Planck's oversized mirrors the beam shape on the sky was determined by the horns. There were some features of the Planck CMB map released in 2013 that appeared to be due to the presence of far out sidelobes at a level slightly higher than predicted by modelling. These sidelobes, when aligned with the Galactic plane, produced long streaks in the Planck maps [48].One of the aims of this research was to see if manufacturing tolerances, such as damages to the corrugations of the horn, that may not have been visible, could have caused this increase in sidelobe level.

5.3 Electroformed Horns

The corrugated horns that were used in both the LFI and HFI were created using a method called "electroforming" (Figure 5.5). It is the most commonly used method for such horns and consists of machining the horn's internal geometry onto the surface of an aluminium mandrel. This mandrel is then placed into a copper electrolytic solution along with the positively charged electroformed metal source (anode) (usually a copper/nickel compound in the case of a feed-horn). The mandrel is negatively charged (cathode). The anode is then broken down (ionised) in the solution and is electrochemically deposited onto the mandrel. The build-up is achieved over all the mandrel surfaces at an approximate

deposition rate of 0.001" per hour. The process is continued until the required horn thickness is achieved. This process becomes difficult when dealing with horns operating at the highest Planck frequencies because the corrugation widths and lengths required are small.

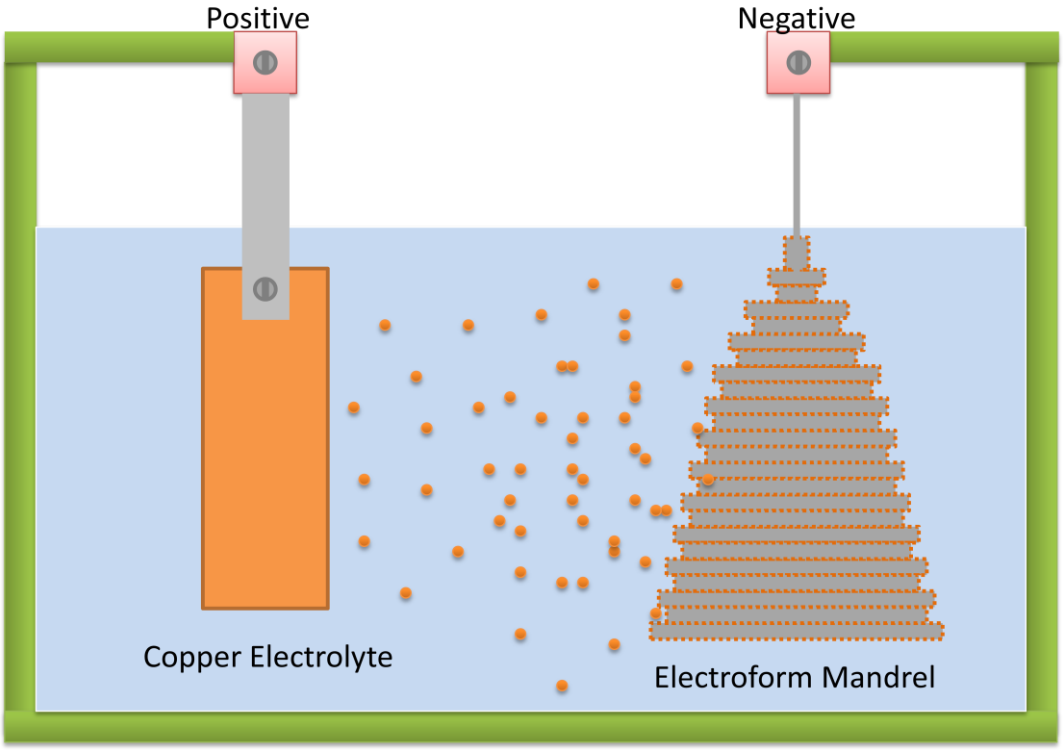

Figure 5.3 The electroforming process.

5.4 Analysis of Electroformed Horns

The possible manufacturing issues that can arise when dealing with electroformed horns are:

- The filling or partial filling of the corrugations due to parts of the mandrel being left in the horn.
- The damaging or partial damaging of the corrugations.

These errors are shown schematically in Figure 5.4. The effects of these manufacturing errors on the symmetry of the main beam, cross-polarization and the sidelobe levels were investigated.

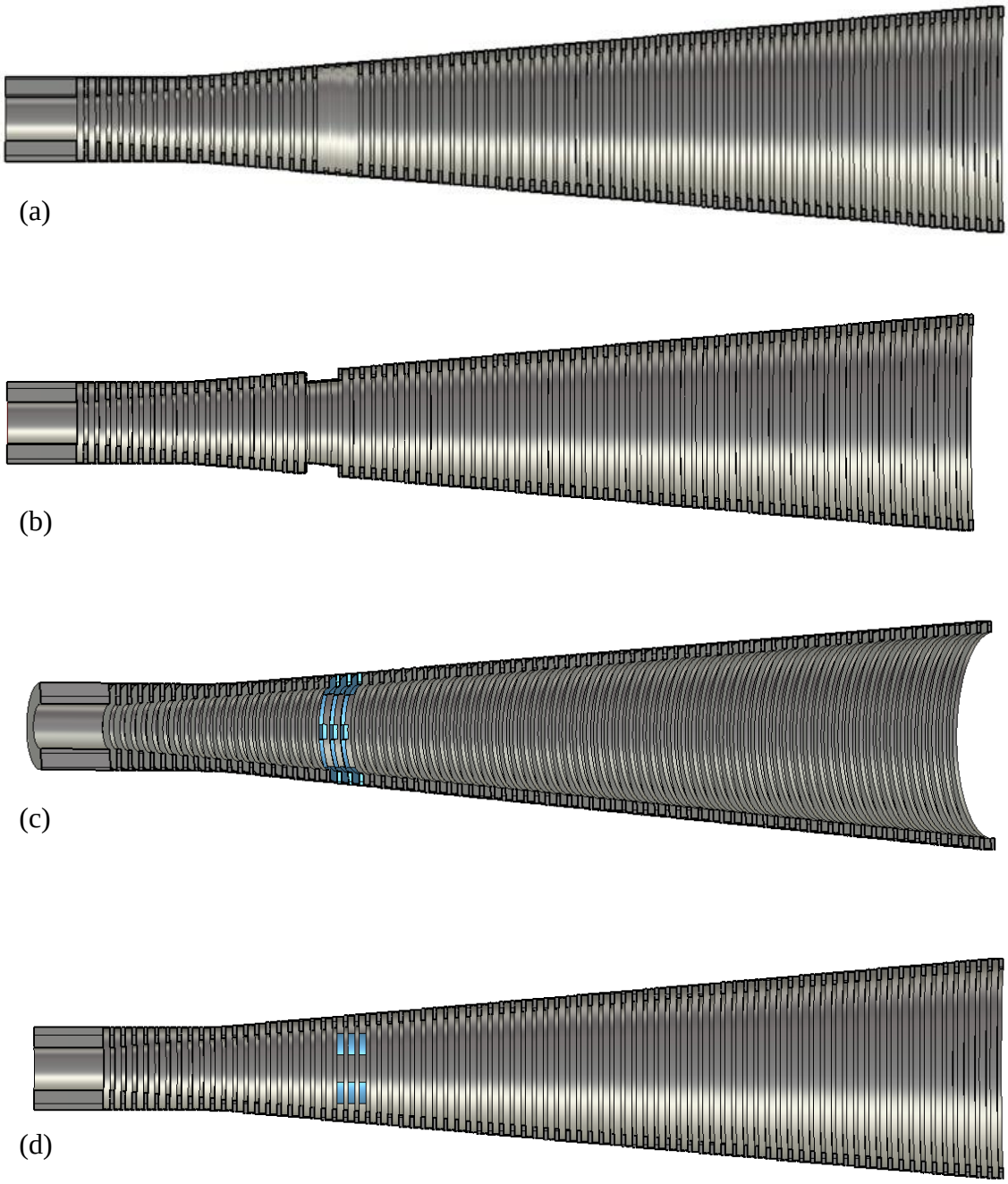

Figure 5.4 (a) A corrugated horn where three of the corrugations have been removed. (b) A corrugated horn where three of the corrugations have been filled. (c) A corrugated horn where three of the corrugations have been partially removed. (d) A corrugated horn where three of the corrugations have been partially filled (Diagrams were generated using CST).

5.4.1 Filled Corrugated Horn

Initially it was decided to look at the effect of corrugations that were completely filled (a rotationally symmetric problem). The high frequencies used in the HFI make modelling the high-frequency Planck system impractical (with

CST) and so it was decided to use a low-frequency version to test the effects. The horn under test was a single-moded (HE_{11}), 100-GHz corrugated conical horn which consisted of 163 corrugations. The aim was to find out whether filling a small number of corrugations could affect the beam quality, and whether any particular location was especially important. There were five locations along the horn that were tested, the throat of the horn, between the throat and the centre of the horn, the centre, between the centre and the aperture, and the aperture (Figure 5.5). The results (shown Figures 5.7-5.12) were calculated using the mode-matching method (implemented in Scatter). Scatter was used for fully filled corrugations as it is faster than CST however since CST must be used for the partially filled case, CST and Scatter results were compared to provide a benchmark and as a useful validation of different techniques. The Scatter work was carried out in collaboration with Ian McAuley of NUI Maynooth.

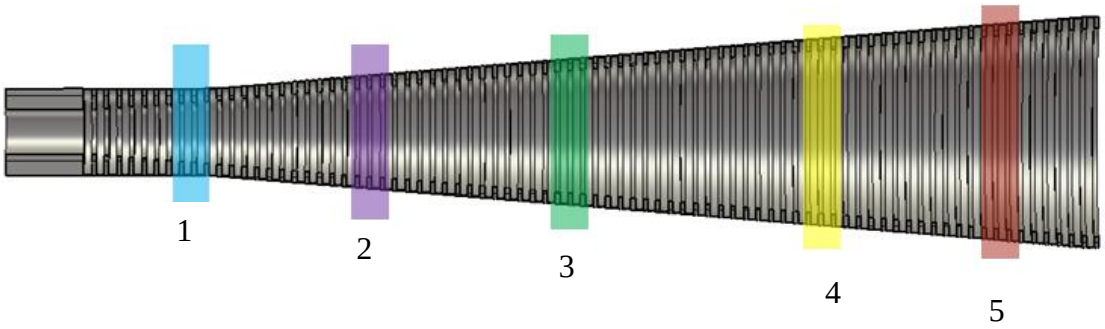

Figure 5.5 A corrugated horn indicating the locations where the corrugations were raltered. The locations are coloured to match the colours of the results plotted in Figures 5.7-5.12.

To simulate filling the corrugations, the horn's "geometry file", which contained the lengths and radii of the corrugations, was altered (Figure 5.6). The outer radii of the corrugations were reduced to almost the same size of the inner radii. This created one long section with very small corrugations.

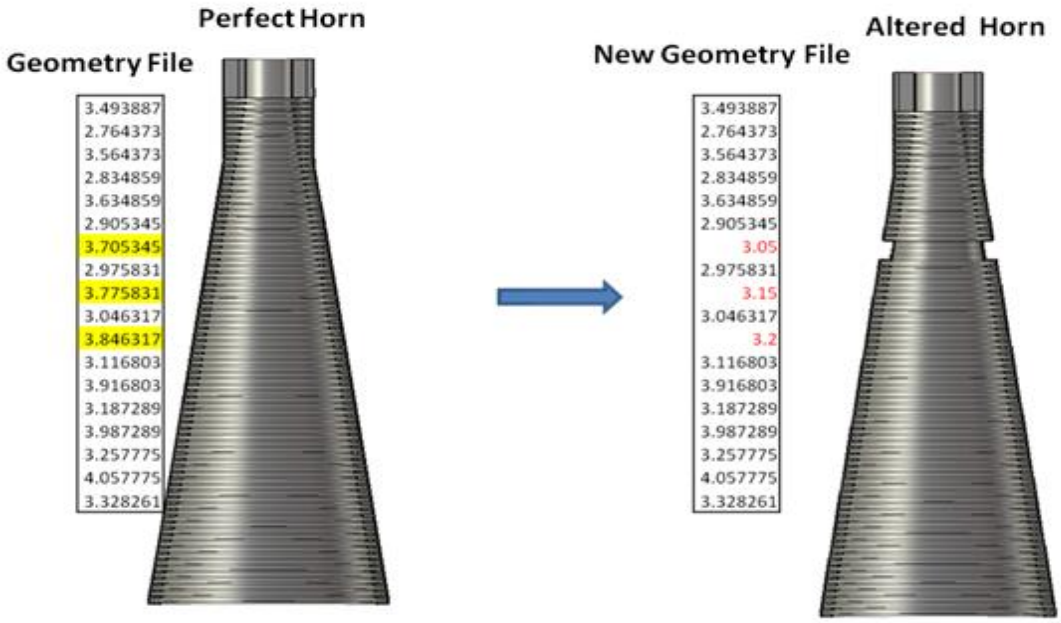

Figure 5.6 Three corrugations being filled by altering the geometry file.

The results in Figure 5.7 and Figure 5.8 show that filling in even a single corrugation does have an effect but this effect depends on the location of the filled corrugation. The co-polar results (Figure 5.7) show filling at positions 1, 4 and 5 produce little change in beam symmetry and sidelobe levels. Filling at position 2 shows the beam pattern losing symmetry and an increase in sidelobe level. At position 3 there is a loss in beam symmetry and an increase in sidelobe level but not as severe as position 2. None of these results produce a symmetrical beam pattern with higher sidelobe levels which is believed to be the cause of some of the features in the Planck map. The cross-polar results (Figure 5.8) show that filling at position 1 produces a very small effect, positions 2 and 3 produce higher cross-polarization, positions 4 and 5 produce a small increase in cross-polarization level.(All cross-polar patterns shown were calculated for cuts at 45°.)

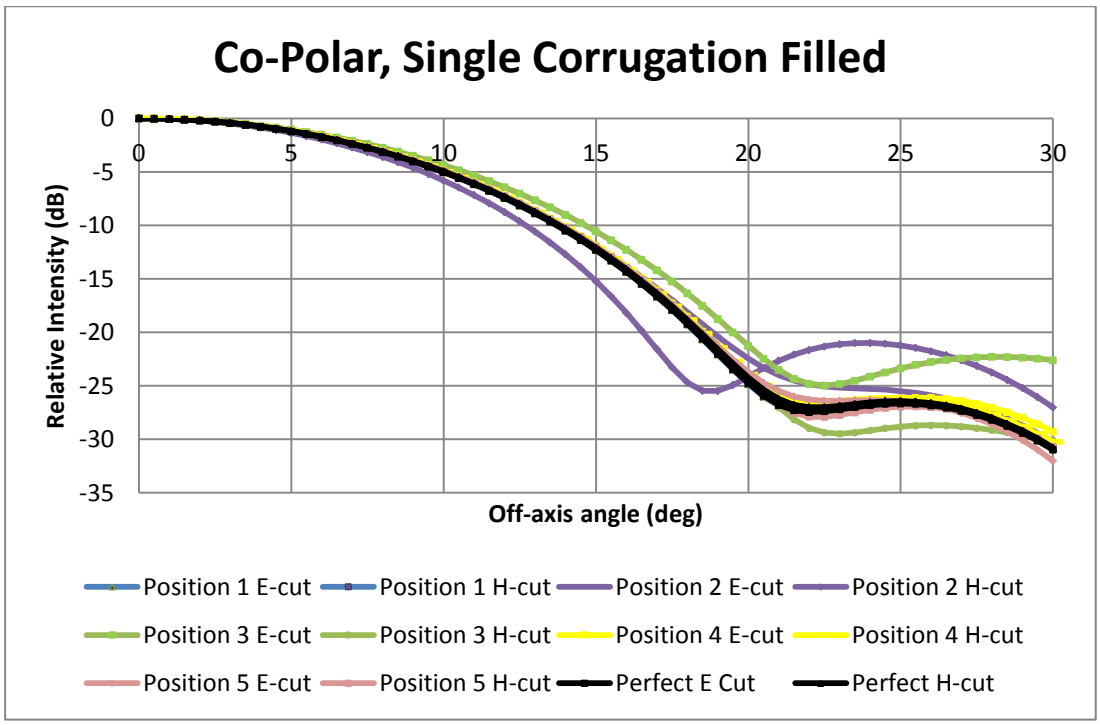

Figure 5.7 Co-polar power as a function of off-axis angle for a corrugated horn which has had one corrugation filled in. The position of the filled corrugation is given by the colour (see Figure 5.5). A horn without any filled corrugations was plotted for comparison (in black).

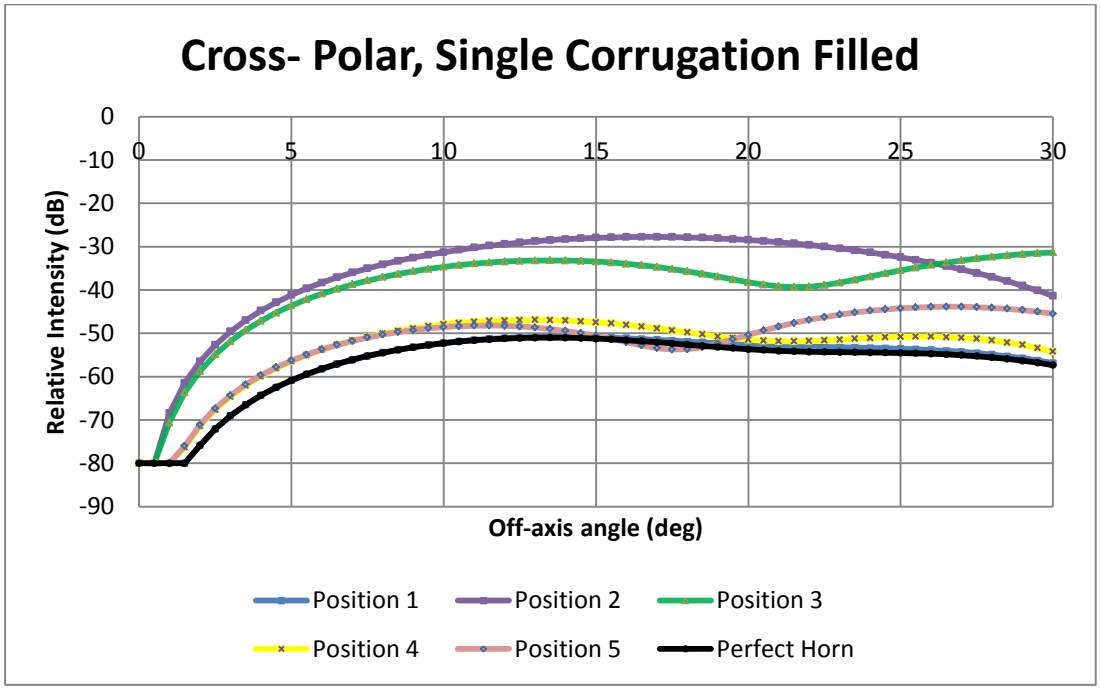

Figure 5.8 Cross-polar power as a function of off-axis angle for a corrugated horn which has had one corrugation filled in. The position of the filled corrugation is given by colour (see Figure 5.5). A horn without any filled corrugations was plotted for comparison (in black).

The effects on co-polar power of filling two corrugations (Figure 5.9) were similar to those seen when filling in a single corrugation. However, the results show a loss of beam symmetry and a change in sidelobe level when filling two corrugations at position 4 and 5. Filling in two corrugations has a greater effect on cross-polarization (Figure 5.10) compared to a single corrugation being filled with an increase in all cases. Most notably there is a significant increase in cross-polarization at position 4 and small decrease at position 3 in comparison to a single filled corrugation. In position 3 there is only a small effect on the main beam but an increase in sidelobe level (in on direction). This effect was seen in Planck.

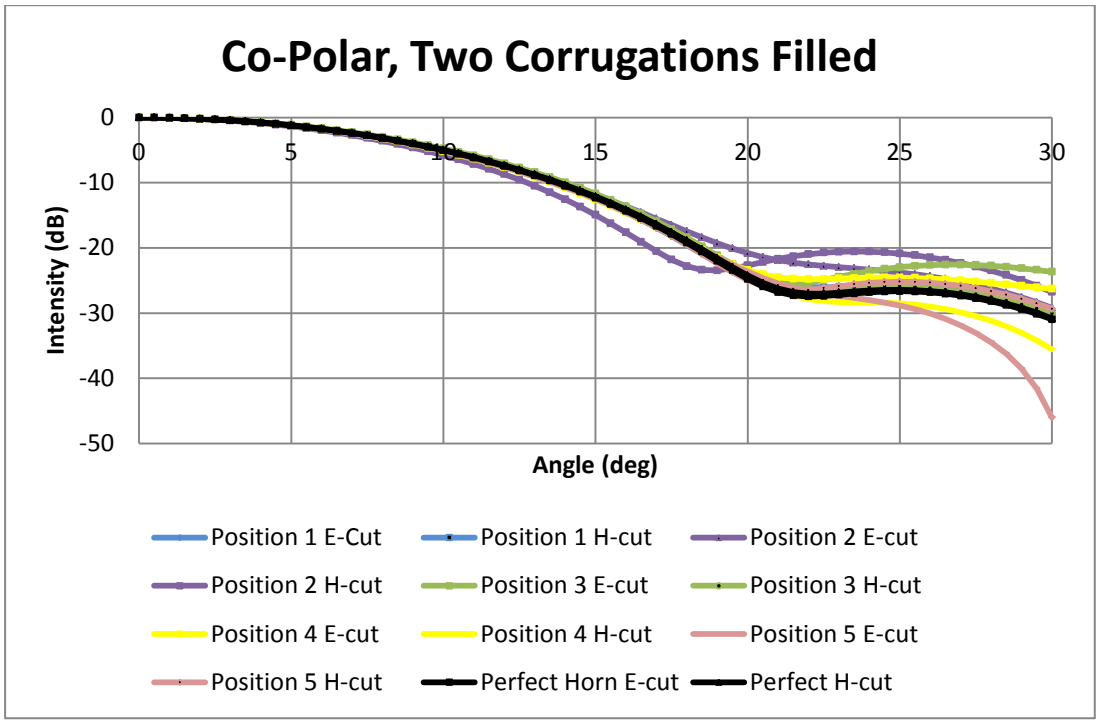

Figure 5.9 Co-polar power as a function of off-axis angle for a corrugated horn which has had two corrugations filled in. The position of the filled corrugation is given by the colour (see Figure 5.5). A horn without any filled corrugations was plotted for comparison (in black).

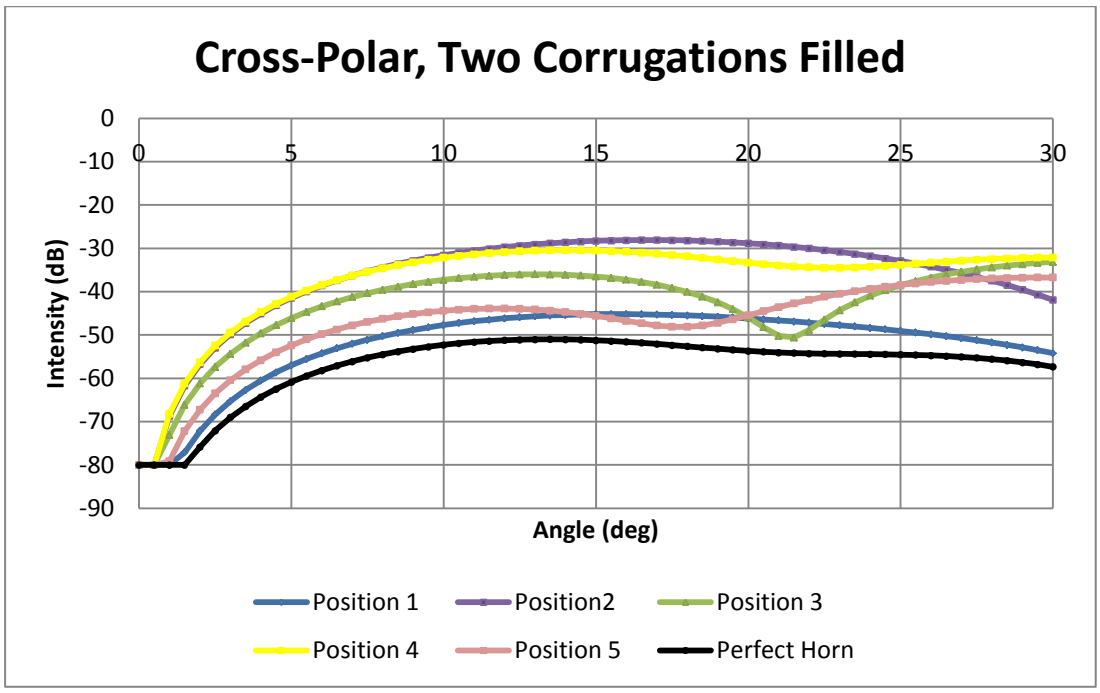

Figure 5.10 Cross-polar power as a function of off-axis angle for a corrugated horn which has had one corrugation filled in. The position of the filled corrugation is given by colour (see Figure 5.5). A horn without any filled corrugations was plotted for comparison (in black).

With three corrugations filled the beam is highly asymmetric with sidelobe levels thatare higher for most of the positions (Figure 5.11). Filling at position 1 produces a beam that is symmetric with sidelobe levels that are slightly lower. The cross-polarization levels are all high except at position 1.

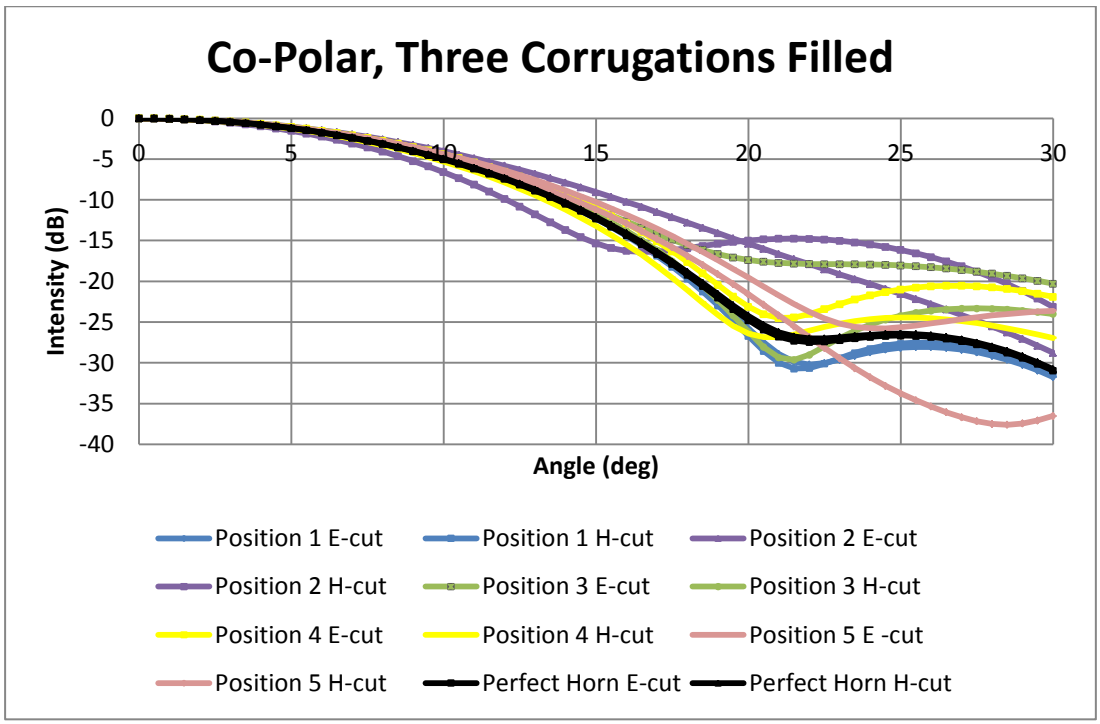

Figure 5.11 Co-polar power as a function of off-axis angle for a corrugated horn which has had three corrugations filled in. The position of the filled corrugation is given by the colour (see Figure 5.5). A horn without any filled corrugations was plotted for comparison (in black).

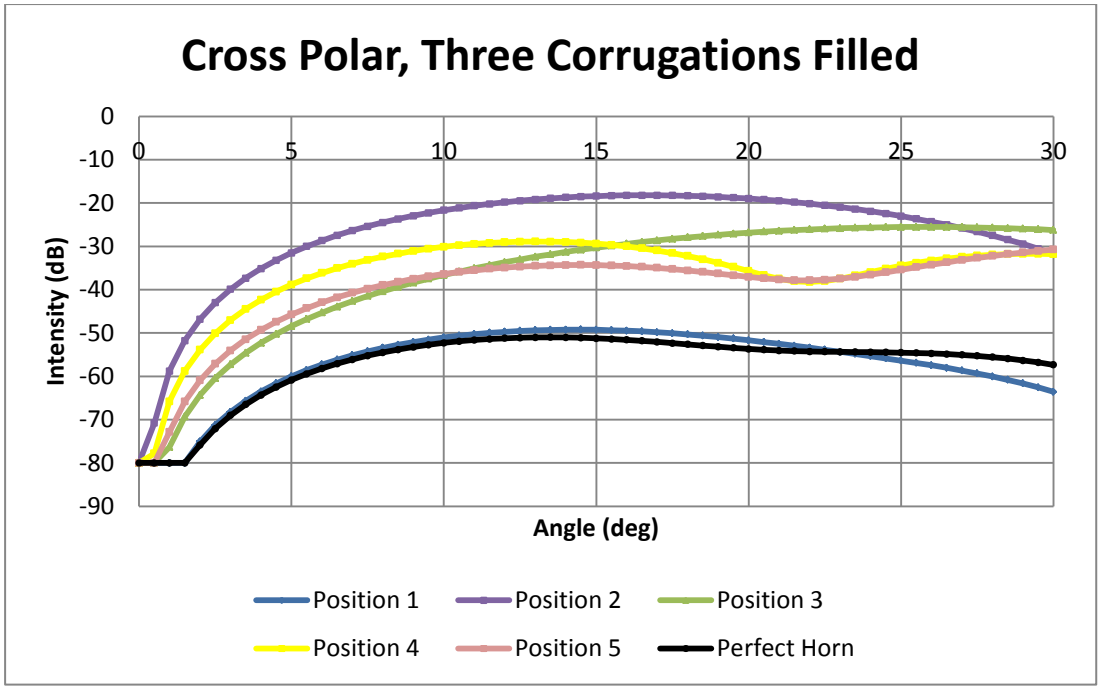

Figure 5.12 Cross-polar power as a function of off-axis angle for a corrugated horn which has had one corrugation filled in. The position of the filled corrugation is given by colour (see Figure 5.5). A horn without any filled corrugations was plotted for comparison (in black).

An important result of this work is that filling (simulating incomplete removal of the mandrel) even a small number of corrugations can have a significant effect on the beam shape. The results above show that the more corrugations that are filled the greater the effect on cross-polar and co-polar beam patterns, as expected. The level of the effect seen with different number of corrugations filled is shown in Figures 5.13 and 5.14. The difference between filling one or two corrugations is small but filling three corrugations can drastically change the nature of the beam. Filling the corrugations at position 2 on the horn produces the greatest effect where filling at position 1 produces the least effect. The possible reason for this is that position 2 is the region of the horn were the higher order modes are being generated and at position 1 the beam has not been fully formed and has time to recover. Positions 3, 4 and 5 are the regions of the horn designed to reduce the side lobes. The results show for these positions that beam symmetry has been affected but not to the same extent as the side lobe level.

To confirm that these results are accurate the results for the three corrugations filled at position 2 calculated with Scatter, were compared to CST simulations, which uses a different technique, (Figure 5.15) and were found to show close agreement. Since CST cannot be configured to measure the cross-polarization it was only the co-polar results that could be compared.

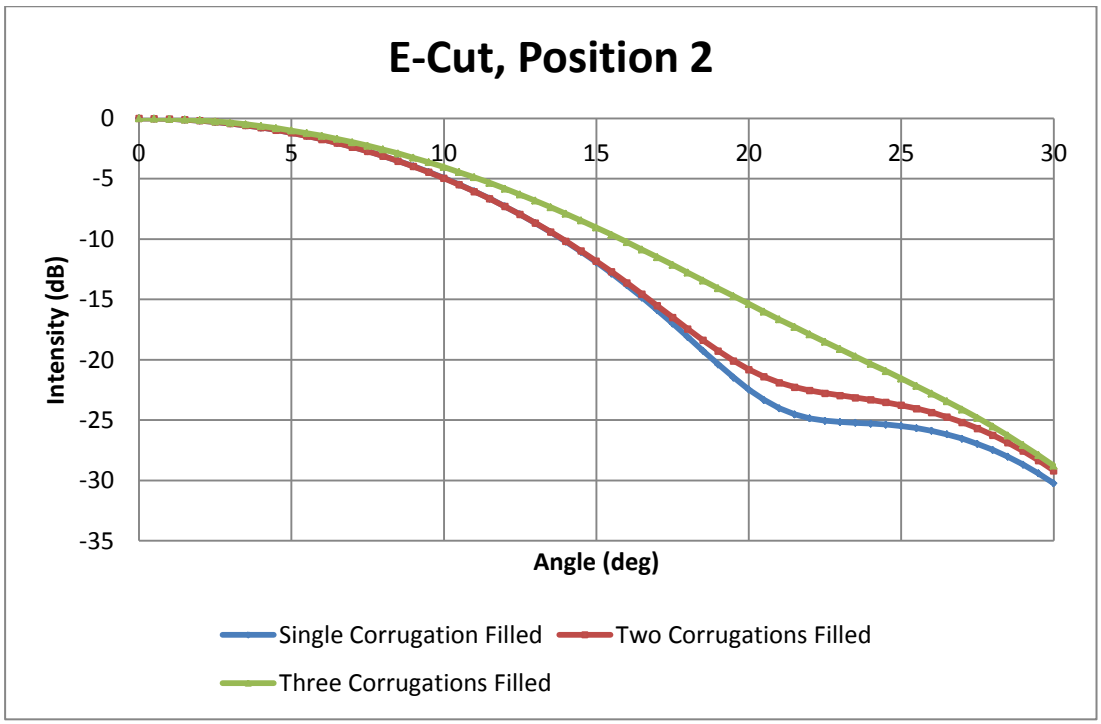

Figure 5.13 Beam pattern (E-cut) for different number of corrugations filled at position 2.

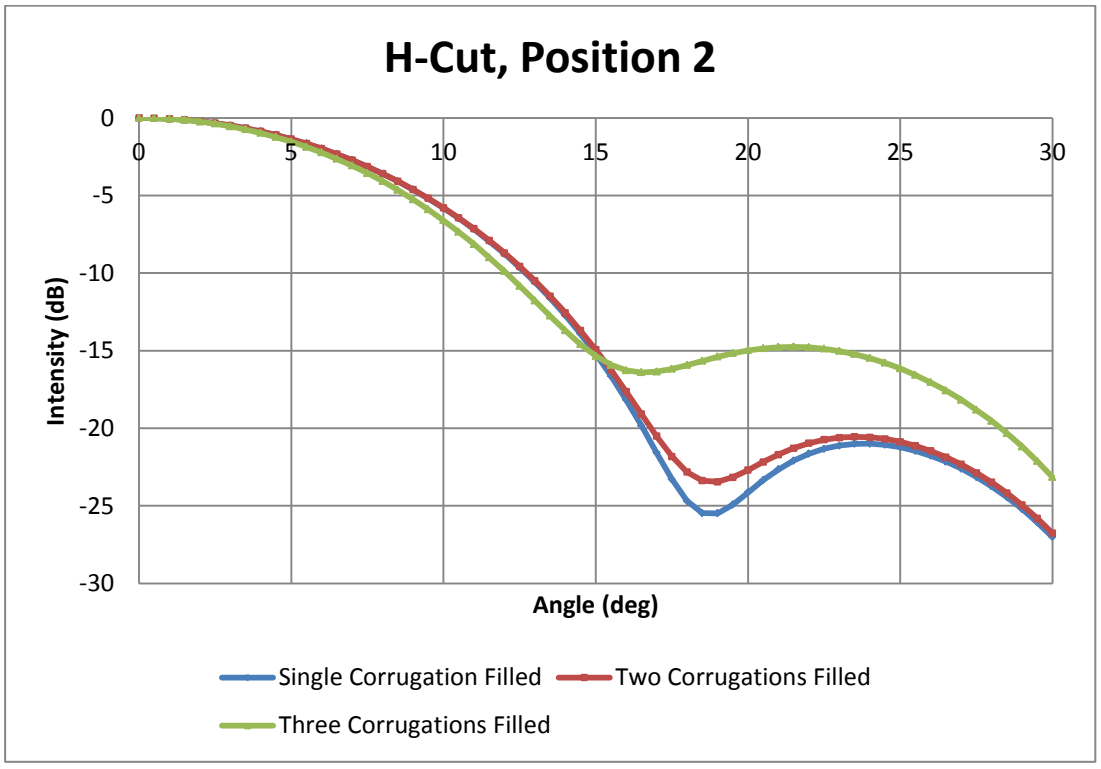

Figure 5.14 Beam pattern (H-cut) for different number of corrugations filled at position 2.

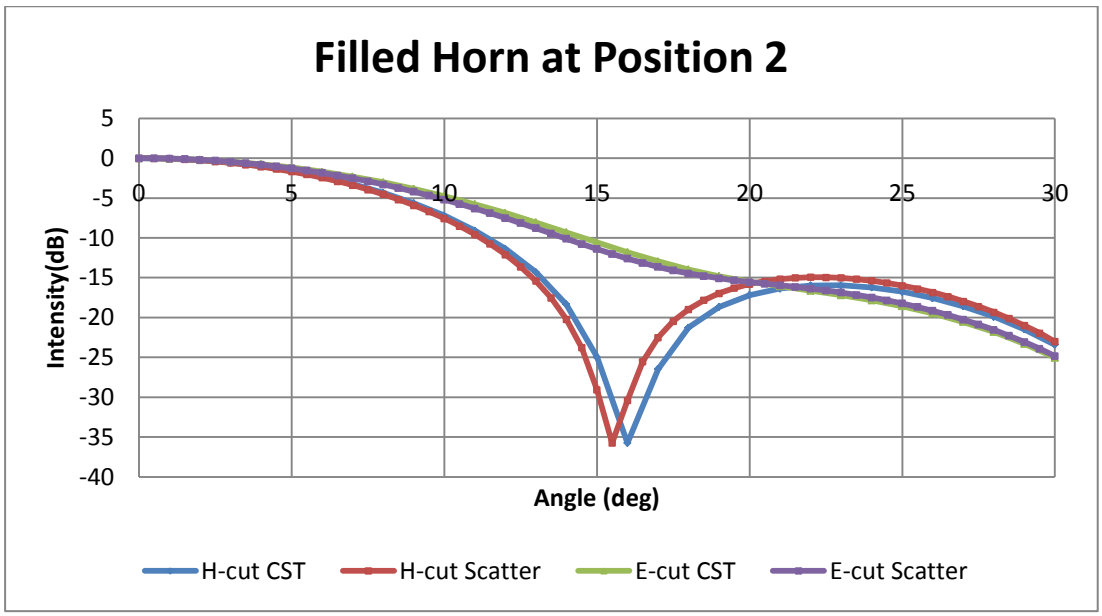

Figure 5.15 E and H plane cuts of the beam pattern from a corrugated horn with three corrugations filled at position 2 (see Figure 5.5). The beam patterns were calculated using Scatter and CST.

The results above (Figures 5.7-5.15) are for the corrugated horn operating at 100 GHz. The effects of filling in three corrugations at position 2 were then measured at different frequencies throughout the horn's bandwidth (85, 90, 95, 105, 110 and 115 GHz)(Figures 5.16-5.18). The individual results for each frequency are given in Appendix B, and summarised here.

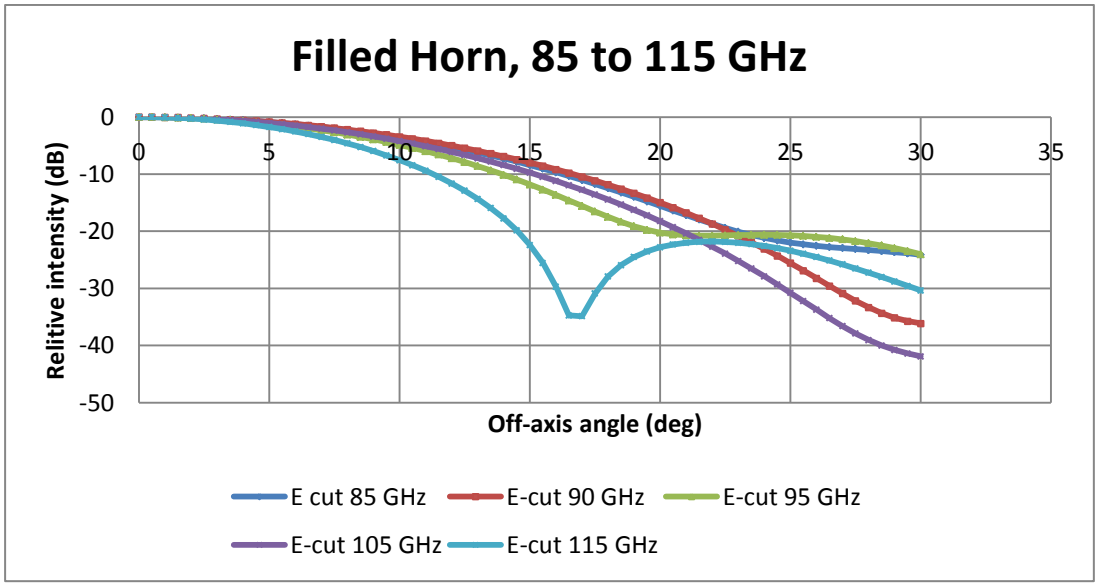

Figure 5.16 The co-polar (E-cut) results for filling three corrugations at position 2, operating between 85 GHz and 115 GHz

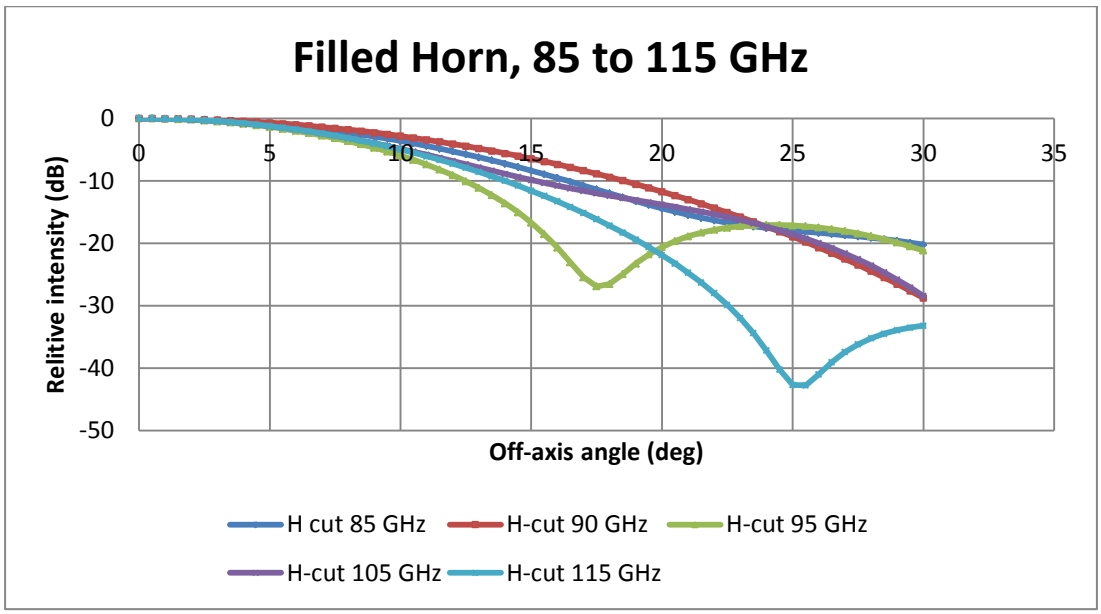

Figure 5.17 The co-polar (H-cut) results for filling three corrugations at position 2, operating between 85 GHz and 115 GHz

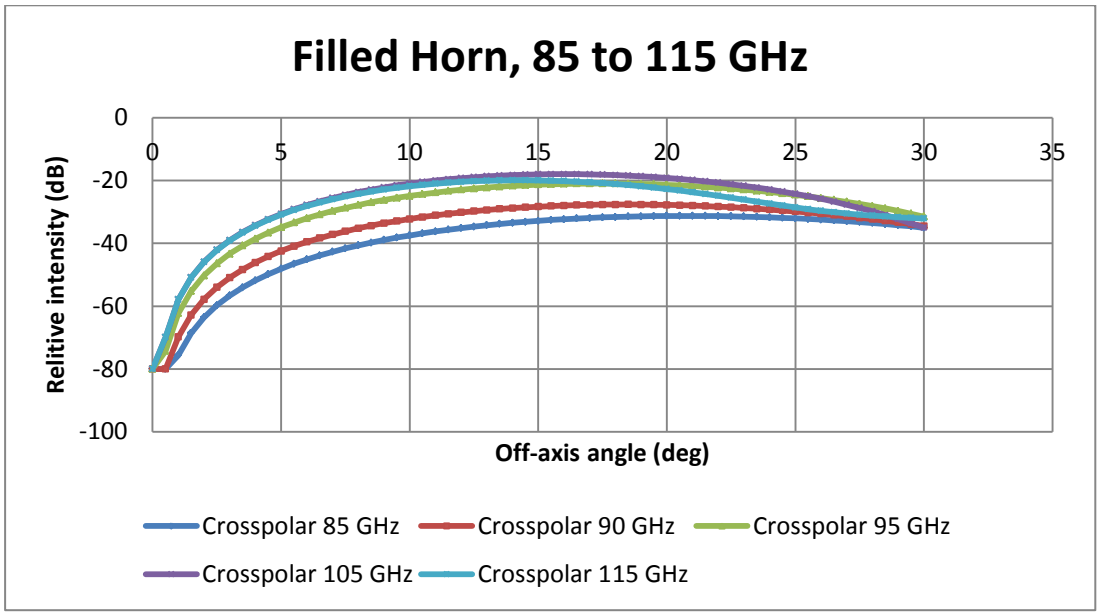

Figure 5.18 The co-polar (crosspolar) results for filling three corrugations at position 2, operating between 85 GHz and 115 GHz

The results (Figures 5.16-5.18) show that as the frequency increases the effects on beam symmetry and cross-polarization levels increase slightly. The co-polar results at 85 GHz and 90 GHz show very little difference between E and H-cuts, the beam pattern is almost symmetrical. When the frequency is increased to 95 and 105 GHz there is noticeable difference between the E and H-cuts, the beam

pattern is less symmetric than at the lower frequencies. At 115 GHz the E and H-cuts are completely different.

At 85 GHz the cross-polarization peaks at -30 dB and is 10 dB higher than a perfect horn. Increasing the frequency shows an increase in the cross-polarization level and the highest level was at 105 GHz peaking at -18 dB, an increase of 35 dB from a perfect horn.

5.4.2 Damaged Corrugated Horn

What I refer to as 'damaged horns' are horns where some corrugations have been completely removed from the horn (e.g. if they are damaged at launch). As for filling the corrugations, corrugations were removed at different locations along the horn and the number of corrugations required to affect the beam pattern determined.

Similar to filling the corrugations, damaging the horn involved altering the horn's geometry file (Figure 5.26). The difference being that the inner radii of the corrugations were increased to almost the same size of the outer radii. This created one long section with small corrugations.

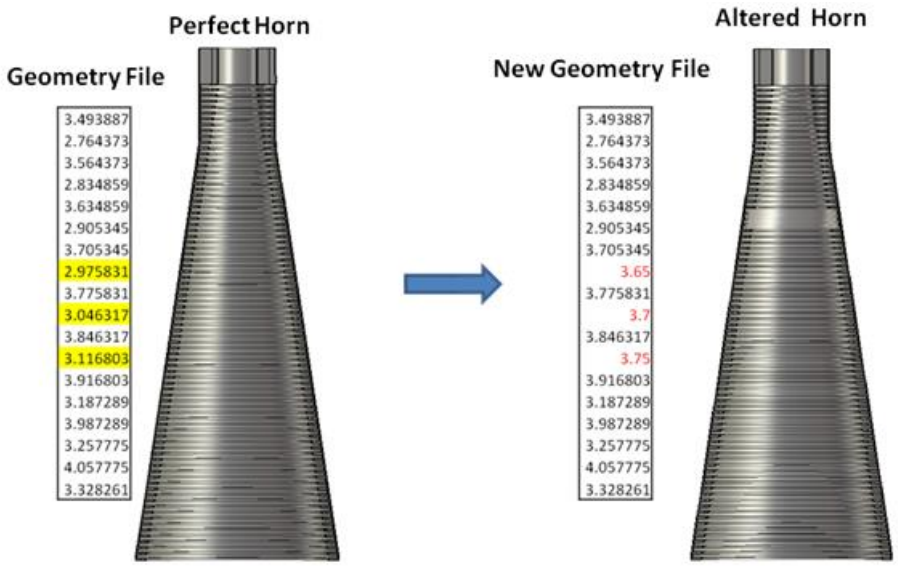

Figure 5.19 Three corrugations being removed by altering the geometry file.

The results shown in Figures 5.20 and 5.21 show that removing a single corrugation does have an effect but just like filling the corrugations this effect depends on the location. The co-polar results (Figure 5.20) show that removing a corrugation at position 1 has no effect on beam symmetry and sidelobe levels. At position 4 there is a small effect on the width of the main beam but the beam is symmetric and the sidelobes are low. Removing corrugations at position 2 shows the beam pattern losing symmetry and an increase in sidelobe level. At positions 3 and 5 there is a loss in beam symmetry and an increase in sidelobe level. The cross-polar results (Figure 5.21) show that filling at position 1 produces no effect, positions 2, 3 and 5 produce the highest cross-polarization, position 4 produces a small increase in cross-polarization level.

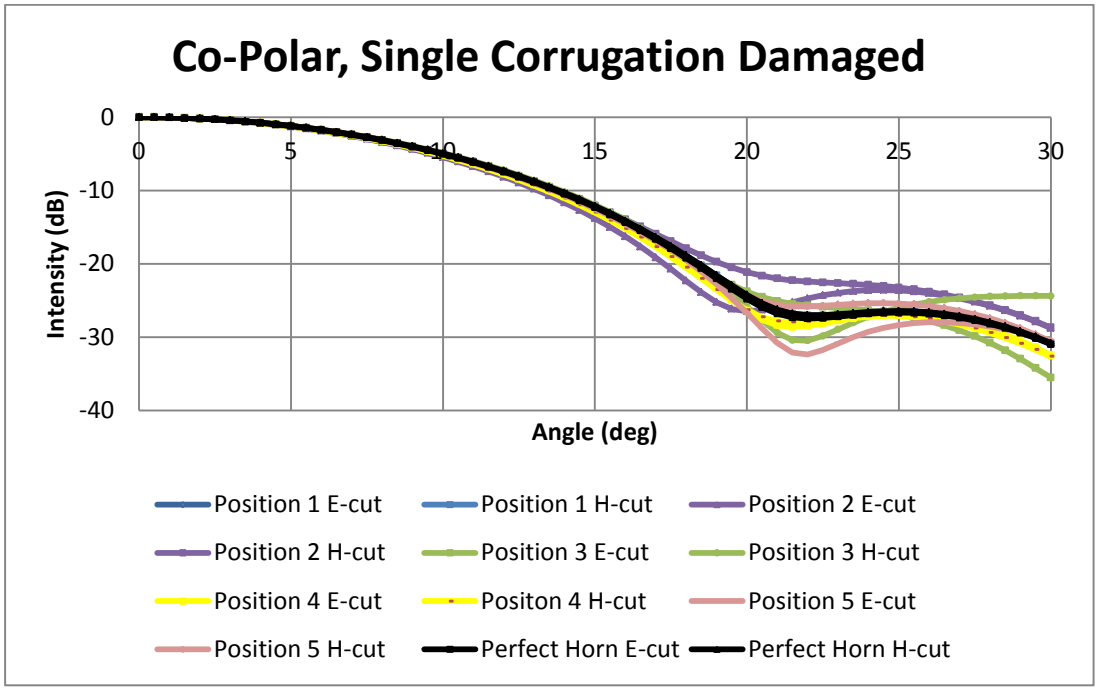

Figure 5.20 Co-polar power as a function of off-axis angle for a corrugated horn which has had one corrugation removed. The position of the removed corrugation is given by the colour (see Figure 5.5). A horn without any removed corrugations was plotted for comparison (in black).

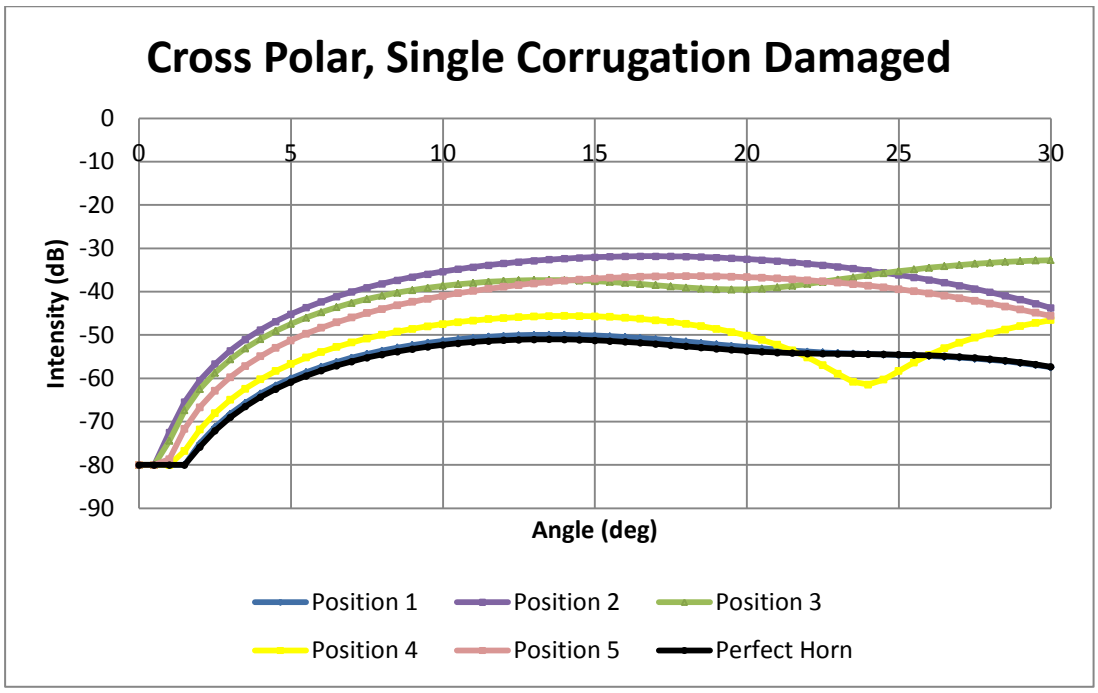

Figure 5.21 Cross-polar power as a function of off-axis angle for a corrugated horn which has had one corrugation removed. The position of the removed corrugation is given by colour (see Figure 5.5). A horn without any removed corrugations was plotted for comparison (in black).

The co-polar results for removing two corrugations (Figure 5.22) show that removing corrugations at position 5 and 3 has greater effects on beam symmetry and sidelobe levels than position 2 which was not the case for filling the corrugations. Once again there is no change at position 1. At position 4 there is a small increase in sidelobe level and the beam is no longer symmetric. Removing two corrugations increases the levels of cross-polarization (Figure 5.23). Position 3 causes the greatest effect, peaking at -25 dB which is 25 dB higher than the cross-polar level of a perfect horn.

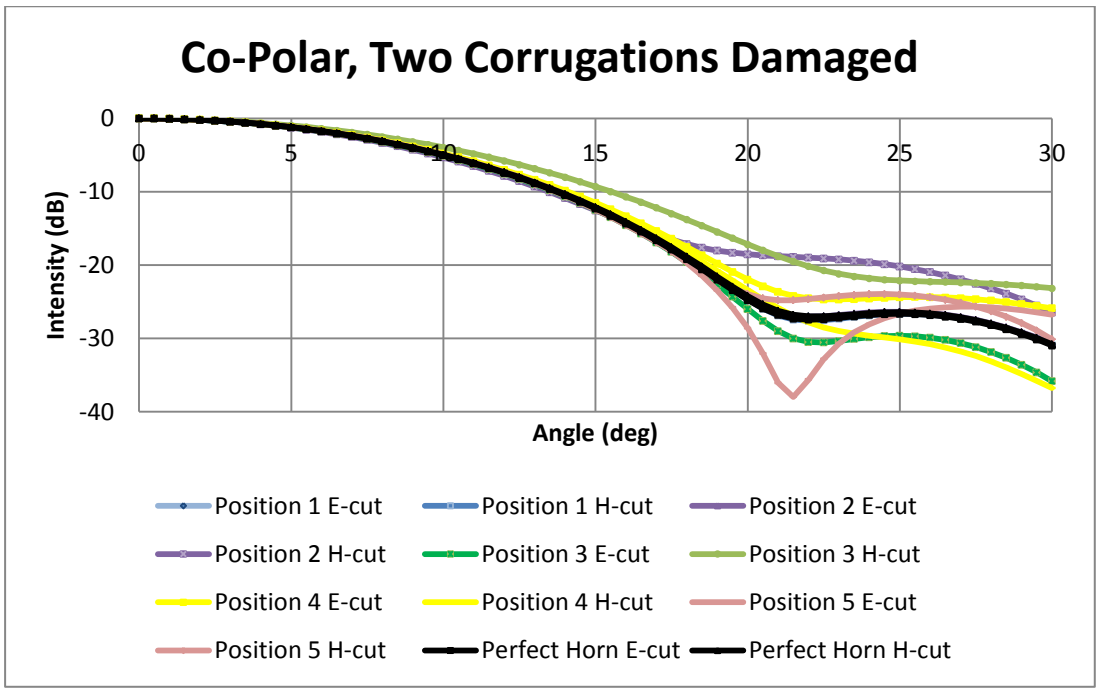

Figure 5.22 Co-polar power as a function of off-axis angle for a corrugated horn which has had two corrugations removed. The position of the removed corrugations is given by the colour (see Figure 5.5). A horn without any removed corrugations was plotted for comparison (in black).

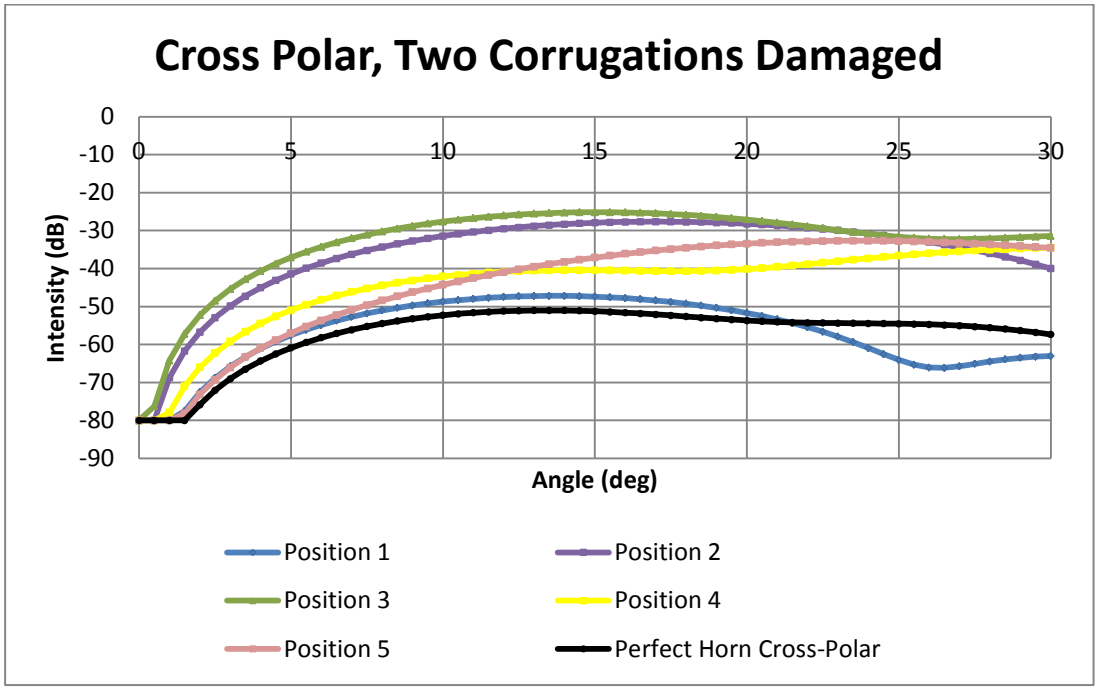

Figure 5.23 Cross-polar power as a function of off-axis angle for a corrugated horn which has had two corrugations removed. The position of the removed corrugations are given by colour (see Figure 5.5). A horn without any removed corrugations was plotted for comparison (in black).

Removing three corrugations at any position produces a beam pattern that is again no longer symmetric and in general has increased sidelobe levels (Figure 5.24). Positions 2 and 3 causes the greatest effect. Position 4 shows an almost symmetrical beam but with higher sidelobes. Position 5 has improved in comparison to removing two corrugations, the beam pattern is more symmetric and the sidelobe levels have almost returned to normal. Position 1 even shows a decrease in sidelobe level. The levels of cross-polarization (Figure 5.25) have increased. The cross-polar levels at positions 2 and 3 remain the highest, but the level at position 1 has increased drastically in comparison to removing one or two corrugations, while the level at position 5 decreased in comparison to removing one or two corrugations.

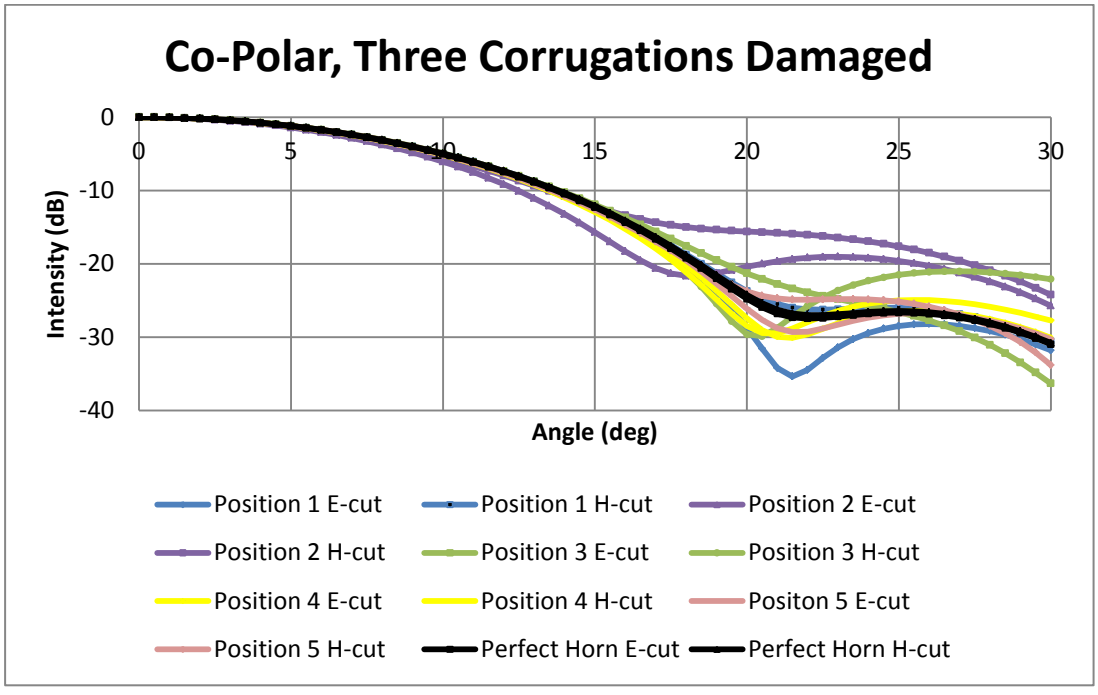

Figure 5.24 Co-polar power as a function of off-axis angle for a corrugated horn which has had three corrugations removed. The position of the removed corrugations is given by the colour (see Figure 5.5). A horn without any removed corrugations was plotted for comparison (in black).

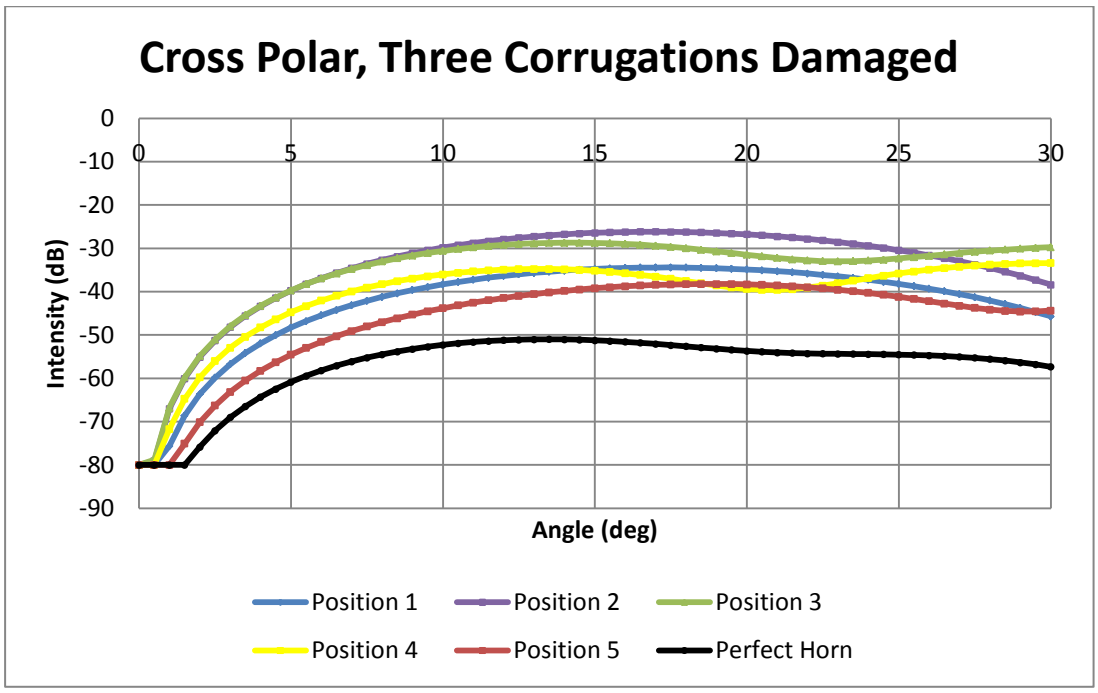

Figure 5.25 Cross-polar power as a function of off-axis angle for a corrugated horn which has had three corrugation removed. The position of the removed corrugations is given by colour (see Figure 5.5). A horn without any removed corrugations was plotted for comparison (in black).

Similar to filling the corrugations the more corrugations removed the greater the effect on beam symmetry, sidelobe levels and cross-polarization level. In general the location of the removed corrugations is important. The level of the effect seen with number of corrugations removed is shown in Figures 5.26 and 5.27. The locations that cause the most effect are positions 2, 3, and in the case of removing two corrugations position 5. Removing three corrugations causes the beam pattern to lose its symmetry, causes higher side-lobes and cross-polarization. Once again to confirm the accuracy of these results from Scatter they were compared to the results obtained using CST. The comparison is shown in Figure 5.28, and once again there is good agreement between the two methods.

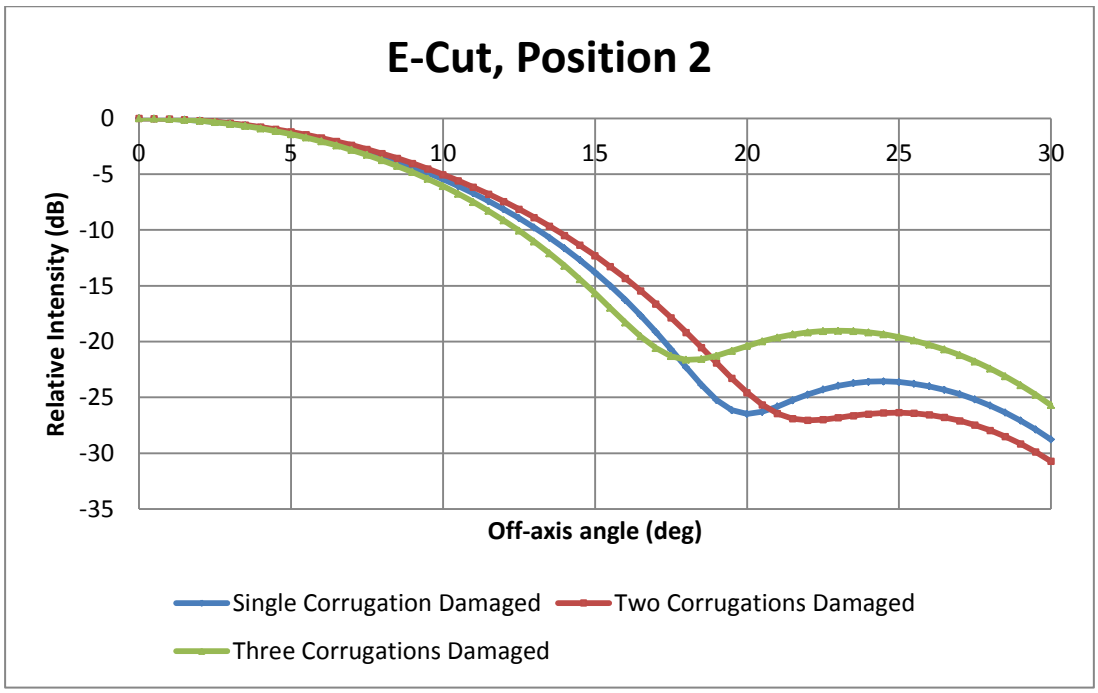

Figure 5.26 Beam pattern (E-cut) for different number of corrugations removed at position 2.

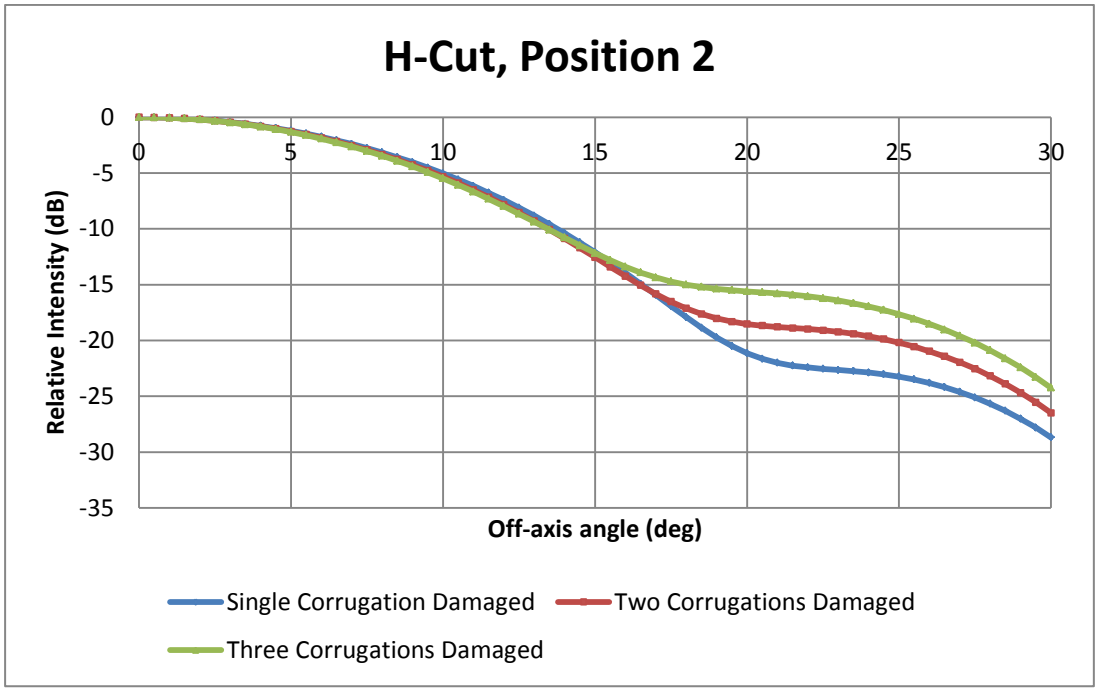

Figure 5.27 Beam pattern (H-cut) for different number of corrugations removed at position 2.

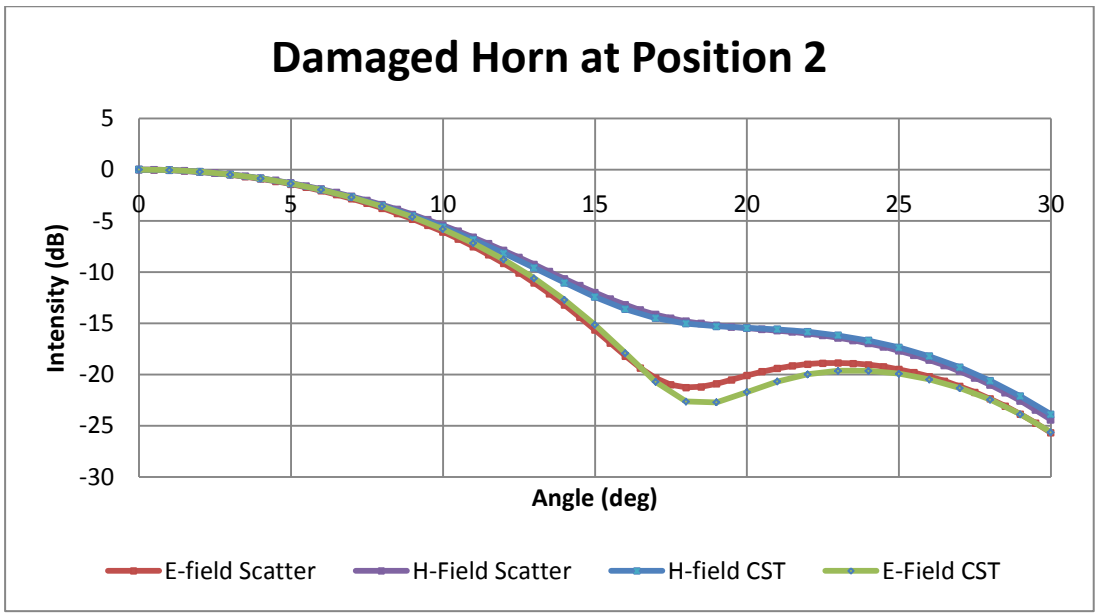

Figure 5.28 E and H plane cuts of the beam pattern from a corrugated horn with three corrugations removed at position 2 (see Figure 5.5). The beam patterns were calculated using Scatter and CST.

The effects of damaging three corrugations at position 2 were then measured at different frequencies across the bandwidth (85, 90, 95, 105, 110 and 115 GHz)(Figures 5.29 to 5.31). The individual results for each frequency are given in Appendix B.

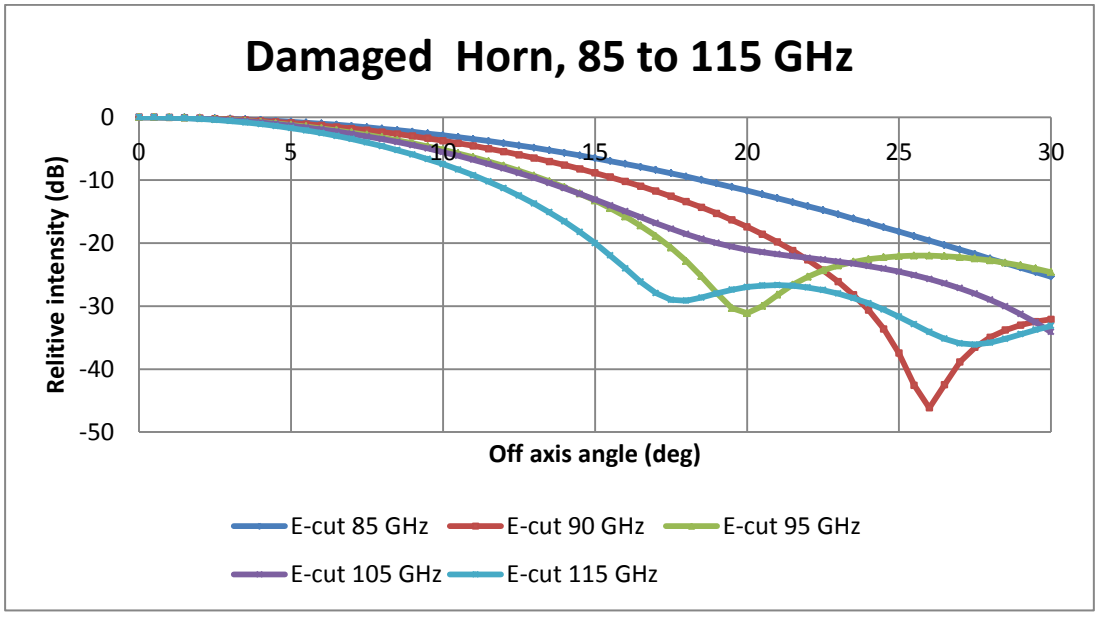

Figure 5.29 The co-polar (E-cut) results for damaging three corrugations at position 2, operating between 85 GHz and 115 GHz

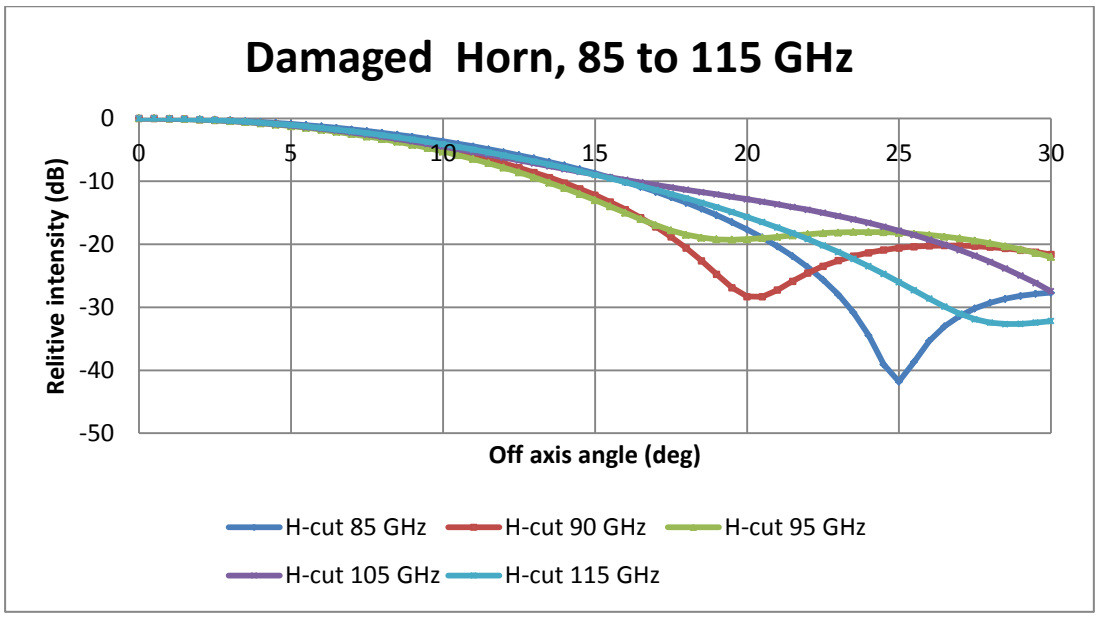

Figure 5.30 The co-polar (H-cut) results for damaging three corrugations at position 2, operating between 85 GHz and 115 GHz

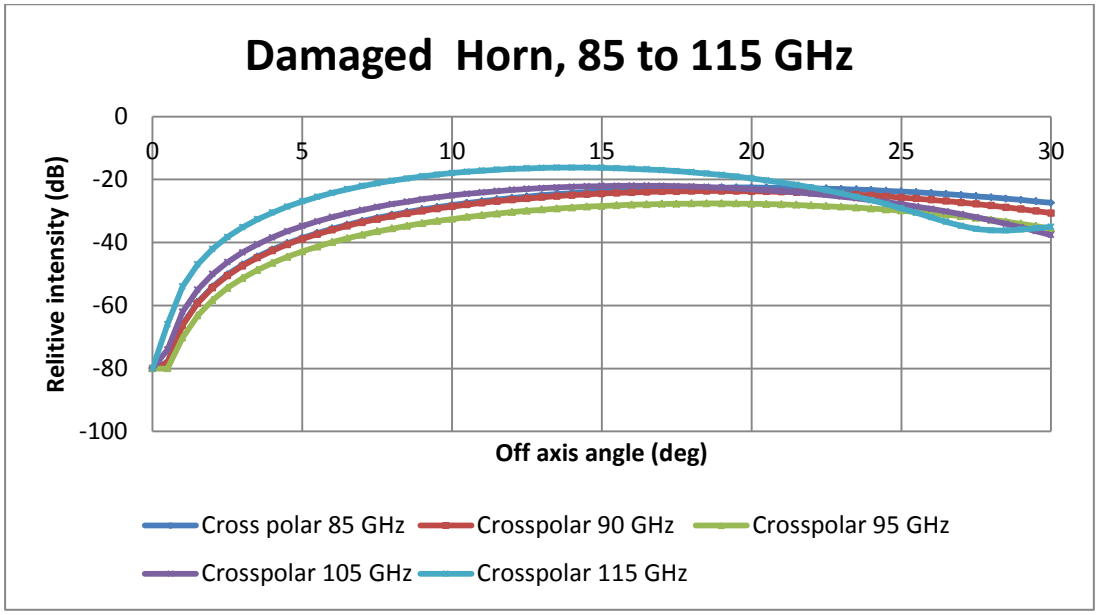

Figure 5.31 The cross-polar results for damaging three corrugations at position 2, operating between 85 GHz and 115 GHz

Unlike the results obtained when filling the corrugations, the results (Figures 5.29-5.31) for removing the corrugations show that as the frequency moves further away from 100 GHz the effects on beam symmetry and cross-polarization levels increase. The co-polar results at 85 and 90 GHz show a

significant difference between the E- and H-cuts, the beam is asymmetric at an off-axis angle of 10 degrees or more. At 95 GHz the beam pattern is the most symmetric the biggest difference between the E- and H-cuts is 10 dB. At 105 and 115 GHz the results show a small difference between the E- and H-cuts, the E-cuts are almost at the same level of the beam pattern produced by a perfect horn.

The cross-polar results also show that the lower the frequency the lesser the effect on the cross-polar levels. At 85 GHz the cross-polarization level peaks at -22 dB an increase of 30 dB from a perfect horn. Increasing the frequency shows a decrease in the cross-polar levels and the lowest level was at 95 GHz peaking at -29 dB, an increase of 15 dB.

5.4.3 Comparison between Filled and Damaged Horn

The results show that damaging or filling even a single corrugation can have an effect on the horn's performance in terms of beam width, main beam symmetry, sidelobe level and cross-polarization level. Both damaging and filling the corrugations are bad for the horns but which is worse, damaging or filling? Figures 5.32-5.34 shows a comparison between a damaged horn and a filled horn. Since filling and removing three corrugations at position 2 showed the most effect those results were chosen for the comparison.

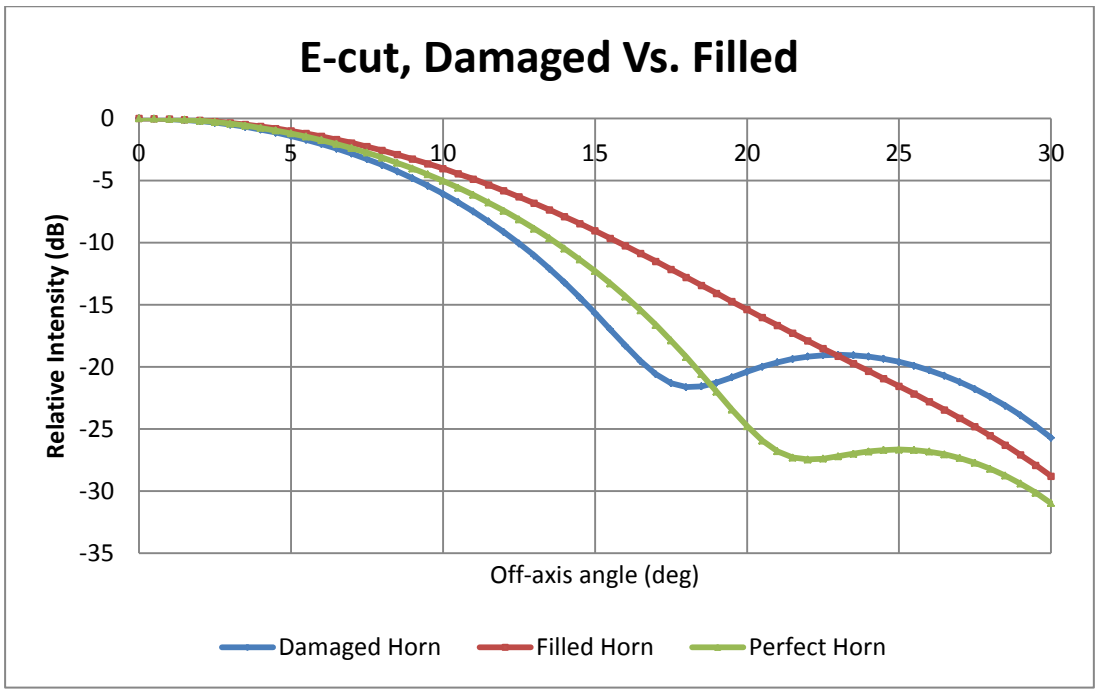

Figure 5.32 Co-polar power as a function of off-axis angle for a corrugated horn which has had three corrugations removed/filled at position 2 (E-cut only). A horn without any removed/filled corrugations was plotted for comparison.

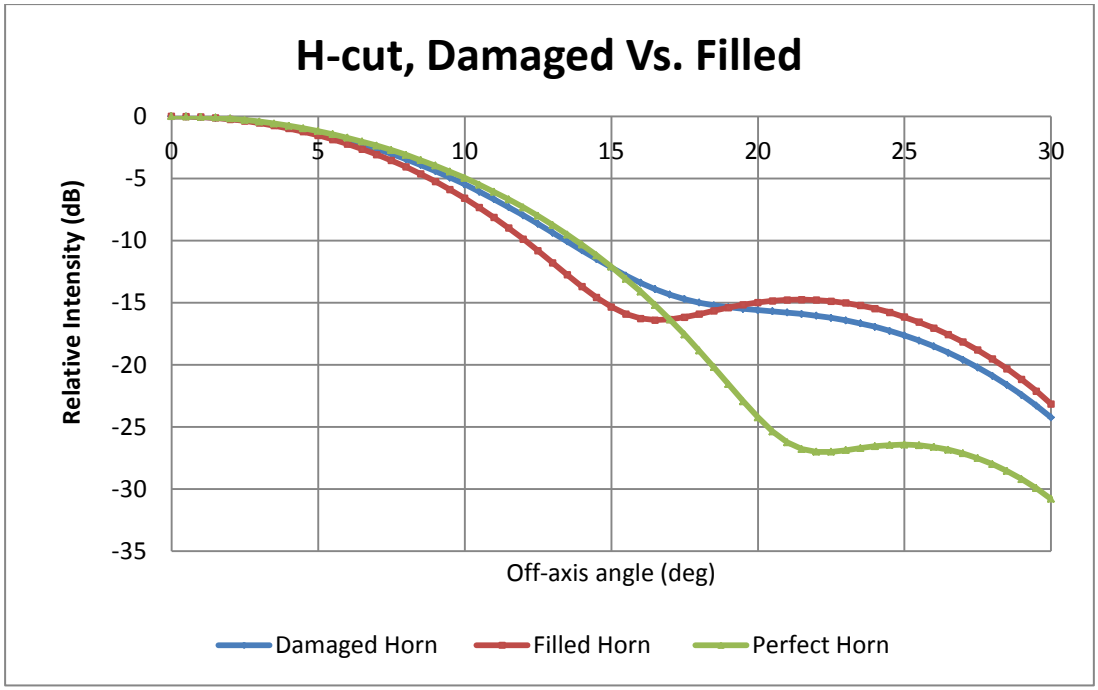

Figure 5.33 Co-polar power as a function of off-axis angle for a corrugated horn which has had three corrugations removed/filled at position 2 (H-cut only). A horn without any removed/filled corrugations was plotted for comparison.

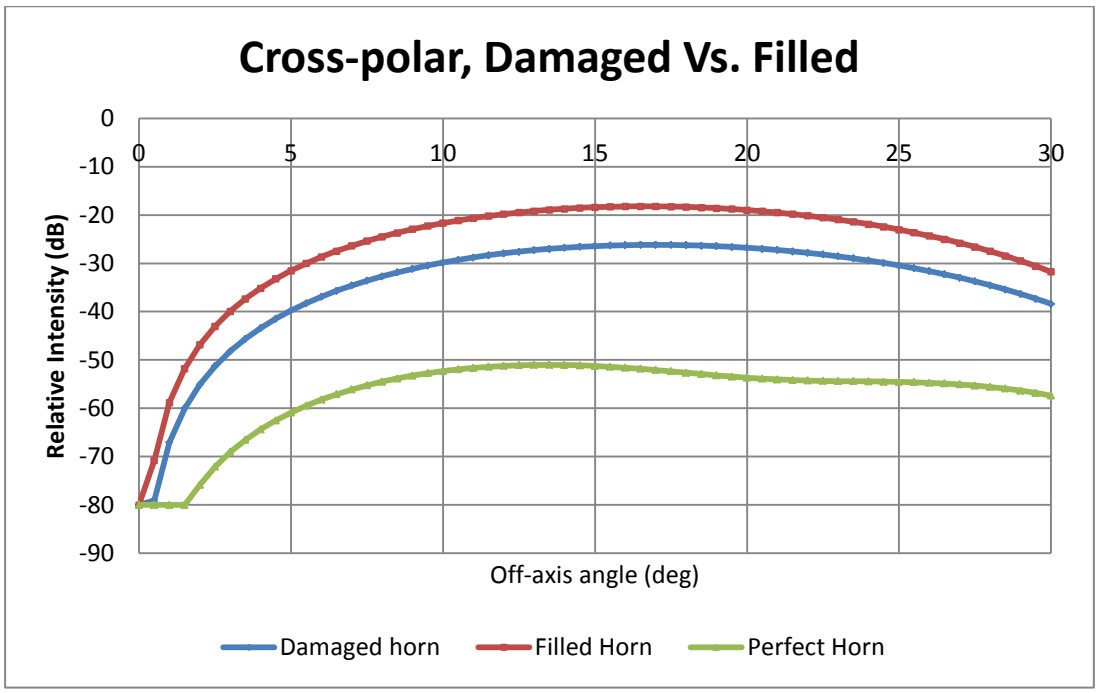

Figure 5.34 Cross-polar power as a function of off-axis angle for a corrugated horn which has had three corrugations removed/filled at position 2. A horn without any removed/filled corrugations was plotted for comparison.

The comparison between damaging and filling corrugations show that filling the corrugations has more of an effect on beam width, beam symmetry, sidelobe level and cross-polarization.

5.4.4 Partially Filled Corrugated Horn

Next it was decided to investigate the effect of partially filling a corrugation i.e. not completely filling the full ring. This scenario is more likely to happen since it involves very small pieces of the mandrel being left in the horn which could be missed when inspecting the horn. With previous results in mind, this scenario was only tested for three corrugations at position 2. This scenario could only be tested using CST because Scatter will only work with cylindrically symmetric corrugations. To partially fill the corrugations a CAD model of a ring, with the same dimensions as the corrugation to be filled, was generated in CST. Then two blocks were created and intersected the ring. The blocks were then cut

away from the ring along with four pieces of the ring. The remaining pieces of the ring were then transformed into the corrugations of the horn. The process is illustrated in Figure 5.35. Three corrugations were filled by 10%, 20%, 30% and 40% at position 2 (see Figure 5.5). The reason for having four pieces filling the corrugations was to make the model symmetric and hence allowing for the use of the boundary conditions in CST (discussed in Chapter 2).(effectively modelling a quarter of the horn).

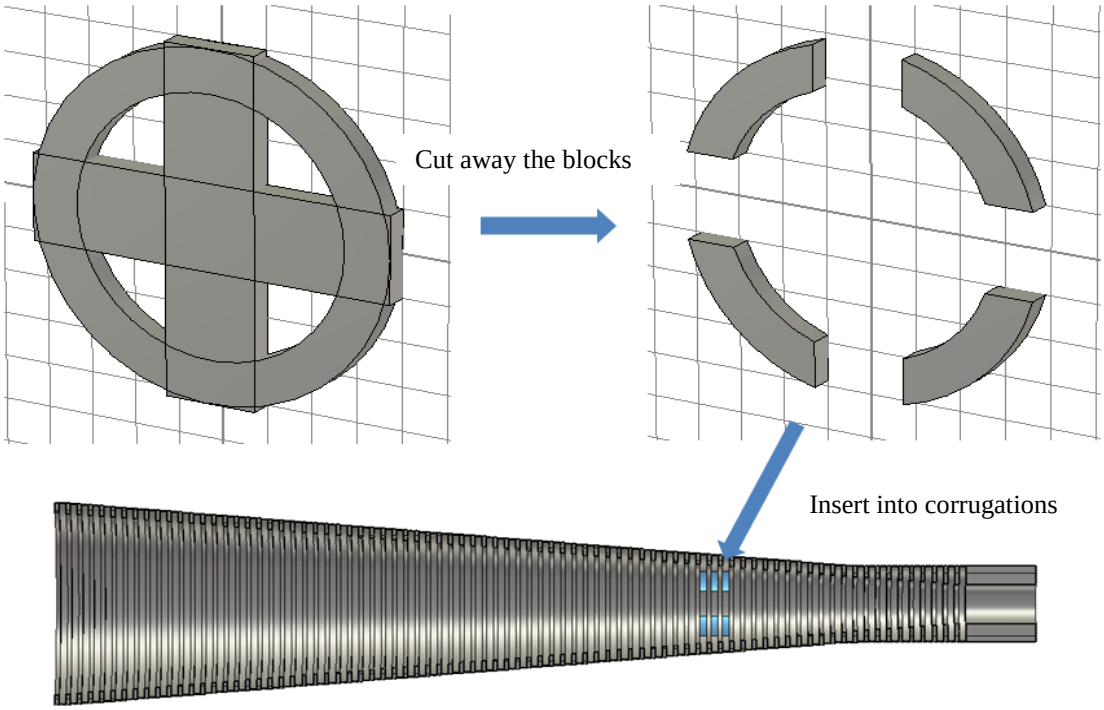

Figure 5.35 A CAD model of a ring, with the same dimensions as the corrugations to be filled, being intersected by two blocks which are then cut away leaving pieces of the ring. These pieces are then inserted into a corrugation to partially fill it.

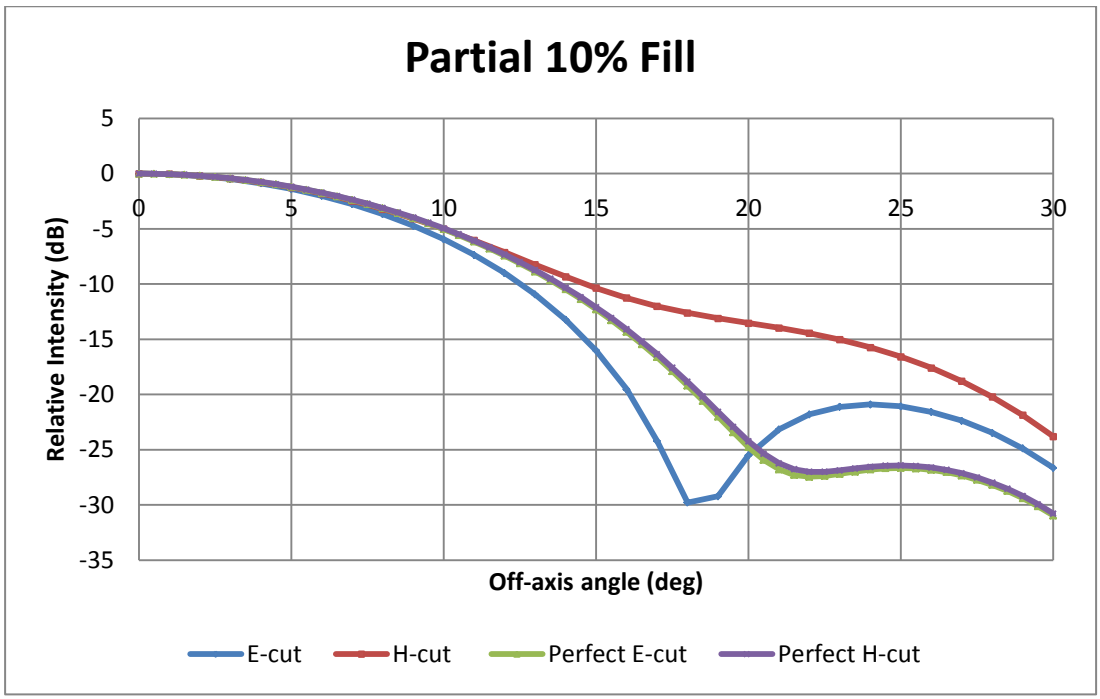

Figure 5.36 Co-polar power as a function of off-axis angle for a corrugated horn which has had three corrugations partially filled by 10%. The filled corrugations are at position 2 of the horn (see Figure 5.5). A horn without any partially filled corrugations was plotted for comparison.

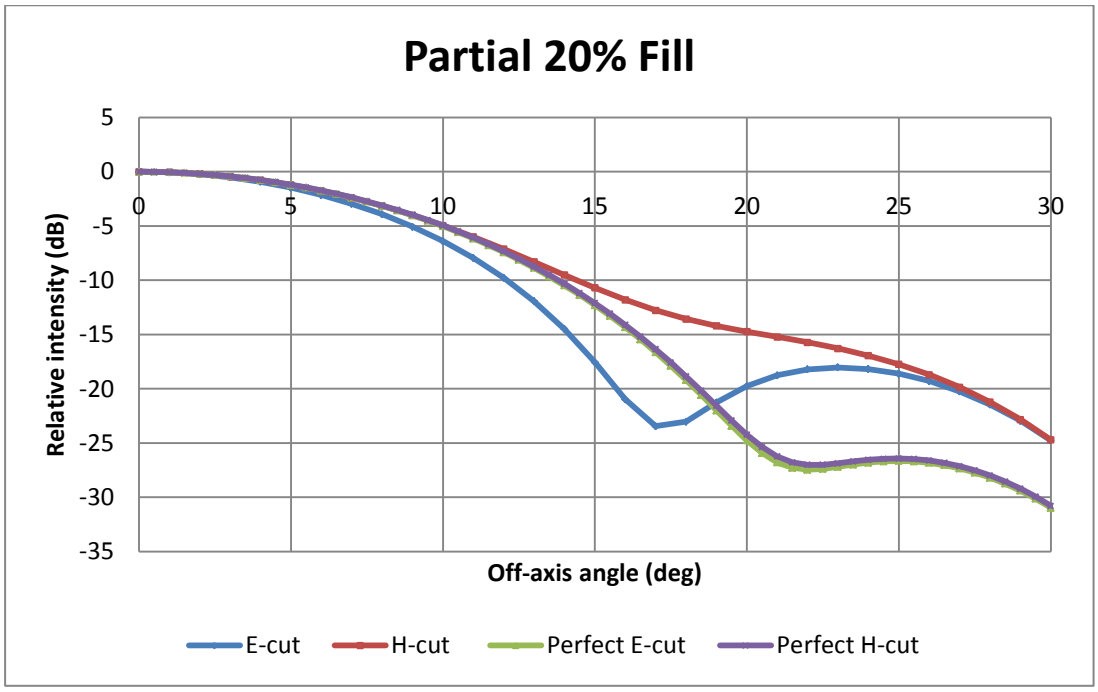

Figure 5.37 Co-polar power as a function of off-axis angle for a corrugated horn which has had three corrugations partially filled by 20%. The filled corrugations are at position 2 of the horn (see Figure 5.5). A horn without any partially filled corrugations was plotted for comparison.

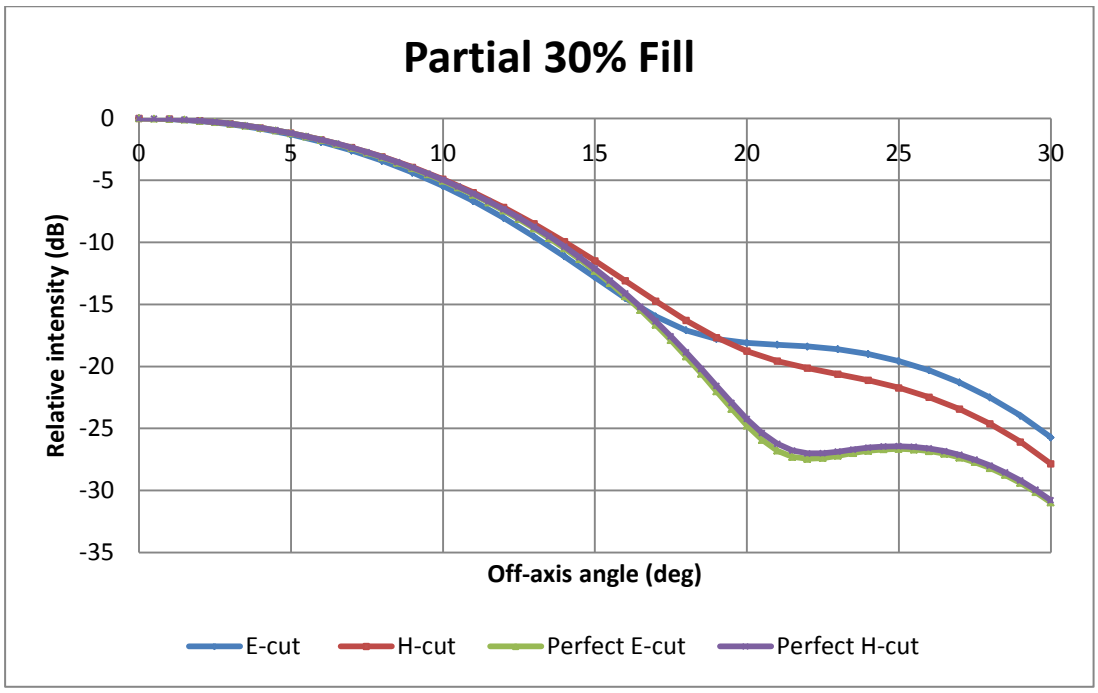

Figure 5.38 Co-polar power as a function of off-axis angle for a corrugated horn which has had three corrugations partially filled by 30%. The filled corrugations are at position 2 of the horn (see Figure 5.5). A horn without any partially filled corrugations was plotted for comparison.

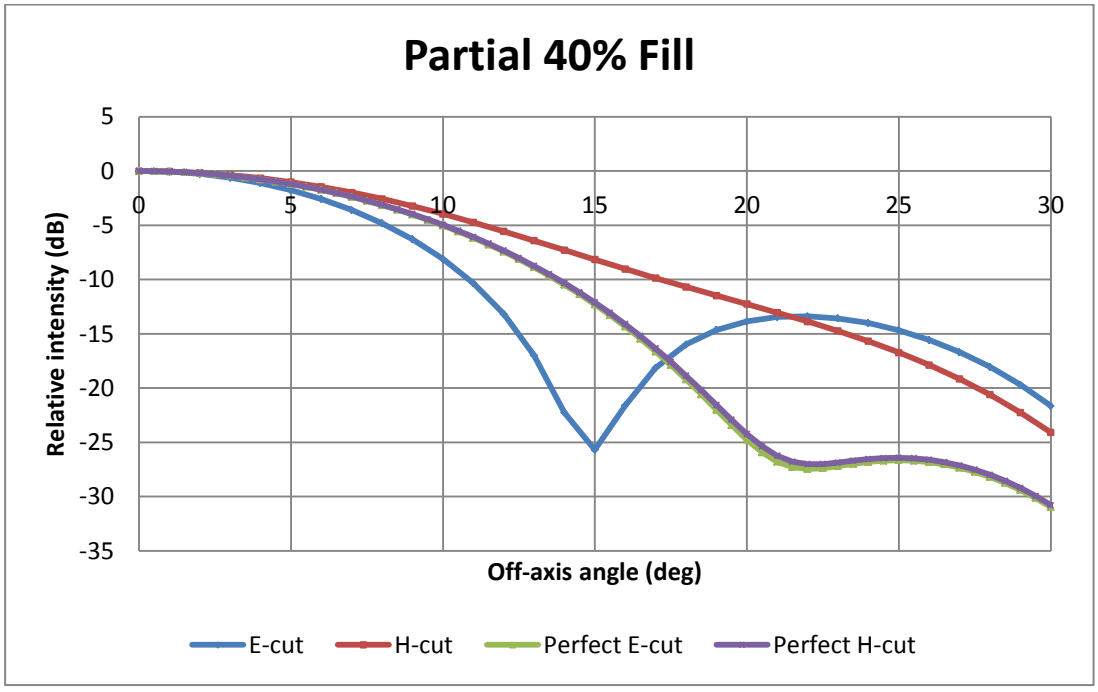

Figure 5.39 Co-polar power as a function of off-axis angle for a corrugated horn which has had three corrugations partially filled by 40%. The filled corrugations are at position 2 of the horn (see Figure 5.5). A horn without any partially filled corrugations was plotted for comparison.

The results (Figures 5.36 - 5.39) show that even filling the corrugations by 10% has an effect on the beam pattern. Filling the corrugations by 40% affected the beam the most which was an expected result. The results show that for 30% fill the beam pattern is more symmetric and has lower side-lobe levels than that of 10% and 20% which was not expected.

5.4.5 Partially Damaged Corrugated Horn

In this section I've investigated the effects of partially damaging the corrugations of the horn. The process of partially damaging the horns is similar to partially filling. The only difference being that the pieces of the ring, made of different material to the horn, intersect the corrugations and are then cut away creating an incomplete corrugation. Like the analysis of partially filling the corrugations, three corrugations are 10%, 20%, 30% and 40% partially removed at location 2. Once again this scenario could only be analysed using CST.

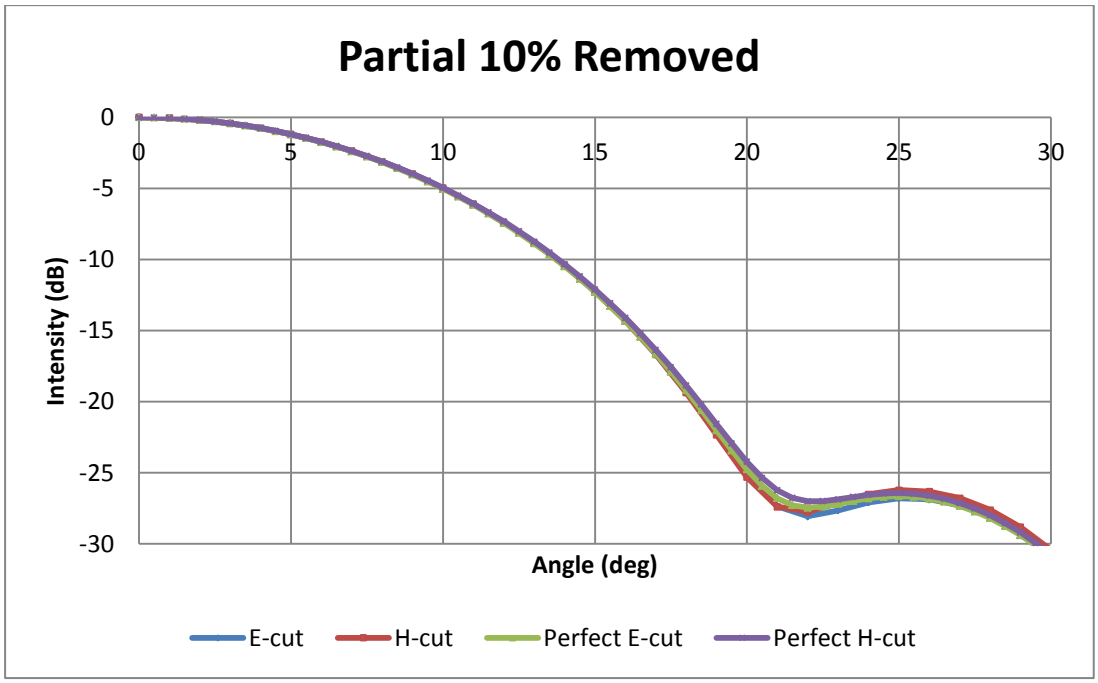

Figure 5.40 Co-polar power as a function of off-axis angle for a corrugated horn which has had three corrugations partially removed by 10%. The filled corrugations are at position 2 of the horn (see Figure 5.5). A horn without any partially removed corrugations was plotted for comparison.

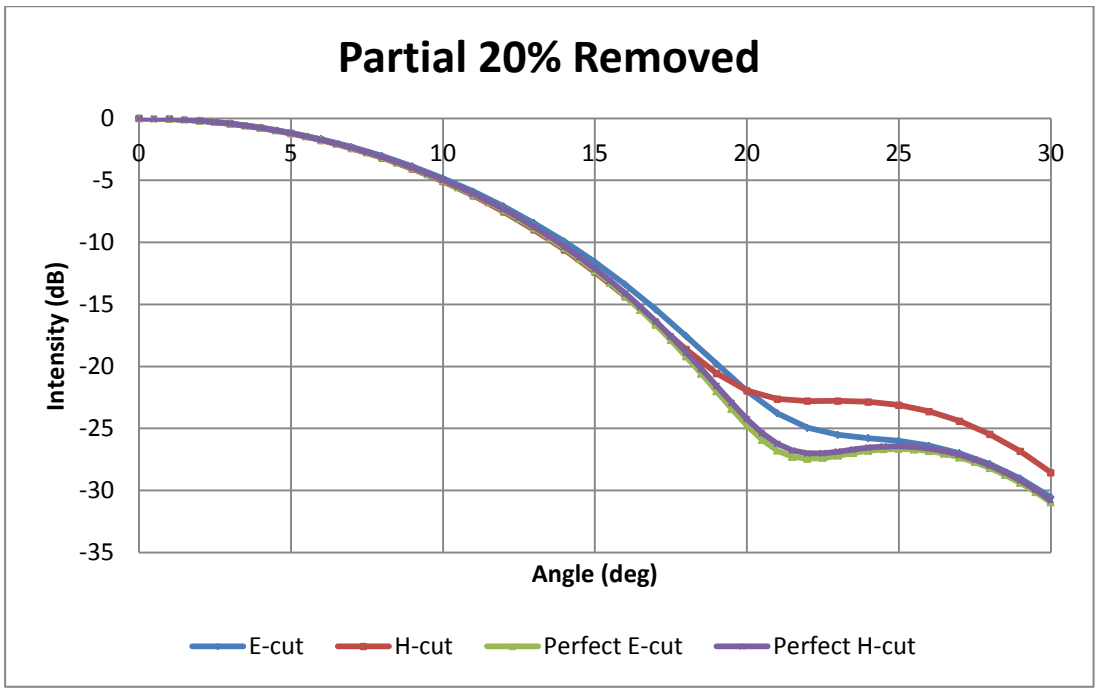

Figure 5.41 Co-polar power as a function of off-axis angle for a corrugated horn which has had three corrugations partially removed by 20%. The filled corrugations are at position 2 of the horn (see Figure 5.5). A horn without any partially removed corrugations was plotted for comparison.

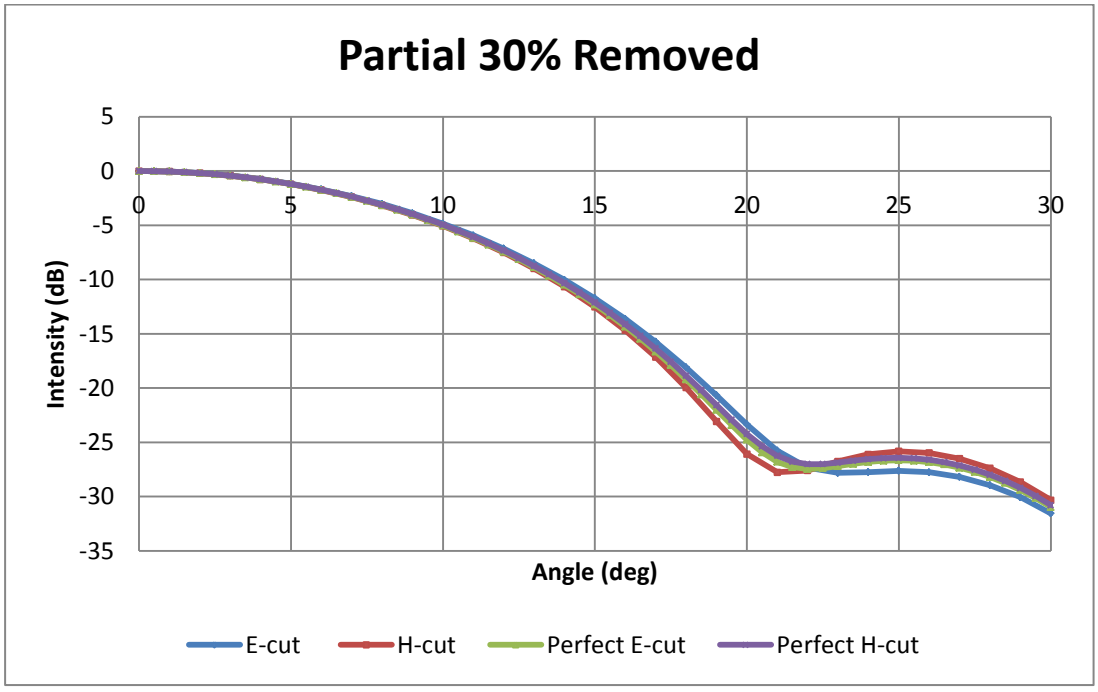

Figure 5.42 Co-polar power as a function of off-axis angle for a corrugated horn which has had three corrugations partially removed by 30%. The filled corrugations are at position 2 of the horn (see Figure 5.5). A horn without any partially removed corrugations was plotted for comparison.

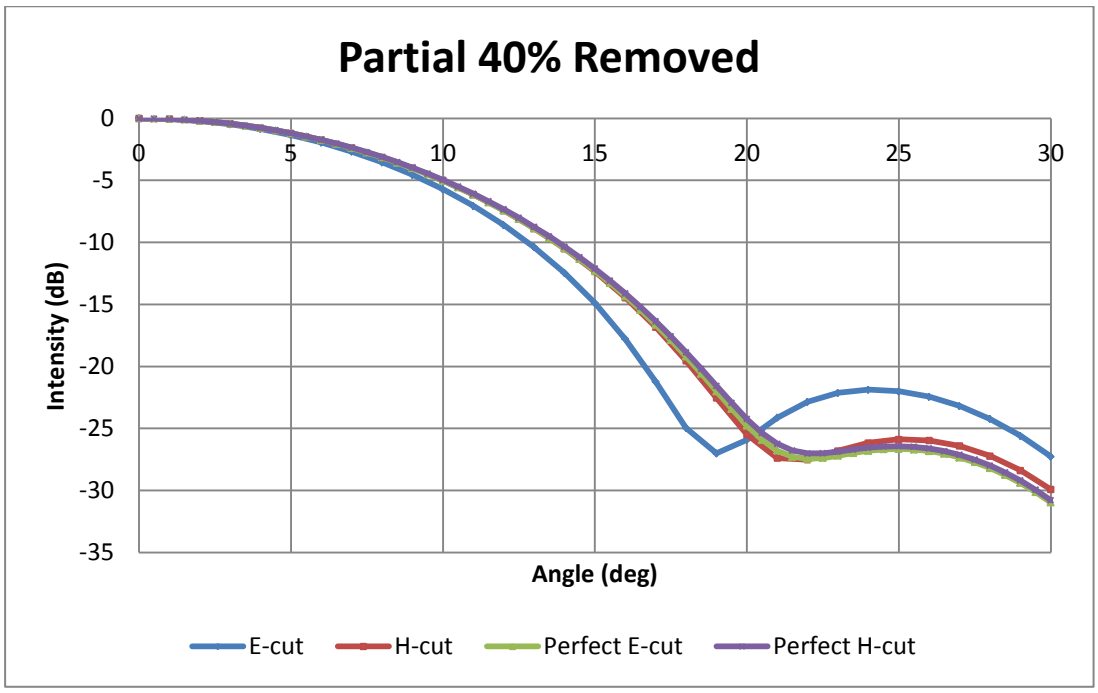

Figure 5.43 Co-polar power as a function of off-axis angle for a corrugated horn which has had three corrugations partially removed by 40%. The filled corrugations are at position 2 of the horn (see Figure 5.5). A horn without any partially removed corrugations was plotted for comparison.

The results (Figure 5.40-5.43) show that partially removing the corrugations has less of an effect than partially filling the corrugations. It was only when 40% of the corrugations were removed that we saw any significant effect beam symmetry and sidelobe level. However, at 20% removed there was an unexpected difference in sidelobe levels.

5.5 Summary

In this chapter I've discussed the use of electroformed corrugated horns, the type of horns used in the Planck telescope. Since Planck has oversized mirrors the beam shape on the sky is determined by the horns. There were some unexpected features on the Planck map that may have been caused by manufacturing tolerances. It was for this reason that the manufacturing tolerances of the horns were investigated in this chapter. Of particular interest are variations in the horns

that would be difficult to detect by visual exspection, which do not cause significant changes in the main beam (which can be checked with low frequency measurements before launch) and yet cause an increase in sidelobe level. The possible manufacturing tolerances for corrugated horns are damage to the corrugations or filling of the corrugations. I've calculated beam patterns and cross-polarization levels of horns with these manufacturing variations. The first manufacturing tolerance investigated was filling corrugations (simulating material being left in the corrugations after the electroforming process), then removing the corrugations (simulating the corrugations being damaged during launch) and these two scenarios were compared with one another to determine which was worse. The results were calculated using Scatter, and CST was used to confirm the accuracy of the results. Scatter was faster than CST. Then the scenario of partially filling and removing of corrugations was then investigated. Scatter was unable to simulate these scenarios since it requires cylindrically symmetrical corrugations and so only CST could be used.

It was found that filling corrugations had the greatest effect, reducing the symmetry of the main beam and increased the sidelobe level. The effect is particularly severe when three corrugations or more are filled, but even partially filling corrugations or filling even one corrugation had a noticeable effect, depending on the location of that corrugation. Damaging or partially damaging a corrugation also degrades the beam. My results show that even small defects (within manufacturing tolerances) could affect the sidelobe levels of corrugated horns, something that may explain features seen on the recently published Planck CMB maps.

Chapter 6 Conclusions

6.1 Conclusion

This thesis was concerned with the analysis of quasi-optical systems for long-wavelength applications in the terahertz and submillimetre wavebands. The astronomical instrumentation used in the CMB telescopes QUBIC and Planck were the main focus of my work.

In Chapter 1 of this thesis the CMB was introduced and the importance and difficulty of making accurate measurements of its temperature and polarization fluctuations were highlighted. I then focused on the instruments used in the CMB experiments such as bolometric and heterodyne receivers. A list of experiments dedicated to measuring the CMB showed the importance now given to these measurements.

In Chapter 2 the properties of waveguides and corrugated horns that are used in CMB experiment receivers were examined. Also outlined in this chapter was the derivation of the forms of the TE and TM modes that propagate through them. The techniques exploited by the CST and Scatter software that were used to carry out a detailed analysis of the horn feeds used in these instruments were also described in this chapter.

In Chapter 3 the improvements made to the mode-matching software Scatter was discussed. Scatter was found to be producing unexpected results for Planck at certain frequencies. The possible reason for this was the numerical instability in the matrix inversion technique. A solution to this was to replace the inverse matrix with a pseudoinverse matrix. This was done by Ian McAuley for the Scatter code in the MATLAB and Mathematica environment. In this chapter I discussed and

implemented changes to Scatter in the C (NI LabWindows) environment. It was found that changing the code to use the pseudoinverse, rather than the inverse of a matrix, improved the beam predictions for the Planck horn and for the QUBIC horn when gaps were introduced between the platelets.

In Chapter 4 I looked at the possible manufacturing issues that can arise when dealing with platelet formed corrugated horns, the type of horns that will be used as the sky horns for the QUBIC telescope. Manufacturing issues such as adding a thick plate in front for stability, effects of adding gaps between the plates and manufacturing tolerances when cutting platelet holes were investigated.

The investigation into adding a thick plate for stability showed good agreement between the simulated results and the measured results. The two scenarios under test were a 100 GHz corrugated conical horn, with a smooth thick plate, and a horn with a corrugated thick plate. Both CST and Scatter were used to simulate these scenarios. The results show that there is a small narrowing of the beam and the slight elevation in the sidelobe levels for both a smooth and corrugated thick plate. They also show that both scenarios produce almost the same effect on the beam pattern. The measurements taken by the VNA agree with the conclusions from the simulations. I concluded that a thick plate has a small effect on the beam pattern and that it doesn't matter if the plate is smooth or corrugated. A smooth thick plate is ideal, as it is easier to manufacture as it doesn't require etching corrugations into the plate.

Testing the effects of gaps between the platelets was done using Scatter. The results show that as the gap sizes increased the effect on the beam pattern and sidelobe levels also increased. The size of the gaps ranged from 0.003 mm ($\lambda/666.6$) to 0.3 mm ($\lambda/6.6$). The results show that a gap size of 0.1 mm ($\lambda/20$)

starts to affect the sidelobe levels and at 0.15 mm (λ/13) the sidelobe levels would be too high to make useful scientific measurements. CST was also used to investigate the effects but the results were not sufficiently accurate. With the gap sizes being as small as $\lambda/10^3$ and with the horn operating at such a high frequency, the sampling rate of CST needed to be higher than λ/12 which was not possible with the computer available. I conclude that for gaps between the plates to have a significant effect on the horn's performance, the size of the gaps would need to be greater than λ/20 which is well outside realistic manufacturing tolerances.

When investigating the addition of random variations to the corrugation radii it was determined from the results that the larger the variation added the greater the effect on the main beam and sidelobes, as expected. It can be seen from the results that the intensity of the main beam pattern starts to get affected by adding a variation between ±0.2 mm (λ/15), adding variations between ±0.25 mm (λ/12) causes the intensity of the main beam lobe greatly decreased. Therefore this corrugated horn can tolerate a variation in the radii between ±0.15 mm before the any effects on the main beam pattern can be seen.

In Chapter 5 the effects of manufacturing tolerances of electroformed corrugated horns, the type of horns used in the Planck telescope, were modelled. The effects of filling and removing corrugations were investigated using CST and Scatter. The Planck horns were too large to simulate on CST so a smaller 100 GHz conical corrugated horn was used instead. The results show that damaging or filling even a single corrugation can have an effect on a corrugated horn's beam pattern in terms of beam width, main beam symmetry, sidelobe level and cross-polarization. The level of the effect depends on the position of the removed/filled corrugations but in general the effect gets particularly bad for three corrugations

removed/filled. The neck of the horn is the least affected by the filling and removal of corrugations. Damaging or filling the corrugations at the throat and the centre of the horn is where we see the greatest effect on the beam pattern. The main beam loses its symmetry, there is an increase in side lobe level and cross-polarization. Other locations along the horn were shown to have some effect on the beam symmetry but the levels of the side-lobes were the most affected.

The effects of filling or removing the corrugations was investigated at a range of different frequencies. The results show that the effects on the beam pattern caused by filling the corrugations increased as the frequency increased. The results for removing the corrugations show that the effects on the beam pattern increased as the frequency moved further away from 100 GHz (the central operating frequency).

The two scenarios were then compared to one another to determine whether it was better to have a filled or a damaged horn. The results show that filling the corrugations was slightly more damaging to the horn's beam pattern and cross-polarization level.

The effects of partially filling and removing corrugations were then investigated. This could only be done using CST since Scatter requires cylindrically symmetric corrugations. The results from completely filling or removing corrugations show that three corrugations removed/filled at the throat of the horn affected the beam pattern the most, for this reason only three corrugations partially filled/removed at the throat were simulated to save on computational time. The results for partial fill show that even with 10% of the corrugations filled there was an effect on the beam pattern and sidelobe levels. The results showed that generally the greater the percentage of the corrugation

filled the greater the effect, with the one exception. At 30% fill the beam pattern was more symmetric and the sidelobe levels weren't as high as 10% and 20% fill. The results for partially damaged corrugations show that removing the same amount of material from the horn that had filled the corrugations, almost had no effect on the beam pattern and sidelobe level. It was only at 40% removal that a small difference was seen in the beam width and beam symmetry.

The analysis of the manufacturing tolerances showed the importance of the corrugations and how the complete removal or filling of even a single corrugation can have a significant effect on the horn's performance. Leaving some corrugations filled or partially filled after the manufacturing process has a bigger impact on performance than the corrugations being damaged during launch.

6.2 Author's Contribution

The theory presented in Chapters 1 and 2 are from the literature but I have selected topics that are of particular relevance for this work. These topics come from very different fields including observational cosmology (Chapter 1) and antenna modelling (Chapter 2). In Chapter 2 I also describe the operation of code (both commercial and in-house) later used by the author for simulations. There was a significant learning curve with these highly-specialised software and it took time to build up experience and intuition with the different techniques.

In Chapter 3 I describe additions to the Scatter code that were made by the author and these were applied to two cases. The first had been studied in a different environment by Ian McAuley of NUI Maynooth, the second arose only in the work of the author.

All the simulations in Chapters 4 and 5 were carried out by the author along with experimental measurements and design of the horn attachments. The attachments were manufactured by David Watson of NUI Maynooth.

Works Cited

[1] Beatty, K., "Big stars and dark horses: Herschel's first observations", The 'NewScientist' website, Sky and Telescope,2010.

[2] http://map.gsfc.nasa.gov/resources/featured_images.html.

[3] Alpher, R. A., Herman, R. C., "Early Work on the Big Bang Cosmology and the Cosmic Background Radiation", Proceedings of the American Philosophical Society, Vol. 119, No. 5, p. 325-348, 1975.

[4] Wilson, R. W., Penzias, A. A., "Isotropy of Cosmic Background Radiation at 4080 Megahertz", Science, Volume 156, Issue 3778, p. 1100-1101,1967.

[5] Bennett, C. L., Smoot, G. F., Janssen, M., Gulkis, S., Kogut, A., Hinshaw, G.,

"COBE Differential Maicrowave Radiometers - Calibration Techniques", Astrophysical Journal, Vol. 391, No. 2, p.466-482, 1992.

[6] Turner, M. S., "Cosmology: Going Beyond the Bang Bang", Physics World, Sept. 1996.

[7] Lineweaver, C. H., "What is the Universe Made Of? How Old Is It?", Astophysical Journal, 9911294, 1999.

[8] http://www.kavliprize.no.

[9] http://map.gsfc.nasa.gov/resources/cmbimages.html.

[10] http://www.astro.ucla.edu/~wright/CMB-DT.html.

[11] ESA and the Planck Collaboration, Ade P.A.R et al,"Planck 2013 Results.XVI.Cosmological Parameters", submitted to Astronomy & Astrophysics, 2013, arXiv:1303.507vl.

[12] Guth, A. H., "Inflationary Universe: A Possible Solution to the Horizon and Flatness Problems", Physical Review D, Vol. 23, Issue 2, p. 347-356, 1981.

[13] http://cosmology.berkeley.edu/~yuki/CMBpol/.

[14] Hu, W., White, M.," A CMB Polarization Primer ", New Astronomy 2, 1997,.p.325, Elsevier Science B.V.

[15] http://www-news.uchicago.edu/releases/photos/polarization/.

[16] The QUBIC collaboration, Battistelli E, et al,"QUBIC The QU Bolometric Interfeometer for Cosmology", Astropartical Physics, Vol 3419, p705-716, 2011.

[17] Benford, D.J., Allen, C.A., Kutyrev, A.S., Moseley, S.H., Shafer, R.A., Chervenak, J.A., Grossman, E.N., Irwin, K.D., Martinis, J.M., Reintsema, C.D.,"Superconducting Transition Edge Sensor Bolometer Arrays for Submillimeter Astronomy", Proceedings of the 11th International Symposium on Space Terahertz Technology , pp187 - 196, Ann Arbor, Michigan May 1-3, 2000.

[18]Liddle, A., Loveday, J., "The Oxford Companion to Cosmology", Oxford University Press, p.4, 2008.

[19] Peiponen, K.E, Zeitler, A. , Kuwata-Gonokami, M., " Terahertz Spectroscopy and Imaging", Springer Series in Optical Sciences, Volume 171, 2013.

[20] Mogenson, M., Jemec, G. B. E., "Diagnosis of Nonmelanome Skin Cancer/Keratinocyte Carinoma: A review of Diagnostic Accuracy of

Nonmelenoma Skin Cancer Diagnostic Tests and Technologies", Dermatological Surgery, Vol. 33, Issue 10, p. 1158-1174, 2007.

[21] www .dtic.mil.com & www.science photolibrary.com.

[22] Wang, Y., Zhang, L., Deng, C., Li, W., Zhong, H., Zhang, C., "Feature Extraction and Identification of Explosive Materials in Reflective Terahertz Spectroscopic Imaging System", Proceedings of 2008 International Conference on Optical Instuments and Technology: Microelectronic and Optoelectronic Devices and Integration, Vol. 7158, 2009.

[23] Luukanen, A., Gronholm, M., Lappalainen, P., Leivo, M., Rautiainen, A., Tamminen, A., Ale-Laurinaho, J., Dietlein, C.R., Grossman, E. N., "Real-Time Passive Terahertz Imaging System for Standoff Conceal Weapons Imaging ", Passive Millimeter-Wave Imaging Technology XIII Proceedings, SPIE Digital Library,Vol. 7670, 2010.

[24] http://dc126.4shared.com/doc/FQblY-rR/preview.html - CST Documentation Centre.

[25] Gleeson, E., "Single and Multi-moded Corrugated Horn Design for Cosmic Microwave Background Experiments", Ph.D. thesis, National University of Ireland, Maynooth, Ireland, 2004.

[26] Orfanidis S. J.," Electromagnetic Waves and Antennas", ECE Department,Rutgers University, chapter 9, p. 362 - 374, 2008.

[27]http://www.rfcafe.com/references/electrical/rectangular-waveguide-modes.htm.

[28] Swaminathan, M.,"Computation of cutoff wavenumbers of TE and TM modes in waveguides of arbitrary cross sections using a surface integral formulation ", IEEE Xplore Digital Library, p.154 - 159, Feb. 1990.

[29] http://www.globalspec.com/reference/59959/203279/7-10-circular-cylindric-waveguides.

[30] Pozar, D. M., "Microwave Engineering", Second Edition, John Wiley & Sons Inc., Toronto,1998.

[31] Olver, A.D, Clarricoats, P.J.B., Kishk, A.A., Shali, L., "Microwave Horns and Feeds", IEEE Press, New York, 1994.

[32] Weiland, T.,"A discretization model for the solution of Maxwell's equations for six-component fields", Archiv fuer Elektronik und Uebertragungstechnik, vol. 31, p. 116-120, 1977. In German.

[33] Doherty, S., "Optical and Quasi-Optical Design and Analysis of Astronomical Instrumentation including a Prototype SAFARI Pixel", Ph.D. thesis, National University of Ireland, Maynooth, Ireland, 2012.

[34]http://www.home.agilent.com/upload/cmc_upload/All/NSI-near-far.pdf?&cc=IE&lc=eng.

[35] Neiman, M. S., "The Principle of Reciprocity in Antenna Theory", Proceedings of the I.R.E, December, 1943.

[37] Press, Teukolsky, S.A., W.H, Vettering, W.T., and Flannery, B.P., Numerical Recipes in C, Cambridge University Press, 1992.

[38] Kenneth E. Dudeck, Solving complex systems using spreadsheets: a matrix decomposition approach, “Proceedings of the 2005 American Society for Engineering Education Annual Conference & Exposition”

[39] E. W. Wolff et al., Southern Ocean sea-ice extent, productivity and iron flux over the past eight glacial cycles, Nature 440, 491 (2006).

[40] Derby, B., Wallach, E. R., "Theoretical model for diffusion bonding", Metal Science, Volume 16, pp. 49-56(8), 1982 .

[41] Haas et al., Fabrication and performance of MMW and SMMW platelet horn arrays", Multi-feed Systems for Radio Telescopes ASP Conference Series, Vol. 75, 1995.

[42] Benford, D. J., Kooi, J. W., and Gaidis, M. C.,"Optical Properties of Zitex in the Infrared to Submillimeter", Applied Optics, 42(25):5118-5122, 2003.

[43]P. A. Ade, R.J. Wylde & J. Zhang, "Ultra-Gaussian horns for ClOVER-a B-mode CMB experiment", in proceedings 20th International Symposium on Space Terahertz Technology, charlott-esville 20-22 April 2009, pp128-137.

[44] McLoughlan, E., " Optimisation of a Near Field Scanning System", Master Thesis, NUI Maynooth, pg. 26, 2012.

[45] Tauber, J.A., "The Planck mission", Advances in Space Research Volume 34, Issue 3, 2004, pg. 491–496.

[46] Maffei, B., Noviello, F., et al., "Planck pre-launch status: HFI beam expectations from the optical optimisation of the focal plane", EDP Sciences, A&A 520, A12, p.2, 2010.

[47] http://sci.esa.int/planck/13238-planck-payload/, ESA and the Planck Collaboration.

[48] The Planck Collaboration: Ade P.A.R. et al., "Planck 2013 results. XIV. Zodiacal emission", Astronomy & Astrophysics, accepted for publication, 2014.

Appendix A

CAD drawings of horn attachments.

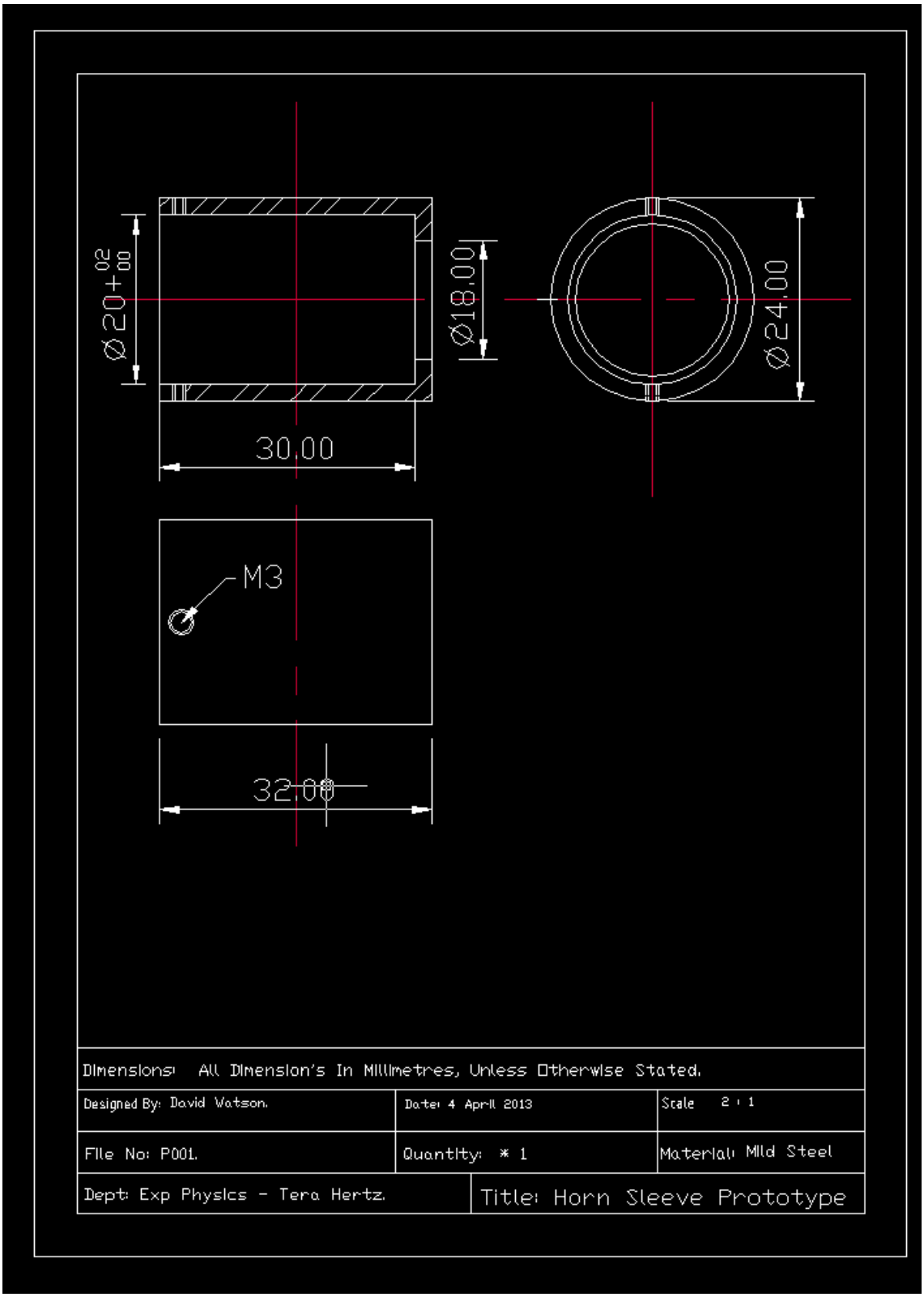

Figure A.1 Drawing of the sleeve (see Figure 4.17)

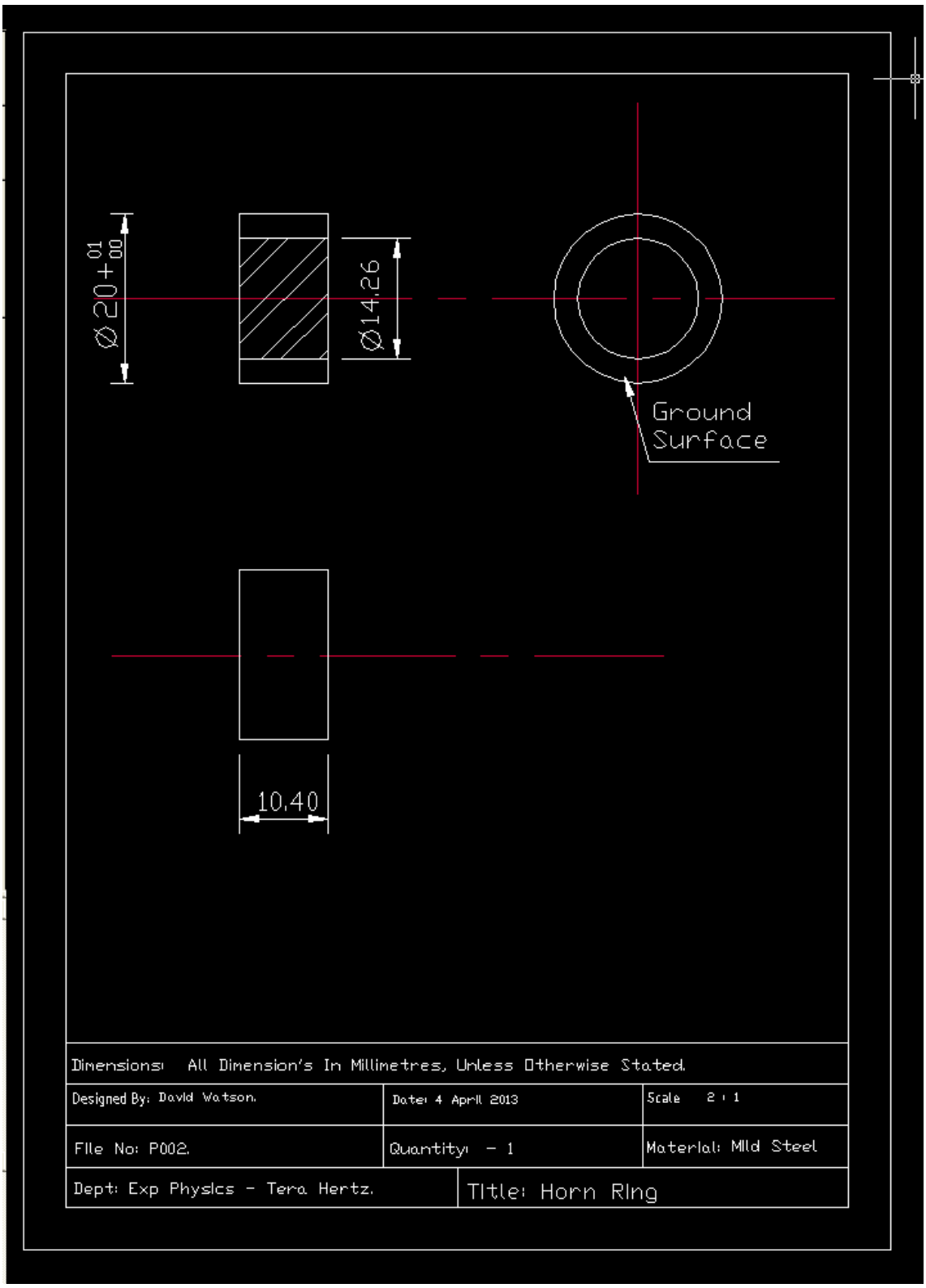

Figure A.2 Drawing of solid cylinder (see Figure 4.15)

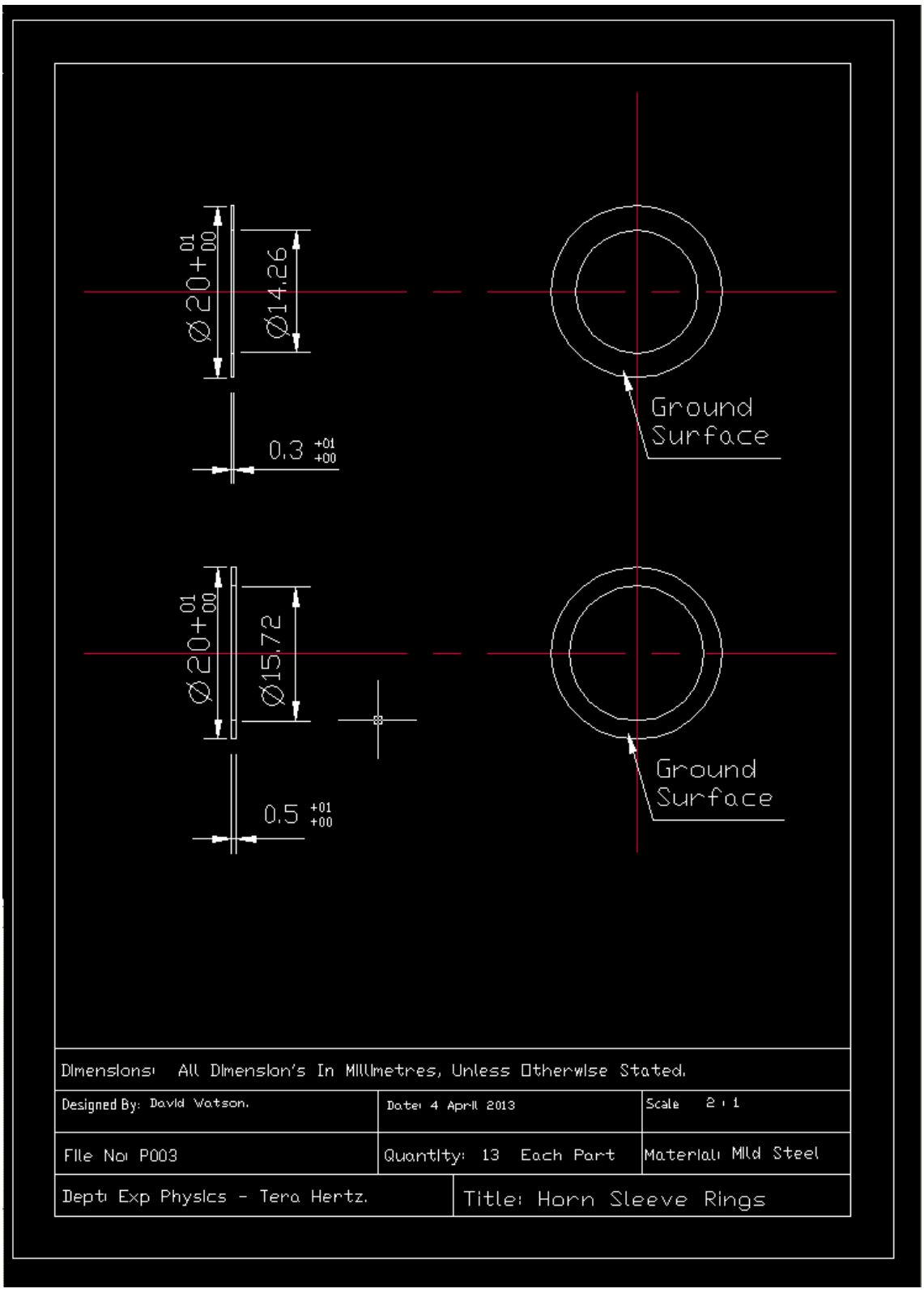

Figure A.3 Drawing of small and large rings (see Figure 4.15).

Appendix B

Co-polar and cross-polar results for filling corrugations

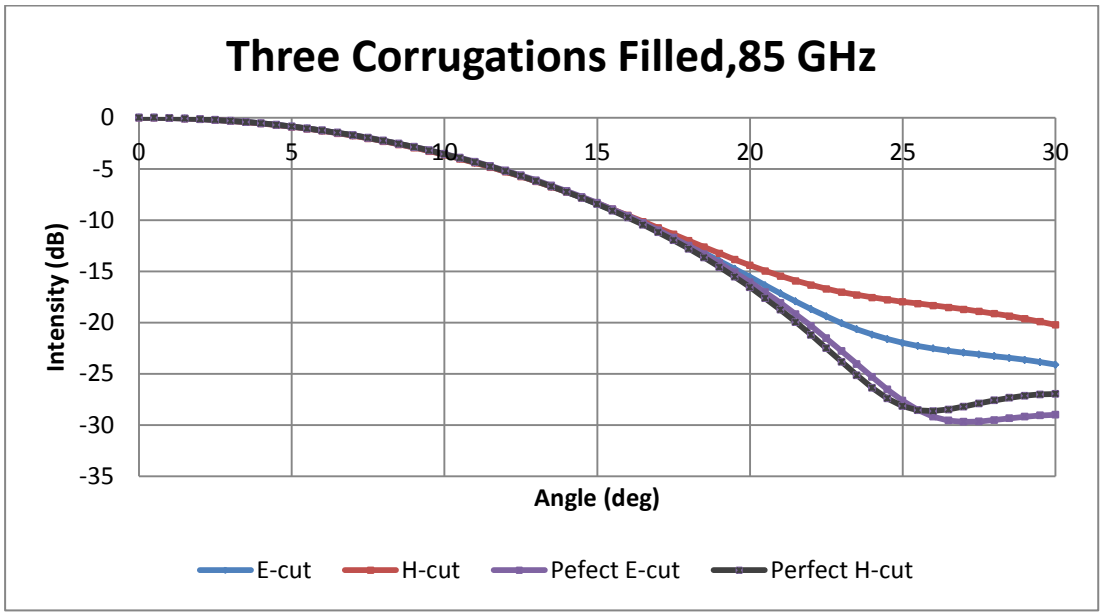

Figure B.1 Co-polar power as a function of off-axis angle for a corrugated horn which has had three corrugations filled in, operating at 85 GHz. The filled corrugations are at position 2 of the horn (see Figure 5.5). A horn without any filled corrugations was plotted for comparison (perfect E- and H-cuts).

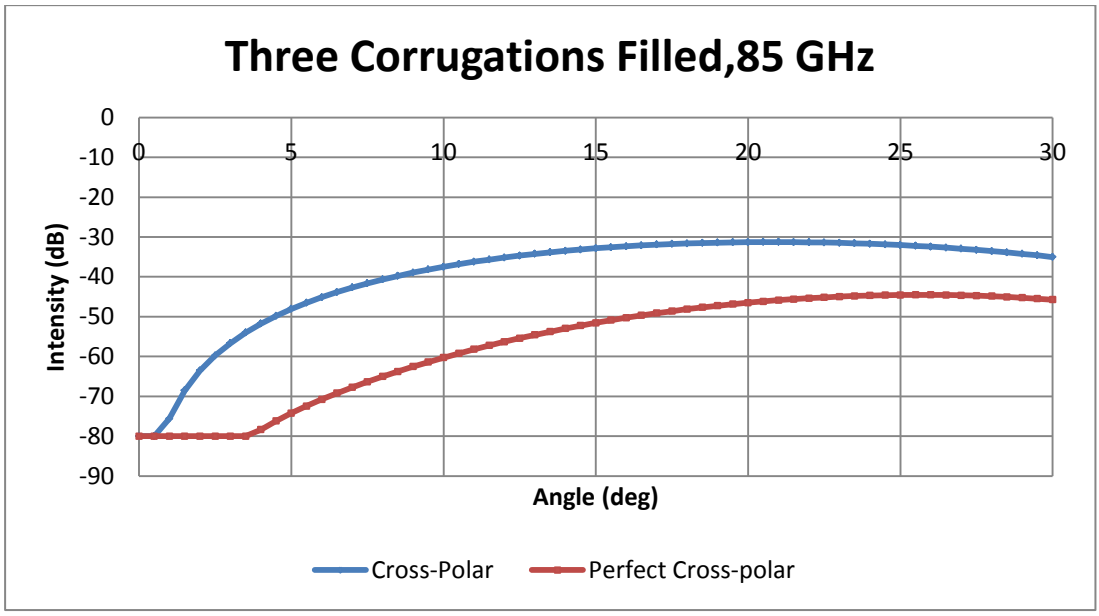

Figure B.2 Cross-polar power as a function of off-axis angle for a corrugated horn which has had three corrugations filled in, operating at 85 GHz. The filled corrugations are at position 2 of the horn (see Figure 5.5). A horn without any filled corrugations was plotted for comparison (perfect cross-polar).

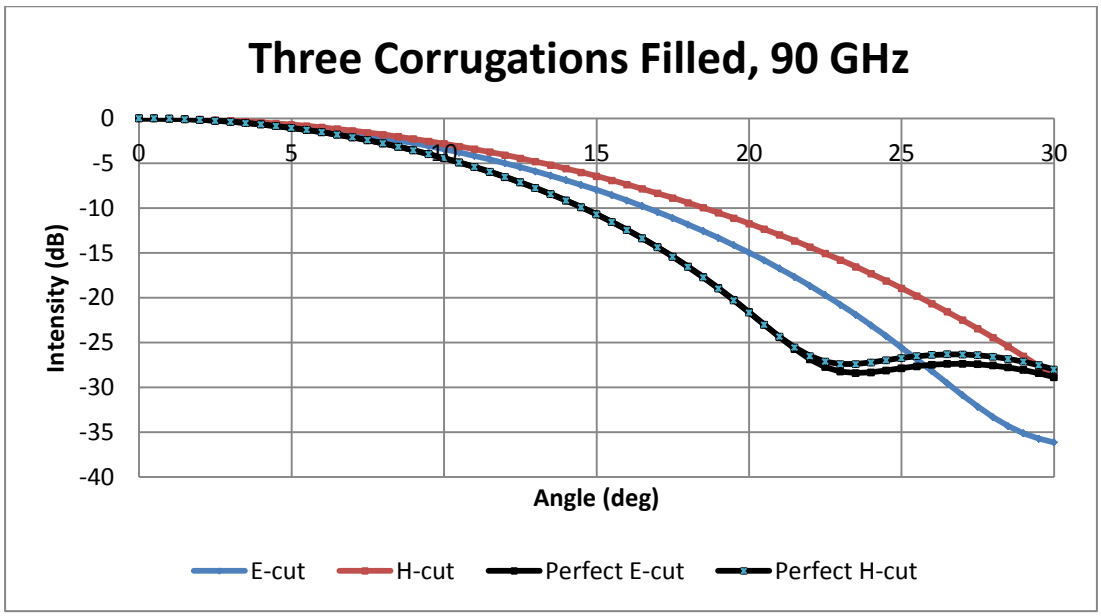

Figure B.3 Co-polar power as a function of off-axis angle for a corrugated horn which has had three corrugations filled in, operating at 90 GHz. The filled corrugations are at position 2 of the horn (see Figure 5.5). A horn without any filled corrugations was plotted for comparison (perfect E- and H-cuts).

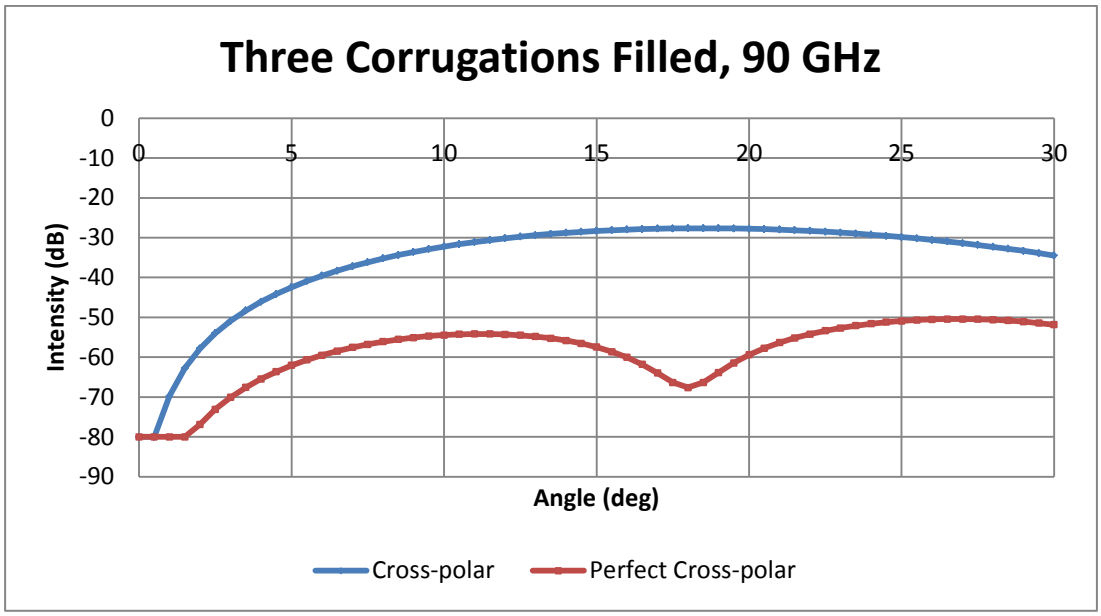

Figure B.4 Cross-polar power as a function of off-axis angle for a corrugated horn which has had three corrugations filled in, operating at 90 GHz. The filled corrugations are at position 2 of the horn (see Figure 5.5). A horn without any filled corrugations was plotted for comparison (perfect cross-polar).

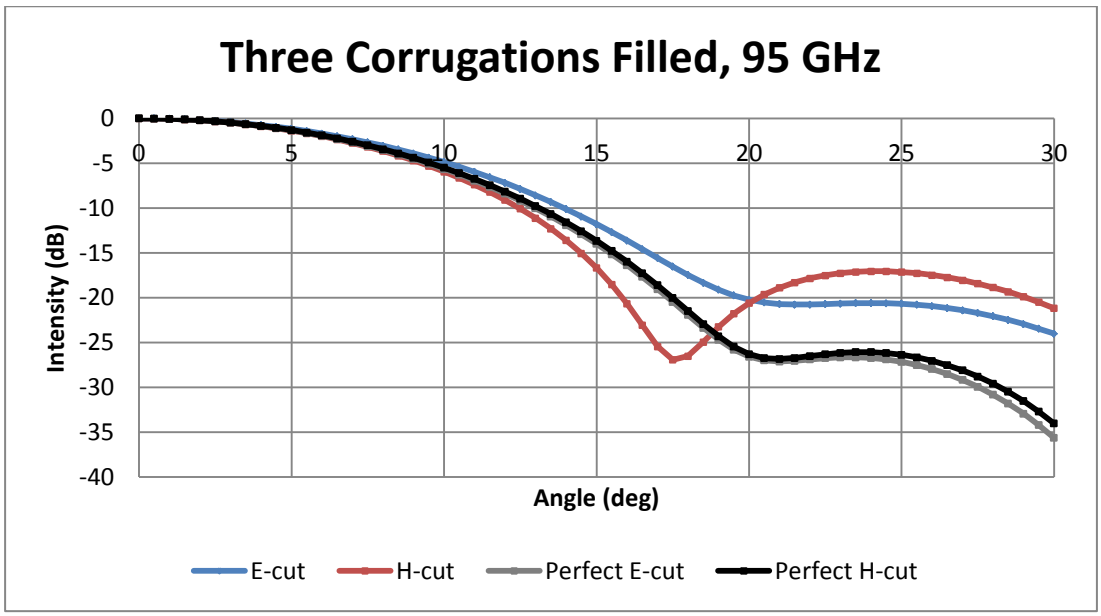

Figure B.5 Co-polar power as a function of off-axis angle for a corrugated horn which has had three corrugations filled in, operating at 95 GHz. The filled corrugations are at position 2 of the horn (see Figure 5.5). A horn without any filled corrugations was plotted for comparison (perfect E- and H-cuts).

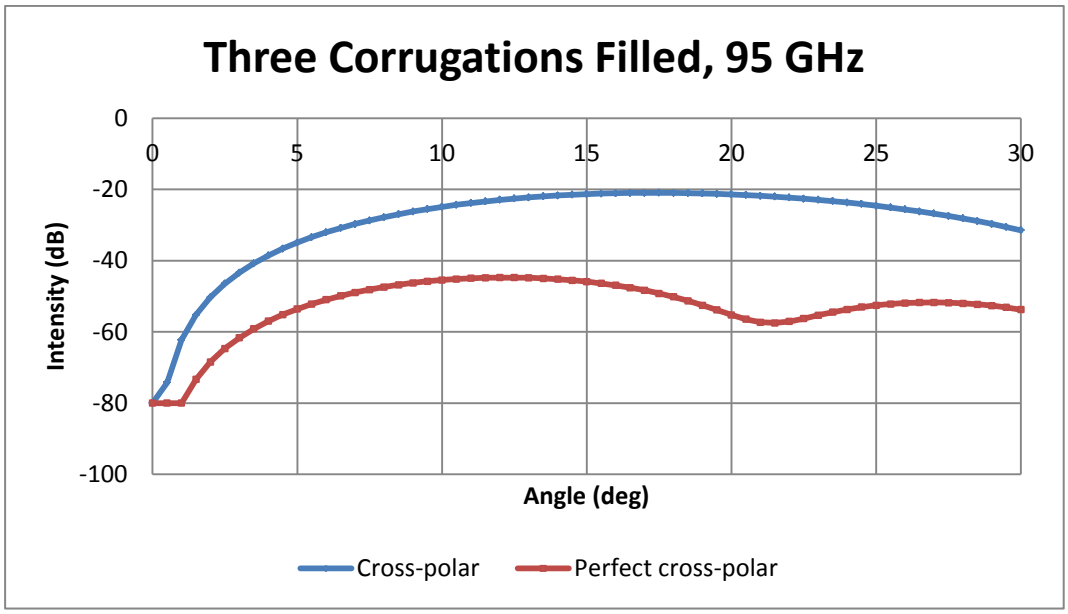

Figure B.6 Cross-polar power as a function of off-axis angle for a corrugated horn which has had three corrugations filled in, operating at 95 GHz. The filled corrugations are at position 2 of the horn (see Figure 5.5). A horn without any filled corrugations was plotted for comparison (perfect cross-polar).

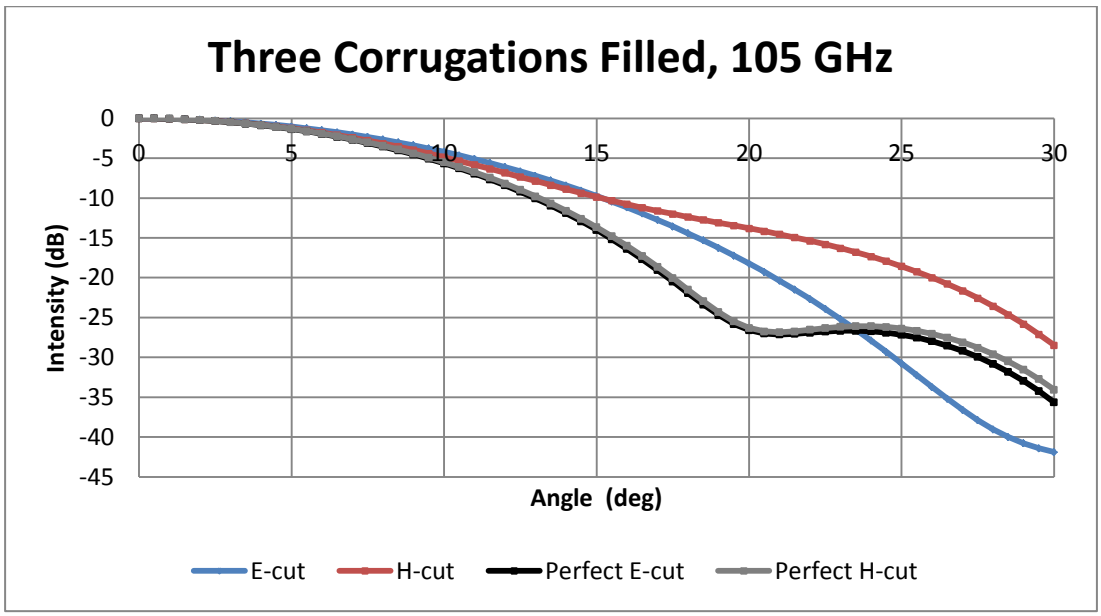

Figure B.7 Co-polar power as a function of off-axis angle for a corrugated horn which has had three corrugations filled in, operating at 105 GHz. The filled corrugations are at position 2 of the horn (see Figure 5.5). A horn without any filled corrugations was plotted for comparison (perfect E- and H-cuts).

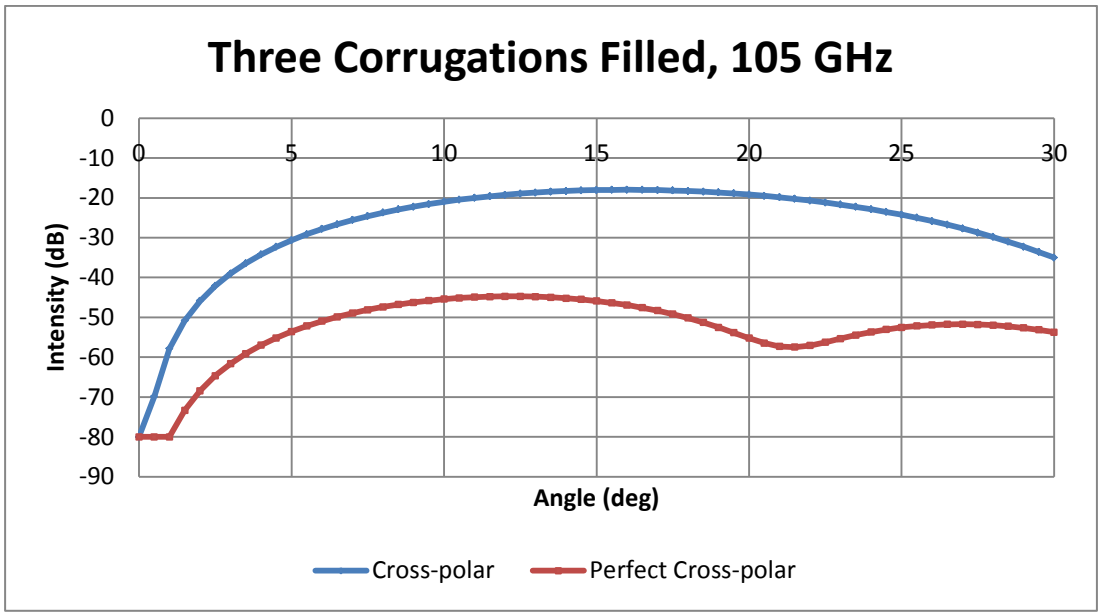

Figure B.8 Cross-polar power as a function of off-axis angle for a corrugated horn which has had three corrugations filled in, operating at 105 GHz. The filled corrugations are at position 2 of the horn (see Figure 5.5). A horn without any filled corrugations was plotted for comparison (perfect cross-polar).

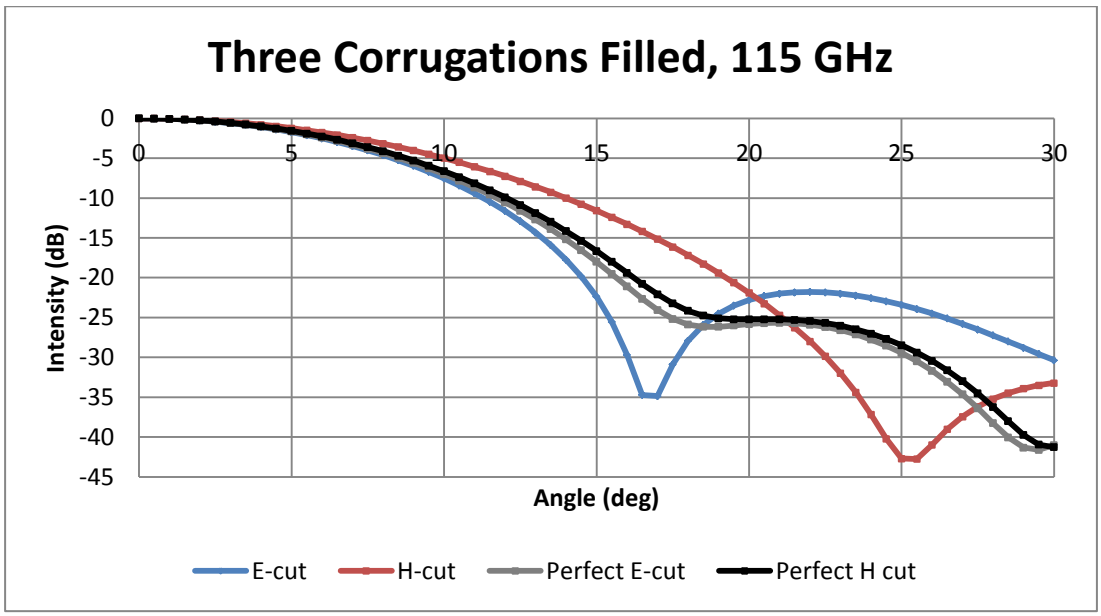

Figure B.9 Co-polar power as a function of off-axis angle for a corrugated horn which has had three corrugations filled in, operating at 115 GHz. The filled corrugations are at position 2 of the horn (see Figure 5.5). A horn without any filled corrugations was plotted for comparison (perfect E- and H-cuts).

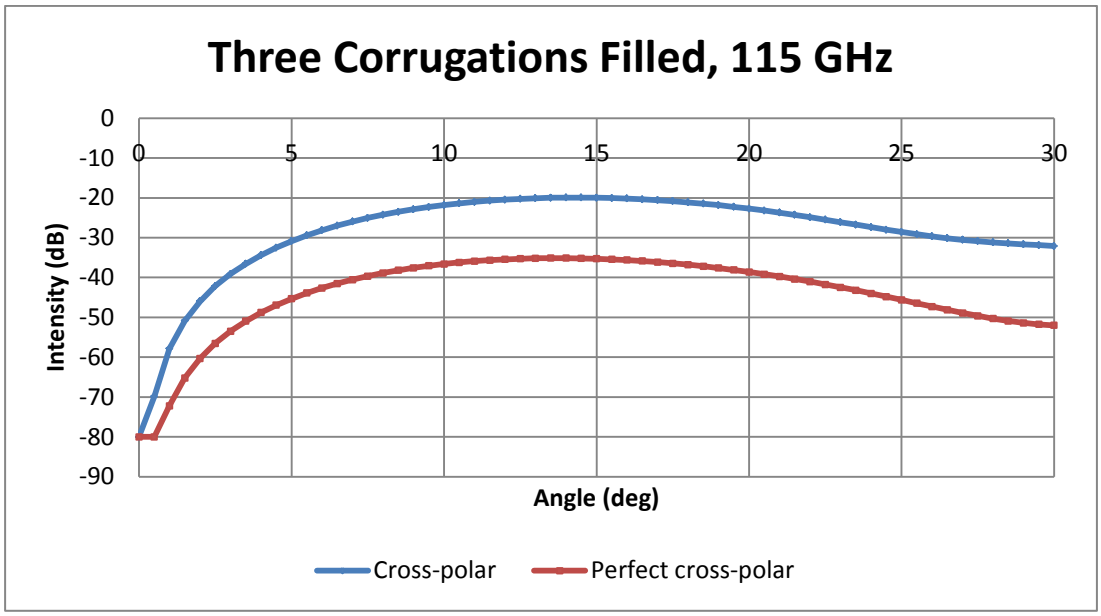

Figure B.10 Cross-polar power as a function of off-axis angle for a corrugated horn which has had three corrugations filled in, operating at 115 GHz. The filled corrugations are at position 2 of the horn (see Figure 5.5). A horn without any filled corrugations was plotted for comparison (perfect cross-polar).

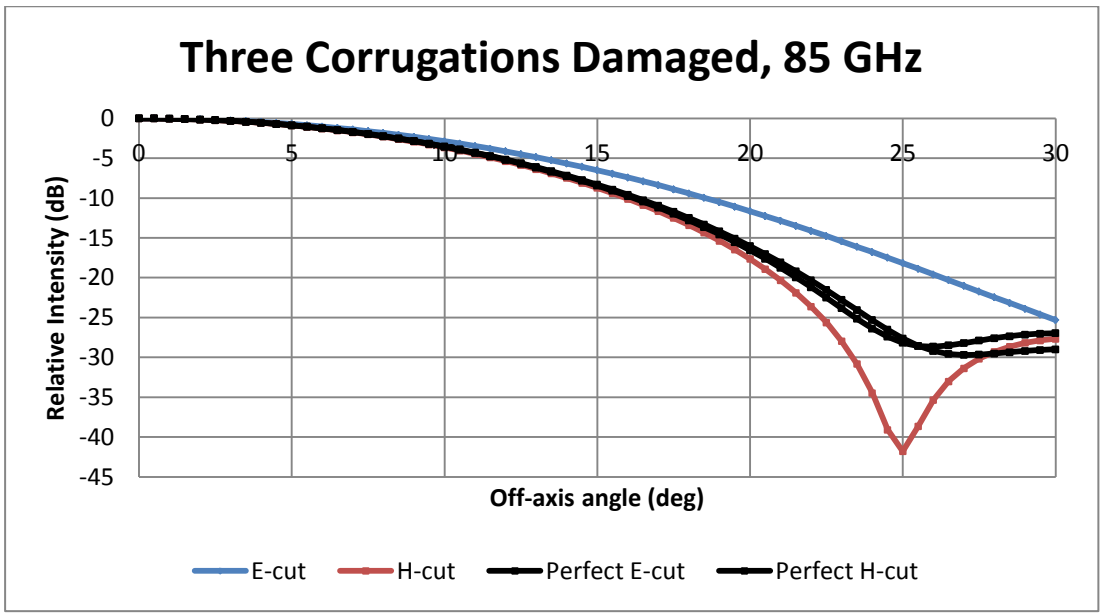

Figure B.11 Co-polar power as a function of off-axis angle for a corrugated horn which has had three corrugations removed, operating at 85 GHz. The removed corrugations are at position 2 of the horn (see Figure 5.5). A horn without any removed corrugations was plotted for comparison (perfect E- and H-cuts).

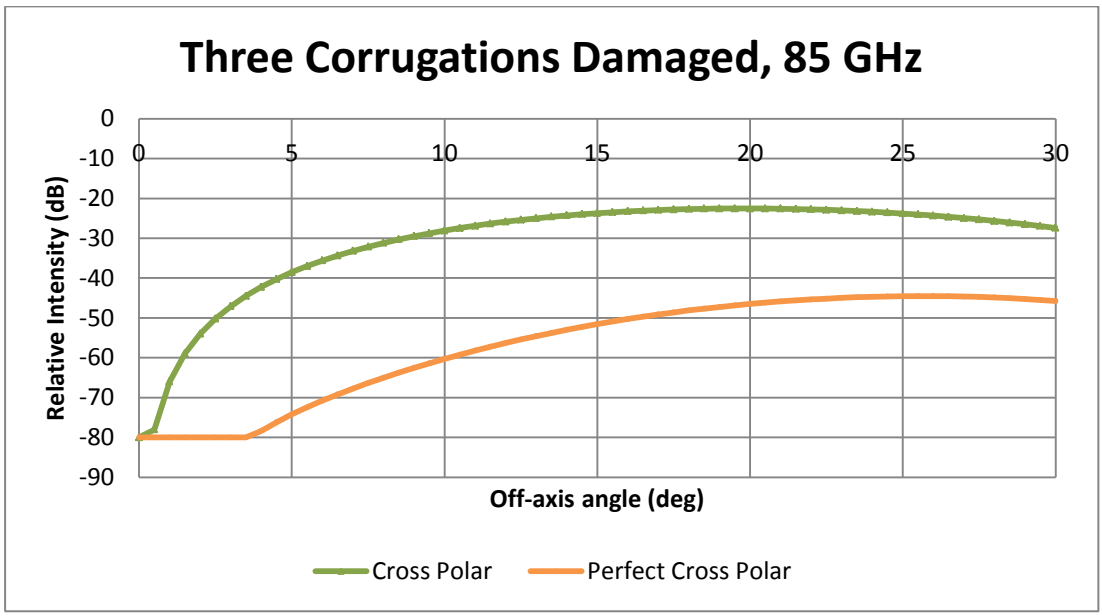

Figure B.12 Cross-polar power as a function of off-axis angle for a corrugated horn which has had three corrugations removed, operating at 85 GHz. The removed corrugations are at position 2 of the horn (see Figure 5.5). A horn without any removed corrugations was plotted for comparison (perfect cross-polar).

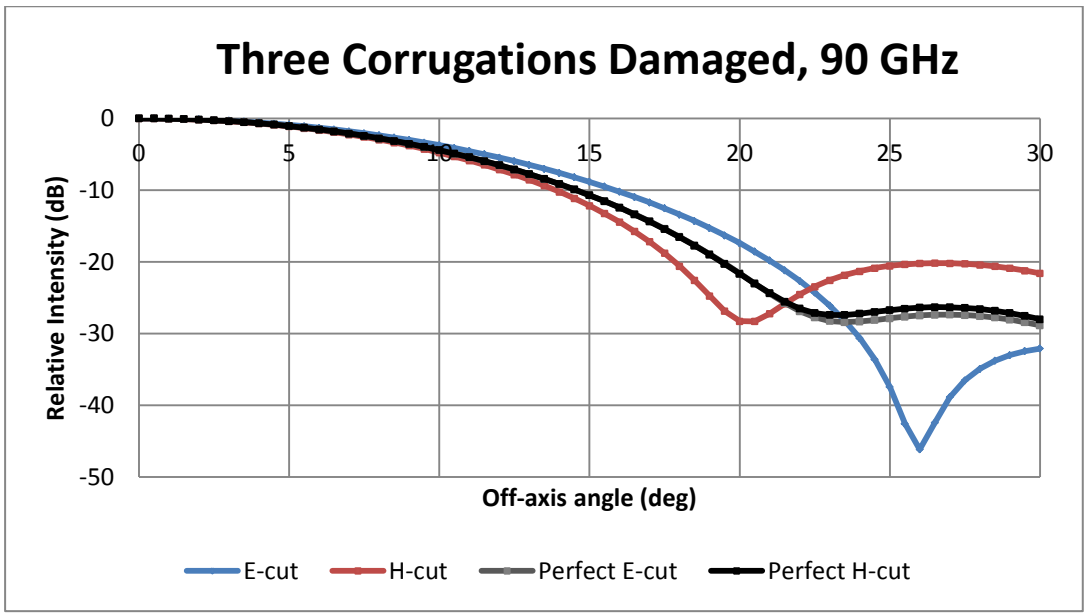

Figure B.13 Co-polar power as a function of off-axis angle for a corrugated horn which has had three corrugations removed, operating at 90 GHz. The removed corrugations are at position 2 of the horn (see Figure 5.5). A horn without any removed corrugations was plotted for comparison (perfect E- and H-cuts).

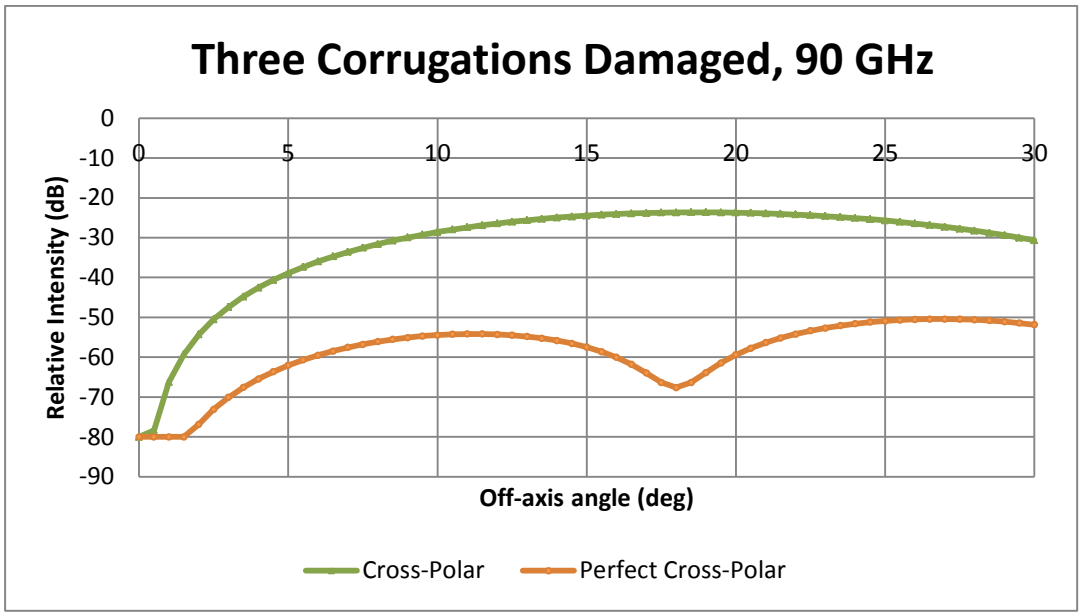

Figure B.14 Cross-polar power as a function of off-axis angle for a corrugated horn which has had three corrugations removed, operating at 90 GHz. The removed corrugations are at position 2 of the horn (see Figure 5.5). A horn without any removed corrugations was plotted for comparison (perfect cross-polar).

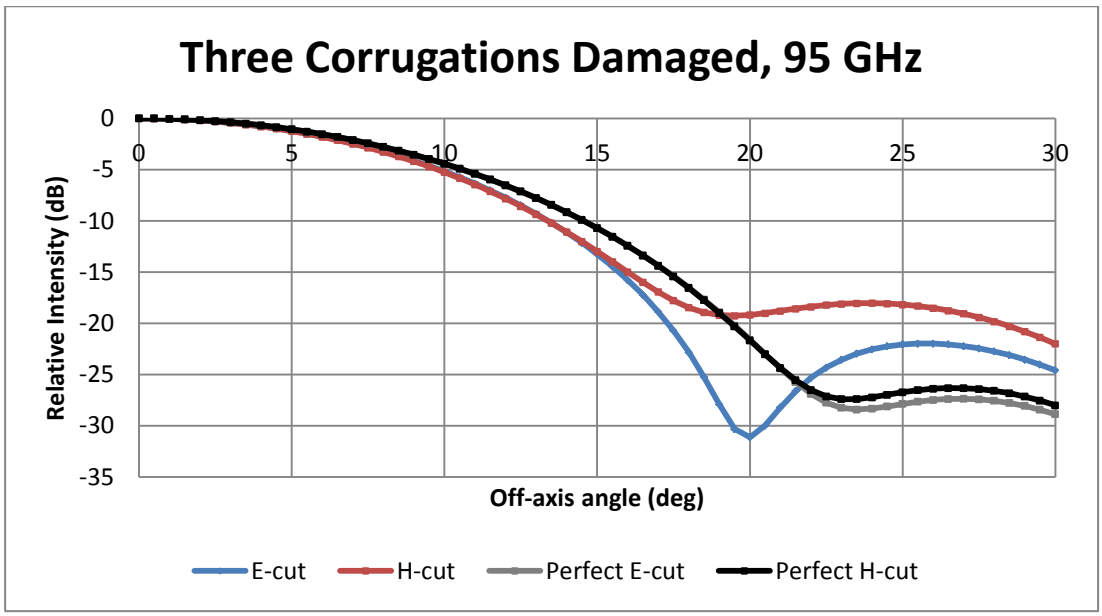

Figure B.15 Co-polar power as a function of off-axis angle for a corrugated horn which has had three corrugations removed, operating at 95 GHz. The removed corrugations are at position 2 of the horn (see Figure 5.5). A horn without any removed corrugations was plotted for comparison (perfect E- and H-cuts).

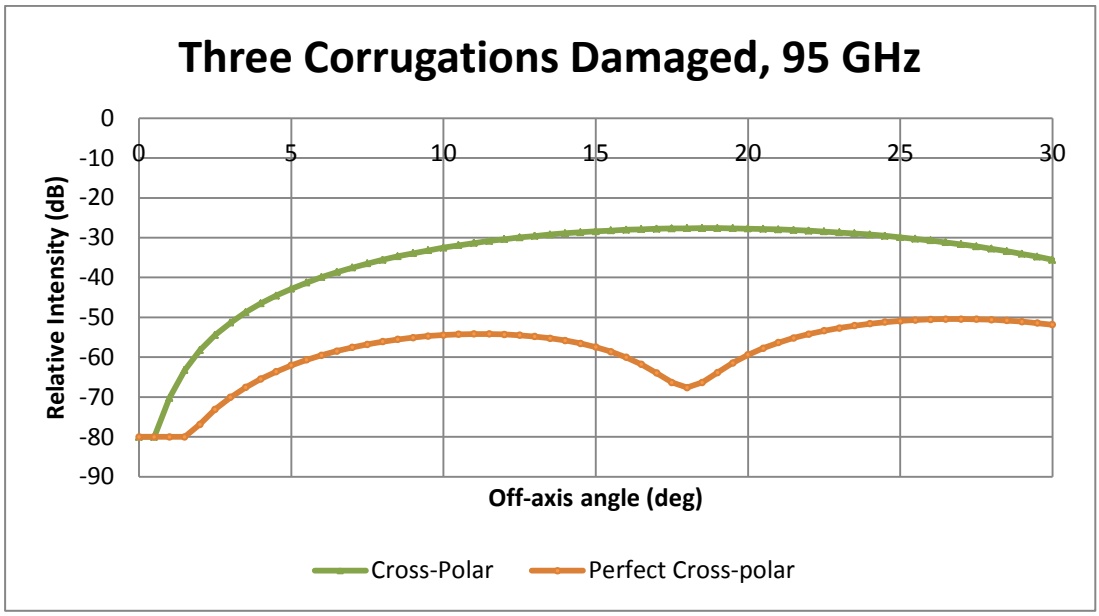

Figure B.16 Cross-polar power as a function of off-axis angle for a corrugated horn which has had three corrugations removed, operating at 95 GHz. The removed corrugations are at position 2 of the horn (see Figure 5.5). A horn without any removed corrugations was plotted for comparison (perfect cross-polar).

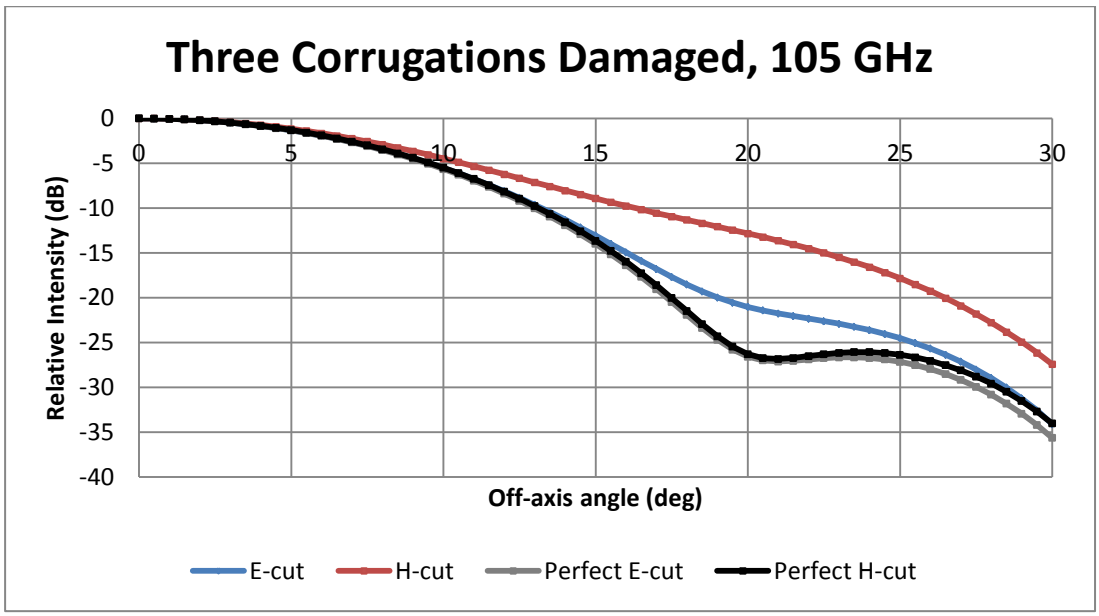

Figure B.17 Co-polar power as a function of off-axis angle for a corrugated horn which has had three corrugations removed, operating at 105 GHz. The removed corrugations are at position 2 of the horn (see Figure 5.5). A horn without any removed corrugations was plotted for comparison (perfect E- and H-cuts).

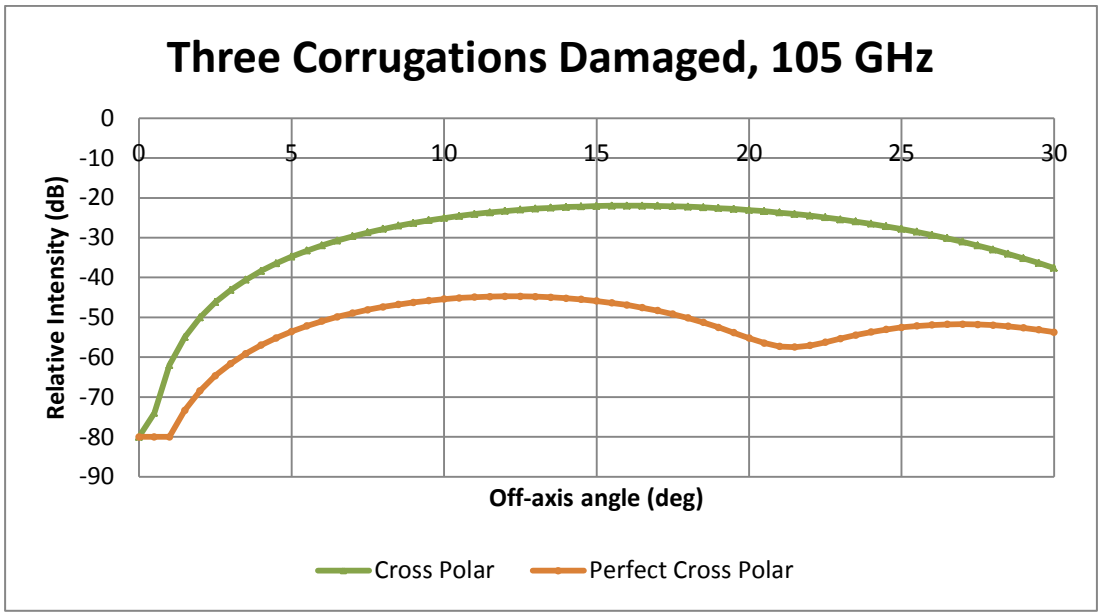

Figure B.18 Cross-polar power as a function of off-axis angle for a corrugated horn which has had three corrugations removed, operating at 105 GHz. The removed corrugations are at position 2 of the horn (see Figure 5.5). A horn without any removed corrugations was plotted for comparison (perfect cross-polar).

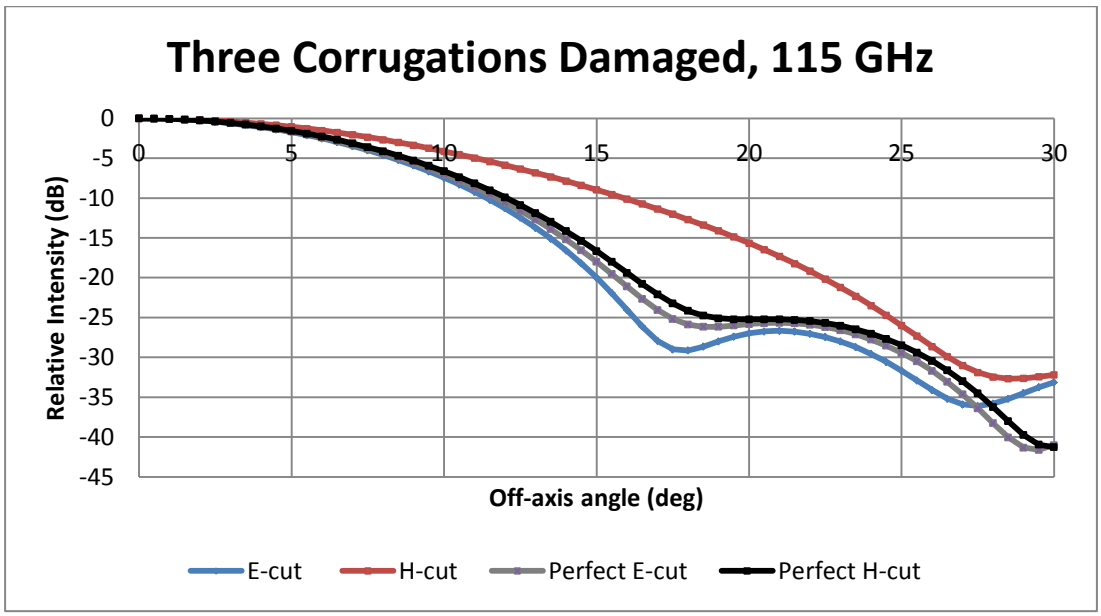

Figure B.19 Co-polar power as a function of off-axis angle for a corrugated horn which has had three corrugations removed, operating at 115 GHz. The removed corrugations are at position 2 of the horn (see Figure 5.5). A horn without any removed corrugations was plotted for comparison (perfect E- and H-cuts).

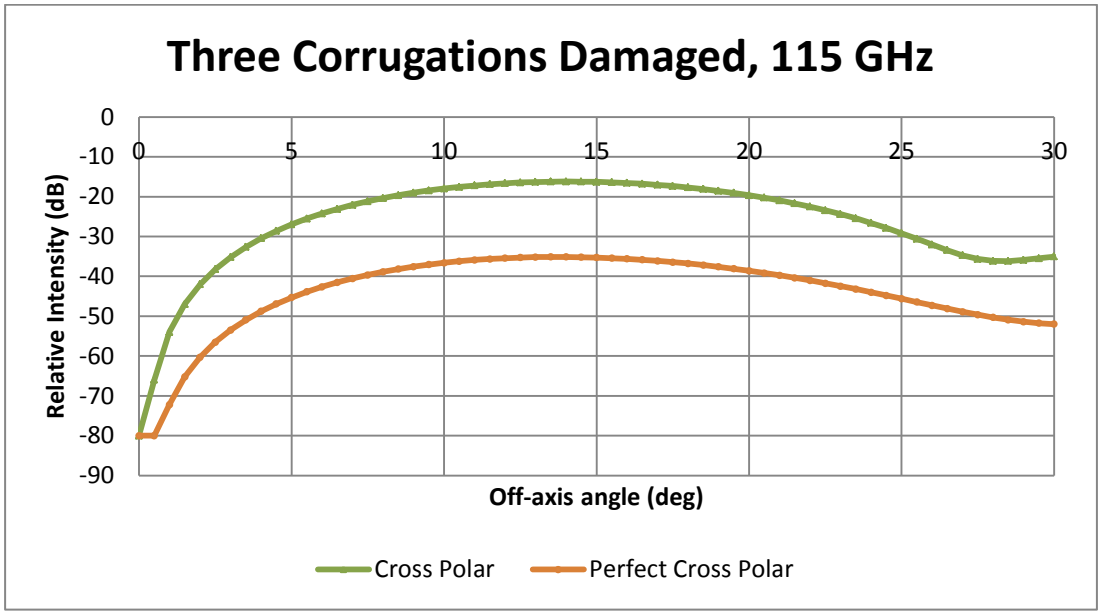

Figure B.20 Cross-polar power as a function of off-axis angle for a corrugated horn which has had three corrugations removed, operating at 115 GHz. The removed corrugations are at position 2 of the horn (see Figure 5.5). A horn without any removed corrugations was plotted for comparison (perfect cross-polar).